An experimental study of an inherently-safe, natural circulating, flash-tube type system for a nuclear reactor steam supply concept

by
Karl Albie Loubser

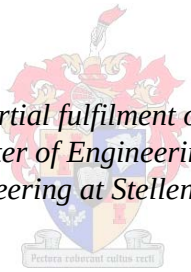

Thesis presented in partial fulfilment of the requirements for the degree of *Master of Engineering (Mechanical) in the Faculty of Engineering at Stellenbosch University*

Supervisor: Mr Robert Thomas Dobson

December 2014

The financial assistance of the National Research Foundation (NRF) towards this research is hereby acknowledged. Opinions expressed and conclusions arrived at, are those of the author and are not necessarily to be attributed to the NRF.

Declaration

By submitting this thesis electronically, I declare that the entirety of the work contained therein is my own, original work, that I am the sole author thereof (save to the extent explicitly otherwise stated), that reproduction and publication thereof by Stellenbosch University will not infringe any third party rights and that I have not previously in its entirety or in part submitted it for obtaining any qualification.

Date: .....

Abstract

An experimental study of an inherently-safe, natural circulating, flash-tube type system for a nuclear reactor steam supply concept

K.A. Loubser

Department of Mechanical and Mechatronic Engineering,
University of Stellenbosch,
*Private Bag X1, MATIELAND **7602**, South Africa.*

Thesis: MEng (Mech)

December 2014

This project investigates aspects of a novel inherently safe nuclear power steam supply system as safety is of paramount importance. The system envisaged has unique features namely: a) a two-phase flow flash-tube type natural circulating primary loop (also the secondary radioactive particle containment); b) a two-phase flow thermosyphon heat pipe type heat exchanger secondary loop is used to transfer heat from the primary loop to the steam generators, thereby physically separating the two flow streams from one another; c) a natural convection air cooled condenser for the removal of the reactor's residual heat; d) a unique core using TRISO type fuel (acting as the primary radioactive particle containment) with life of at least 8.9 years; e) a steel containment vessel acting as a tertiary radioactive product containment; f) a concrete containing structure with air vents to allow air to pass over the main steel containment vessel for cooling purposes in the case of an emergency, and for the removal of parasitic heat during operation.

In particular the primary and secondary loops of the proposed system are investigated. This is done by design, construction and testing of a small scale experimental set-up of the primary and secondary loops as well as the development of theoretical models for the two loops. A literature survey focusing on nuclear technology, thermosyphon loops, natural circulating loop instabilities, heat pipes, and two-phase flow modelling is presented to give a brief overview of the technologies as well as tools used in the work undertaken.

Observations of the inside flow behaviour of the primary loop experimental set-up were made possible by windows providing many insights into the inner workings, such as plume formation and geysering. The transient response of the secondary heat pipe loop start-up is also investigated.

A thermal resistance theoretical model was developed for the secondary loop using heat transfer formulae from theory as well as experimentally semi-empirical correlated formula. Different states of operation of the secondary loop were observed during testing with the theoretical model of the condensing

regime correlating well, two-phase regime correlating acceptably and liquid regime correlating poorly to experimental results and thus were modelled using an experimentally determined overall heat transfer coefficient. The secondary loop model of the liquid regime is coupled with the primary loop theoretical model to predict the system's performance.

A homogeneous, one-dimensional, simple theoretical model for the primary loop was derived and computer simulated. The results did not compare well with experimental results for single phase flow and failed to capture the onset of two-phase flow. The assumptions of one dimensional model with a unidirectional flow, a hydrostatic pressure problem, a constant volumetric flow rate and the inability of the implementation of the code to handle expansion are noted as some of the flaws in the theoretical model.

The following recommendations are made: a more advanced design of the pressuriser should be incorporated into the experiment; the secondary loop's theoretical model should be characterised under a broader set of operating conditions; the computer program can be used as the basis for further research and implementation of alternative solution algorithms and models.

Uittreksel

'n Eksperimentele studie van 'n essensieel veilige, natuurlik sirkulerende, flits-buis-tipe sisteem vir 'n kernkrag reaktor stoomtoevoer konsep

(An experimental study of an inherently-safe, natural circulating, flash-tube type system for a nuclear reactor steam supply concept)

K.A. Loubser

Departement Meganiese en Megatroniese Ingenieurswese,
Universiteit van Stellenbosch,
*Privaatsak X1, MATIELAND **7602**, Suid Afrika.*

Tesis: MIng (Meg)

Desember 2014

Hierdie projek ondersoek aspekte van 'n ongewone, essensieel veilige kernkrag stoomtoevoer-stelsel, omdat veiligheid van kardinale belang is. Die stelsel wat voorgestel is, het unieke eienskappe, naamlik: a) 'n twee-fasevloei flits-buis-tipe natuurlik sirkulerende primêre lus (wat ook die sekondêre inperking van radioaktiewe materiaal bevat); b) 'n twee-fasevloei termo-heweleffek sekondêre lus hitte-pyp hitte-uitruiler word gebruik om die hitte vanaf die primêre lus oor te dra na die stoomkragopwekkers en daardeur word die twee strome se vloei fisies geskei van mekaar; c) 'n natuurlike konveksie lugverkoelde kondensor word gebruik vir die verwydering van die reaktors se oortollige hitte; d) 'n unieke kern gebruik TRISO-tipe brandstof (wat as die primêre inperking van radioaktiewe materiaal optree) met 'n lewe van minstens 8.9 jaar; e) 'n inperkingshouer van staal wat optree as 'n tersiêre radioaktiewe produkhouer; f) 'n betonstruktuur met lugventilasie om toe te laat dat lug oor die hoof staalhouer vloei vir verkoeling in 'n noodgeval, en vir die verwydering van parasitiese hitte tydens werking.

Hoofsaaklik word die primêre en sekondêre lusse van die voorgestelde stelsel ondersoek. Dit word gedoen deur die ontwerp, konstruksie en die toets van 'n eksperimentele opstelling van die primêre en sekondêre lusse op klein skaal, sowel as die ontwikkeling van teoretiese modelle vir die twee lusse. 'n Literatuurstudie wat fokus op kerntegnologie, termo-heweleffeklusse, natuurlik sirkulerende lus instabiliteit, hitte-pype, en twee-fase vloeimodellering word aangebied om 'n kort oorsig te gee van die tegnologie, sowel as gereedskap gebruik in die werk wat onderneem is.

Om die interne vloeigedrag van die primêre lus se eksperimentele opstelling waar te neem, word daar gebruik gemaak van vensters wat dien as 'n manier om die innerlike werking van die proses soos pluimvorming en die kook van die

water in die warmwaterkolom te toon. Die oorgangsreaksie van die sekondêre hittepyplus aanvangs is ook ondersoek.

'n Teoretiese termiese weerstandmodel is ontwikkel vir die sekondêre lus met behulp van hitte-oordragformules waarvoor hitte-oordragteorie gebruik is, wat met eksperimentele semi-empiriese formules gekorreleer is. Verskillende toestande van die sekondêre lus se werking is waargeneem gedurende die toetse. Die teoretiese model het goed met die kondensasiestaat gekorreleer, terwyl by die twee-fasewerkswyse aanvaarbare korrellasies aangetref is en die uiteindelike vloeitoestand swakker gekorrelleer het met eksperimentele resultate en dus gemodelleer is met behulp van die NTU-effektiwiteitsmetode. Die sekondêre lusmodel van die vloeistoftoestand is gekoppel met die primêre lus teoretiese model om die werking van die stelsels te voorspel.

'n Homogene een-dimensionele eenvoudige teoretiese model van die primêre lus is afgelei en 'n rekenaar simulasie is uitgevoer. Die resultate vergelyk nie goed met die eksperimentele resultate vir enkelfasevloei en kon nie die aanvang van twee-fasevloei beskryf nie. Die aannemings van 'n een-dimensionele model met eenrigting vloei, 'n hidrostatiese druk probleem, 'n konstant volumetries vloeitempo en die onvermoë van die implementering van die kode om uitbreiding te hanteer is bekend as 'n paar van die foute in die teoretiese model.

Die volgende aanbevelings word gemaak: 'n meer gevorderde ontwerp van drukreëlaar moet in die eksperiment ingesluit word; die sekondêre lus se teoretiese model moet gekenmerk word onder 'n wyer stel bedryfsomstandighede, en die rekenaar program kan gebruik word as die basis vir verdere navorsing en die implementering van alternatiewe algoritmes en modelle.

Dedications

Dedicated to
Hermann Anton Armbruster

The author would like to acknowledge the following people for their assistance during the project:

Mr C. Zietsman for his advice and technical expertise during the design and manufacture of the experimental set-up.

Mr F. Zietsman for his advice and assistance in the design and manufacture of the experimental set-up.

The employees of the Mechanical Engineering Department Workshop. Specific thanks to Mr J. Stanfliet for his assistance during the assembly and calibration, and Mr C. Samuels for his assistance in the manufacture of experimental set-up.

Mr C. Wahl for his assistance in the design, construction and assembly of the initial experimental set-up.

Mr J. du Preez and Mrs A. Kruger for their assistance in the translation of the abstract.

Mr P. Ioppo, Mr N. Ablett and Miss Z. Nel for their help in the finalization and criticism of the final document.

Mr M. Armbruster for his continued support, guidance and motivation during the course of the research.

The National Research Foundation for financing this researching.

My family for their love and support throughout my studies.

Mr RT Dobson, the supervisor of this thesis, for his advice, expertise, support, supervision, insights and most importantly patience during the course of this research.

Contents

List of Figures

List of Tables

Nomenclature

Variables

A	Area, m^2
B	Buoyancy term
C	Correlation constant
C	Courant-Friedrichs-Lewy (CFL) condition value
c_p	Constant pressure specific heat, J/kg·K
D	Diameter, m
E	Total energy, J
F	Factor/Frictional term
$f(x)$	Function of x
G	Volumetric flow rate, m^3/s
g	Gravitational constant, $9.81\,m/s^2$
H	Enthalpy, J
h	Specific enthalpy, J/kg
h	Heat transfer coefficient, $W/m^2{\cdot}K$
K_L	Minor loss coefficient
k	Thermal conductivity, W/m·K
L	Length, m
M	Momentum term
m	Mass, kg
$\dot{m}$	Mass flow rate, kg/s
NTU	Number of transfer units
n	Correlation constant
P	Pressure, Pa
$\wp$	Perimeter, m
$\dot{Q}$	Heat transfer rate, W
$\dot{q}''$	Heat flux, W/m^2
R	Thermal resistance, K/W
T	Temperature, ℃ or K
t	Time, s
U	Internal energy, J
U	Overall heat transfer coefficient,$W/m^2{\cdot}K$
V	Volume, m^3
v	Velocity, m/s

x	Vapour mass fraction
z	Length of control volume, m

Greek symbols

α	Vapour void fraction
β	Volume expansiveness, 1/K
δ	Thickness, m
ε	Efficiency
μ	Dynamic viscosity, kg/m·s
ρ	Density, kg/m^3
σ	Surface tension, N/m
σ	Standard deviation
τ	Shear stress, N/m^2
ϕ	Diameter, m

Subscripts

amb	Ambient/Environmental
ave	Average
c	Characteristic/Condenser
ch	Channel
con	Connection control volume/Conduction
cu	Copper
cw	Cooling water/Condenser wall
cyl	Cylinder
D	Diameter
dp	Discharge point
err	Error
Exp	Experimental
e	Evaporator
e	Electrical
ele	Electrical element
env	Environment
eq	Equivalent
est	Estimated
exp	Expansion
f	Frictional
fg	Fluid/Gas

g	Gas
$HP2$	Heat pipe number 2
h	Hydraulic
i	Inside/i^{th} control volume
l	Liquid
max	Maximum
min	Minimum
o	Outside
$orig$	Original
Pre	Predicted
s	Surface
sat	At saturation state
th	Thermal
tot	Total
w	Wall
2ϕ	Two-phase
∞	Bulk property
@	At

Superscripts

n	Correlation constant
$''$	Flux, /m^2

Over-score

$\dot{}$	Time rate, /s
—	Average

Non-Dimensional

C	Courant number, $C = v\Delta t/\Delta x$
Nu	Nusselt number, $Nu = hL_c/k$
Pr	Prandtl number, $Pr = \mu c_p/k$
Ra	Rayleigh, $Ra = \text{g}\beta(T_s - T_\infty)L_c^3 Pr/(\mu/\rho)^2$
Re	Reynolds number, $Re = \rho v L_c/\mu$

Acronyms

BWR	Boiling Water Reactor
CV	Control Volume

ESS	Emergency Safety Systems
FMW	Field Meteorology Well
GIF	Generation IV International Forum
HP	Heat Pipe
ID	Internal Diameter
KE	Kinetic Energy
LWR	Light Water Reactor
NCL	Natural Circulation Loop
NCLs	Natural Circulation Loops
NTU	Number of Transfer Units
OD	Outer Diameter
PE	Potential Energy
PRT	Platinum Resistance Thermometer
PWR	Pressurised Water Reactor
RHRS	Residual Heat Removal System
RMS	Root Mean Squared
RMSE	Root Mean Squared Error
SMR	Small and Medium sized Reactors
SN	Serial Number
SSE	Sum of Squares due to Error

1 Introduction

This chapter serves as an introduction to the thesis. It briefly discusses the background and motivation for the work, the design concept under consideration, as well as the objectives for the research. The chapter concludes by giving an outline of the thesis chapters and how they relate to the objectives.

1.1 Background and Motivation

In October 2010, the Inter-Ministerial Committee on Energy of South Africa approved the draft Integrated Resource Plan (IRP), a 20-year blueprint that indicates that the country is planning to commit to 14 % nuclear power as part of its future energy mix. This is expected to result in Eskom making investments to increase South Africa's nuclear capacity by up to 9600 MW by 2029 (Republic of South Africa Department of Energy, 2010). Synonymous with Nuclear power is nuclear safety, as is reinforced by the disaster at Fukushima in Japan. Thus, it is imperative for South Africa to understand the concerns of utilizing nuclear power. Furthermore, South Africa should continue the development of nuclear technology to avoid losing the expertise gained during the planned nuclear expansion program.

The research will look at an innovative and unique nuclear reactor steam supply design concept and investigate the thermal-hydraulic nature and response of the system. The design concept originates from the generation IV requirements of (Generation IV International Forum and U.S. DOE Nuclear Energy Research Advisory Committee, 2002): 1) Providing sustainable energy generation that meets clean air objectives and promotes the long term availability of systems and effective fuel utilization for worldwide energy production; 2) Minimizing and managing nuclear waste and significantly reduce the long-term stewardship burden, thereby improving protection for the public health and the environment; 3) Having a level of financial risk comparable to other energy projects; 4) Having a clear life-cycle cost advantage over other energy sources; 5) Excelling in safety and reliability; 6) Having a very low likelihood and degree of reactor core damage; 7) Eliminate the need for off-site emergency response; 8) Be very unattractive and least desirable route for the diversion or theft of weapons-usable materials and provide increased physical protection against acts of terrorism. The idea is to investigate a concept of a reactor that is inherently safe. This is done by using natural circulation systems. This negates the opportunity for an accident as was experienced by the Japanese at Fukushima where power to circulate the coolant was lost. The method proposed to improve safety in a nuclear reactor system is not to add an additional system for a higher safety level but, rather from a conceptual stage, to design a system that does not need the additional system.

In addition to this, the research will also look at two-phase flow and the interaction between two heat pipe loops. This could then be adapted to pos-

sibly any application where an intermediate heat exchanger is required for containment purposes, such as waste stream heat recovery.

1.2 Design Concept

The concept under consideration is an innovative and unique nuclear reactor steam supply system, shown in Figure 1.1. The reactor to be investigated is unique in the fact that the primary loop will be driven solely by natural circulation and be neither a pressurised water reactor (PWR) nor a boiling water reactor (BWR). Instead, the reactor's primary loop will contain water in both the liquid and vapour phase (two-phase flow). Boiling will take place at a controlled level within a riser section (often referred to as a flash tube) above the reactor, unlike a BWR where it takes place within the core and a PWR where the primary loop is operated in single phase.

Besides the novelty of the reactor's primary loop itself, the entire system is envisioned to contain a number of unique concepts. These concepts (shown in Figure 1.1) include: 1) A two-phase thermosyphon type heat pipe secondary

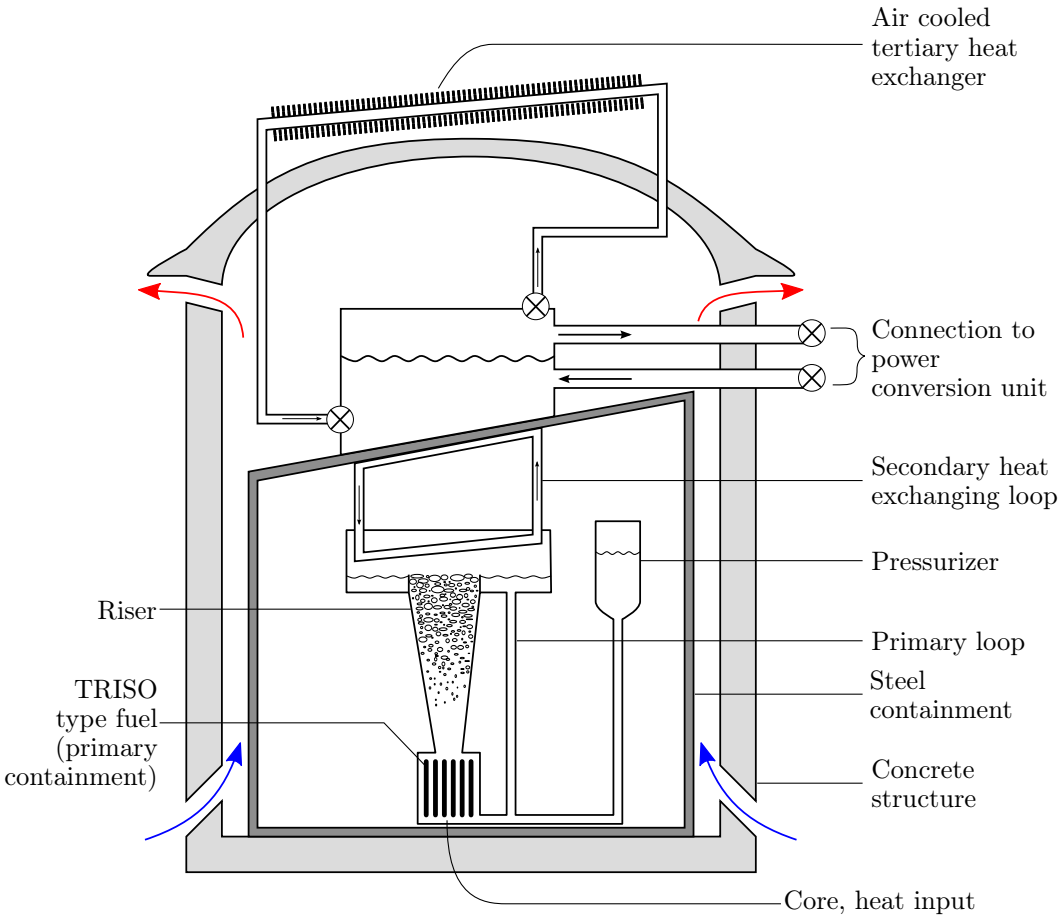

Figure 1.1: Nuclear reactor system showing the major components and natural circulating cooling air flow over the steel containment vessel

heat exchanging loop to transport the heat from the primary loop and making the heat available to generate steam whilst positively isolating the steam generator from the primary loop; 2) A natural convection air cooled condenser (Air cooled tertiary heat exchanger) which transfers heat out of the system to the air [the ultimate heat sink] and is large enough to remove the reactor's residual heat (after heat) during shut down; 3) A steel radioactive particle containment vessel acting as the tertiary product containment (primary loop is the secondary containment and the fuel is the primary); 4) A concrete containing structure with air vents to allow air to pass over the main steel containment vessel for cooling purposes in the case of an emergency, and for the removal of parasitic heat during operation. The core itself is also unique and is envisioned to be of a similar design to Tanihira and Shimazu (2007) which has a life of 8.9 equivalent full power years and utilises the pebble bed modular reactor TRISO type fuel.

1.3 Objectives

The proposed design concept, in section 1.2, encompasses a number of flow and heat transport devices/phenomena: the primary transport loop; heat pipe type thermosyphon secondary heat exchanger; power conversion unit (PCU); air cooled, natural circulation driven, tertiary heat exchanger and thermal response and heat transfer of the containment structures. With the large scope available in investigating the proposed concept, the objectives of the thesis are limited. The objectives of this thesis are to:

1. Build and test a small scale experimental set-up of the primary loop to which the secondary loop can be attached. Observations of flow phenomena within the primary loop experimental set-up must be possible.
2. Observe and document the inner workings and flow behaviour of the tested primary loop.
3. Develop a computer program based on the equations of change (conservation of mass, momentum and energy, and applicable property functions) to simulate the primary loop using a simple homogeneous flow model assuming so-called *quasi-equilibrium* conditions, as defined by Dobson (2012), within the loop. [So-called *quasi-equilibrium* implies that the speed of sound in the working fluid is considerably greater than the particle speed or average velocity and ultimately a constant homogeneous volumetric flow rate for all positions around the loop.]
4. Build a small scale secondary heat exchanger loop and attach it to the primary loop for testing.
5. Develop a theoretical model of the secondary heat exchanger loop using heat transfer theory for implementation in a computer program.

6. Correlate the secondary loop theoretical model data against experimental data.
7. Investigate the validity of the theoretical simulation of the primary and secondary loops.
8. Give recommendations on the path forward for further investigating the proposed system.

1.4 Layout

A brief summary of the layout of the thesis and how it intends to meet the above objectives is as follows:

Chapter 2 consists of a literature survey focusing on nuclear technology, thermosyphon loops and heat pipes, natural circulating loops instabilities and two-phase flow modelling. The survey gives a brief overview of the technologies and tools used in this thesis.

Chapter 3 deals with the modelling of the primary loop as required by objective 3. It begins with the assumptions implemented and takes the reader through the process followed in the development of the computer algorithm.

Chapter 4 discusses the theoretical modelling of the secondary loop heat exchanger. The chapter discusses the thermal resistance model and computer algorithm used to meet objective 5.

Chapter 5 explains the experimental set-up of both the primary and secondary loops built for objectives 1 and 4 respectively. The chapter explains the geometry and layout, the working fluids and materials, the instrumentation used and briefly discusses the data post-processing.

Chapter 6 deals with the observations made during testing. Objective 1 requires that the flow phenomena be observable inside the primary loop and objective 2 that the flow phenomena be observed and documented. The observations provide important insights into the workings of the loop in both the single and two phase flow operations.

Chapter 7 discusses the results of the experimental work and the theoretical models in four different sections. The experimental set-ups' subsequent test results of objectives 1 and 4 are firstly discussed. The secondary loop theoretical semi-empirical characterisation is then explained, completing objective 6. The secondary and primary loops' theoretical models are discussed and compared to the respective experimental results, thereby completing objective 7.

Penultimately, a discussion and conclusion of the presented work is given in chapter 8; and finally, chapter 9 deals with the forward path of the research through the author's recommendations, thereby completing objective 8.

2 Literature Survey

The system under investigation involves a number of devices and phenomena, of which a considerable amount of literature is available. This is partly due to the nuclear field where the inherent dangers of nuclear fission have resulted in a highly technical industry with an enormous amount of academic literature available. The literature survey was conducted with this in mind in an effort to briefly condense the main aspects relating to the proposed concept.

On the nuclear side, the literature survey provides a brief history of nuclear power and its current state. The concept of small and medium reactors is then briefly discussed mentioning current concepts with similar features to the proposed system. The literature survey then highlights the work of the Generation IV International Forum, explaining where the concept under consideration fits in. Previous work on flash-tube type natural circulating reactors is used to explain its workings whilst also mentioning the original design objectives which align with that of the concept's main objective of inherent safety. This is followed by a brief acknowledgement of findings made during the investigations conducted on natural circulating BWR concepts.

The survey then shifts focus to thermosyphon loops and heat pipes explaining their workings, application in the nuclear field and modelling. A discussion is presented on the instabilities of natural circulating loops differentiating between static and dynamic instabilities. The challenges of modelling a two-phase flow system and the homogeneous model is then discussed, with a brief overview of where the homogeneous model fits in with respect to other more complex models.

2.1 Nuclear Technology

In 1939 it was discovered that the nucleus of an atom could be split or fissioned by a neutron into two or more pieces. Though offering no immediate possibility of useful application, it was further found that the fissioning of uranium-235 released on average 2.5 neutrons thus making a self-sustaining chain reaction possible. The feasibility of a chain reaction led to the construction of the first reactor which went into operation on the afternoon of December 2, 1942 at the university of Chicago (King, 1964).

This propitious occasion was the beginning of the nuclear era which has resulted in 229 operational research reactors as of August 2012 and 437 power generation reactors in operation (with a total capacity of 372.1 GW_e) and a further 67 under construction at the end of 2013. The current distribution of the operational power generating reactors is as follows: 84-BWRs; 273-PWRs; 48-Pressurized heavy water reactors (PHWR); 15-Light water cooled graphite moderated reactors (LWGR); 15-Gas cooled reactors (GCR) and 2-Fast reactors (FR) (IAEA Director General, 2013).

Despite the principal function of today's reactors being that of electricity production, a number of them are also used for district heating, desalination and process heat. Future non-electric uses possibly include hydrogen production and the upgrading of low quality petroleum resources.

2.1.1 Small and medium sized reactors

The nuclear industry has historically pursued economies of scale, however, there is growing interest in small (<300 MW_e) and medium (>300, <700 MW_e) sized reactors (SMRs). This is because SMRs allow smaller, incremental and more flexible investment over time. There are approximately 45 innovative SMR concepts at some stage of research and development. Areas of application for SMRs under development include: desalination; electrical generation; transportable and modular power generation; liquid sodium cooled fast reactors; co-generation of electricity and process heat; prototype fast breeder reactors and powering ice breakers (IAEA Director General, 2013).

Most SMRs are designed to be inherently safe with many having similar features to the proposed concept of this thesis. Some of these SMRs are shown in Table 2.1.1.

Table 2.1: Notable SMRs description and features

Reactor	Features	Distinguishing Features
CAREM (CNEA, Argentina) Integral PWR	EC: 25 MW_e TC: 100 MW_{th} C/M: Light water PC: Natural circ. ESS: Passive RHRS: Passive	Pressurizer and steam generators (SGs) inside reactor pressure vessel and vessel is self-pressurised. Pressure suppression containment. CAREM safety systems are based on passive features allowing for a 32 hour grace period when neither automated control power or operator actions are required (IAEA, 2012).
IMR (Mitsubishi Heavy Industries, Japan) Integrated modular BWR	EC: 350 MW_e TC: 1000 MW_{th} C/M: Light water PC: Natural circ. ESS: Passive RHRS: Active	Reactor with an integrated primary system. Steam generators in liquid and vapour regions of the vessel (IAEA, 2012).
SMART (KAERI, Republic of Korea) Integral PWR	EC: 100 MW_e TC: 330 MW_{th} C/M: Light water PC: Forced circ. ESS: Active/ passive RHRS: Passive	Coupling of the desalination system or process heat application. Incorporates engineered safety systems: a reactor shut down system; a safety injection system; a passive reactor heat removal system; a shutdown cooling system; a containment spray system (IAEA, 2012).

EC-Electrical capacity; TC-Thermal capacity; C/M-Coolant/Moderator; PC-Primary circulation; ESS-Emergency safety systems; RHRS-Residual heat removal systems (Table continues on next page)

Reactor	Features	Distinguishing Features
ABV-6M (OKBM Afrikantov, Russian Federation) PWR	EC: 8.6 MW_e TC: 38 MW_{th} C/M: Light water PC: Natural circ. ESS: N/A RHRS: N/A	Natural circulation in the primary circuit for land based and floating nuclear power plants. Core life time without refuelling or shuffling of fuel is 10 years (IAEA, 2012).
VK-300 (RDIPE, Russian Federation) BWR	EC: 250 MW_e TC: 750 MW_{th} C/M: Light water PC: Natural circ. ESS: Passive RHRS: Passive	Cogeneration BWR based on operating VK-50 prototype. The VK-300 uses a metal lined reinforced concrete primary containment (IAEA, 2012).
UNITHERM (RDIPE, Russian Federation) PWR	EC: 2.5 MW_e TC: 20 MW_{th} C/M: Light water PC: Natural circ. ESS: Passive RHRS: Passive	Unmanned reactor operation with long and uninterrupted irradiation of fuel inside reactor core throughout the whole reactor lifetime due to UNITHERM fuel cycle. Makes use of extensive passive systems and devices based on natural processes without the requirement of external energy (IAEA, 2012).
IRIS (IRIS, International consortium) Integral PWR	EC: 335 MW_e TC: 1000 MW_{th} C/M: Light water PC: Forced circ. ESS: Passive RHRS: Passive	Integral primary system configuration with simplified compact design where the primary vessel houses the steam generators, pressuriser and pumps eliminating or reducing the probability of a variety of accidents (IAEA, 2012).
mPower (Babcock & Wilcox, USA) Integral PWR	EC: 180 MW_e TC: 530 MW_{th} C/M: Light water PC: Forced circ. ESS: Passive RHRS: Passive	Integral once-through steam generator, pressurizer and control rod drive mechanism. Reactor deploys a decay heat removal strategies with passive heat exchanger connected to ultimate heat sink, auxiliary steam condenser on secondary circuit, cavity flooding and passive containment cooling (IAEA, 2012).
NuScale (Nuscale Power Inc., USA) Integral PWR	EC: 45 MW_e TC: 160 MW_{th} C/M: Light water PC: Natural circ. ESS: Passive RHRS: Passive	Synergy through plant simplicity; reliance on existing light water technology and availability of an integral test facility. Design safety features include high pressure containment vessel, two passive decay and containment heat removal systems and a shutdown accumulator (IAEA, 2012).

EC-Electrical capacity; TC-Thermal capacity; C/M-Coolant/Moderator; PC-Primary circulation; ESS-Emergency safety systems; RHRS-Residual heat removal systems (Table continues on next page)

Reactor	Features	Distinguishing Features
Westinghouse SMR (Westinghouse, USA) Integral PWR	EC: 225 MW_e TC: 800 MW_{th} C/M: Light water PC: Forced circ. ESS: Passive RHRS: Passive	Incorporates passive safety systems and proven components of the AP1000 reactor utilising four heat exchangers connected to two ultimate heat sinks for decay heat removal. Westinghouse claims no operator intervention is required for seven days following an incident (IAEA, 2012).
AHWR300-LEU (BARC, India) Pressure tube type heavy water moderated reactor	EC: 304 MW_e TC: 920 MW_{th} C/M: Light water/ heavy water PC: Forced circ. ESS: Passive RHRS: Passive	The reactor is designed to use a mixed oxide thorium closed in fuel cycle, recovering U233 and thorium from spent fuel to be used to manufacture fresh fuel. The primary C/M boiling light water and is driven by natural circulation through vertical cooling channels (IAEA, 2012).
PRISM (GE-Hitachi, USA) Liquid metal cooled fast breeder reactor	EC: 311 MW_e TC: 840 MW_{th} C/M: Sodium PC: Forced circ. ESS: Passive RHRS: Passive reactor vessel aux. cooling	System consists of underground containment facility with, seismic isolators and a passive air cooled ultimate heat sink. The reactor forms part of the advanced recycling centre for spent nuclear fuel. The reactor uses passive shutdown and decay heat removal features (IAEA, 2012).
SMR-160 (Holtec International LLC, USA) PWR	EC: 145 MW_e TC: 446 MW_{th} C/M: Light Water PC: Natural circ. ESS: Passive RHRS: Passive	Located deep underground. Designed to be passively cooled for normal shut-down. The reactor C/M continues to circulate through a thermosyphoning action during accident scenarios. No active pumps are required to run the reactor (HOLTEC International, 2013).
TH-100 (STL, South Africa) Gas cooled pebble bed reactor	EC: 35 MW_e TC: 100 MW_{th} C/M: Helium PC: Forced circ. ESS: Passive RHRS: Passive	Thorium pebble bed based fuel cycle. Meltdown proof core due to low power density (3.8 MW/m^3) and a strong negative temperature coefficient. No phase change and pressure build up as in LWR and helium is inert (STL, 2011).

EC-Electrical capacity; TC-Thermal capacity; C/M-Coolant/Moderator; PC-Primary circulation; ESS-Emergency safety systems; RHRS-Residual heat removal systems

2.1.2 Generation IV

The Generation IV International Forum (GIF) came about from a framework for international cooperation in research, for a future generation of nuclear energy systems between 10 countries. The countries included are Argentina, Brazil, Canada, France, Japan, the Republic of Korea, the Republic of South

Africa, Switzerland, the United Kingdom, and the United States. The different generations of nuclear plants and their respective eras, as defined by GIF, are shown in Figure 2.1.

GIF's road map process culminated in the selection of six Generation IV systems for further research and development, namely: Gas-Cooled Fast Reactor System; Lead-Cooled Fast Reactor System; Molten Salt Reactor System; Sodium-Cooled Fast Reactor System; Very-High-Temperature Reactor System (Generation IV International Forum and U.S. DOE Nuclear Energy Research Advisory Committee, 2002). Although the six chosen systems make significant advances in the furthering of nuclear technology they have little in common, from a system and operational perspective, with the novel concept under consideration in this thesis. The design concept under consideration does, however, share the design goals (as outlined in section 1.1) of GIF and due to its novel nature could be classified as a Generation IV+ system.

2.1.3 Flash-tube and natural circulating systems

A few small, low-pressure light water reactors (LWRs), with boiling taking place in a riser section above the core were proposed for mainly district heating applications (Yadigaroglu and Zeller, 1994). One such reactor is the GEYSER-concept, as proposed by Vecsey and Doroszlai (1988), which is an entirely passive LWR concept that was designed to be inherently safe. These requirements, as stated by Vecsey and Doroszlai (1988), required the systems to have:

1. Credible and convincing passive safety, based on simple natural laws (inherently safe).
2. Safe engineering instead of engineered safety, involving simple deterministic processes instead of probabilistic considerations.
3. Simple and approved components and systems based on widespread and

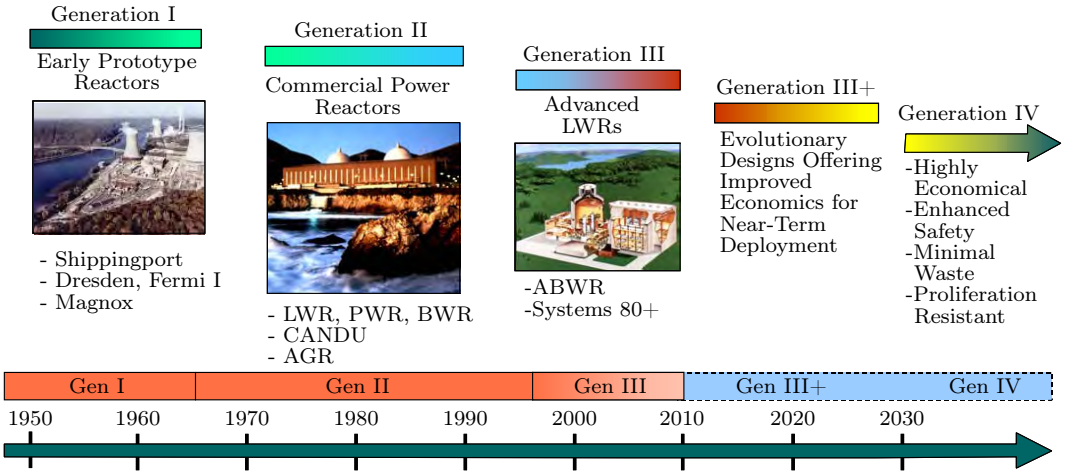

Figure 2.1: Overview of the generations of nuclear energy systems as classified by GIF (Generation IV International Forum and U.S. DOE Nuclear Energy Research Advisory Committee, 2002)

well known technology.

4. Simple unmanned operation with walk-away safety.
5. Complete exclusion of human influence on safety related processes.
6. Nuclear maintenance at site minimised to the simple and safe replacement of the core.
7. Maximum available core life.

These requirements for GEYSER are similar to the goals of the system under consideration, with points one and two being of particular importance. The major difference between GEYSER's requirements and the design concept is that the design concept is not pursuing the goals for public acceptance, as stated by Vecsey and Doroszlai (1988), but rather from one of a fundamental responsibility to the public and environment.

The primary loop of the proposed system is similar to the one as mentioned in the work of Yadigaroglu and Zeller (1994), as seen in Figure 2.2. The operation, as explained by Yadigaroglu and Zeller (1994), is as follows: Flashing of the water into steam takes place in the adiabatic riser section of the loop and is a result of the hydrostatic reduction of pressure as the fluid rises (see Figure 2.2). With the steam saturated in the steam space, the water entering the down-comer is saturated but, becomes subcooled as it progresses downwards with the increase in hydrostatic pressure. Energy is added to the fluid in the core, however, the fluid remains subcooled somewhat due to the throttling above the core. The fluid rises up the riser and flashes where the enthalpy of the fluid matches that of the local saturation enthalpy.

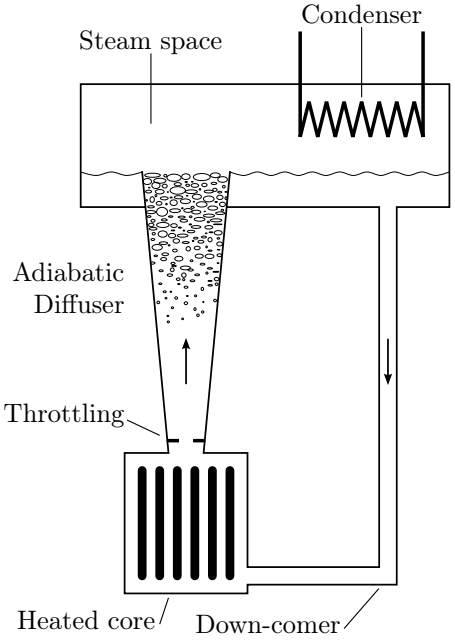

Figure 2.2: Schematic of the flash-driven natural-circulation primary loop (Yadigaroglu and Zeller, 1994)

The transient behaviour of a natural circulating BWR is discussed by Aritomi *et al.* (1992) and Chiang *et al.* (1994). They indicate that if thermo-hydraulic instabilities were to occur during the plant start up, it could influence the reactivity, thus hampering the raising of the power output. Chiang *et al.* (1994) concludes that as the system pressure is increased, the regions where natural circulation oscillations occur becomes narrower, which also suppresses geysering. This being said, the riser section should prevent boiling in the core, thus reducing the influence on the reactivity; the influence of instabilities should, however, be investigated. Aritomi *et al.* (1992) also recommends that large-scale proof testing would be required to understand the start-up processes in a BWR.

2.2 Thermosyphon Loops and Heat Pipes

A thermosyphon loop is a thermodynamic device that transfers heat through passive heat exchange driven by natural circulation. A thermosyphon loop operates by heating the working fluid on the one side and cooling the fluid on the other side of the loop. This results in the warm leg being less dense than the cold leg which induces a buoyancy driven flow, transporting the hot liquid up, round and down to the cool leg and the cool liquid down, round and up to the hot leg. The hot liquid is then cooled and the cold liquid heated, continuing the process.

A closed loop thermosyphon type heat pipe uses the same principle but the flow and transfer of heat is driven through phase change and subsequent large density differences. Heat is transferred utilizing the latent heat of vaporisation. This thermosyphon type heat pipe allows for a more flexible positioning of the condenser (which replaces the cold leg) as the condensate must find its way back to the evaporator (which replaces the hot leg). In most current heat pipe applications, which are typically small in size, this takes place through the capillary action of a wick within the heat pipe which allows the pipe to be placed in any orientation (Vasiliev, 2005). However, for the purposes of the design concept, the secondary loop is considerably larger than typical applications and utilises a gravity return feed. The gravity return feed forces the condenser to be above the evaporator so that the condensate can flow back to the evaporator. The return channel is also separated from the vapour channel to avoid entrainment of the condensate by the vapour, thus enhancing overall heat transfer. The condensate also enters the heat pipe at the lowest point to prevent reverse flow.

Closed loop thermosyphon type heat pipes have been proposed for application in the nuclear field, predominantly for reactor cavity cooling systems as in the works of Verwey (2010), Ruppersberg (2008), Sittmann (2011) and Papini and Cammi (2010), and for waste heat recovery by Senda (2012). The design concept of utilising the secondary loop as a heat transfer mechanism between the primary loop and the steam generators was not found to have yet been researched or investigated.

Prediction of the workings of a two-phase flow loop thermosyphon is a complicated matter as the processes involved are complex and not yet fully understood. Verwey (2010), Ruppersberg (2008) and Sittmann (2011) do, however, provide a good conceptual understanding of the inner workings of the two-phase thermosyphon loop. Lee *et al.* (2003) found during their investigations that a computer simulation can predict most of the parameters involved in modelling a two-phase thermosyphon loop reasonably well, but, only when correct empirical heat transfer correlations are used. Ruppersberg (2008) also concluded that computer simulations without experimental validation cannot deliver quantitative results.

2.3 Natural Circulating Loop Instabilities

Instabilities and fluctuations are often present in natural circulation systems. Single-phase and two-phase natural circulating loops (NCLs) can exhibit unstable behaviour but, under forced circulation only a two-phase system can be subjected to instability. Wissler *et al.* (1956) was one of the first to report on the instability of two-phase natural circulating systems (Bhattacharyya *et al.*, 2012). A systematic classification of the different instabilities observed in two-phase flow was first presented by Boure *et al.* (1973).

Flow can be defined as stable if, when the system experiences a small disturbance, it asymptotically approaches back to the existing operation conditions. Two types of instabilities have universally been classified, namely, static and dynamic. The system is said to be subject to a static instability, if, when the operating conditions are modified by a small amount and it is not possible to regain a steady state close to the previous one. Dynamic instability however depends upon the dynamic interactions of flow variables and the feedback effect (Bhattacharyya *et al.*, 2012).

2.3.1 Two-phase static instabilities

Static instabilities can produce large excursions of flow in an NCL with the threshold able to be predicted from steady state results. When determining the nature of a static instability the pressure drop characteristics, nucleation properties and flow regime transition are important. Due to the sudden variation in flow rates the critical heat flux is strongly influenced by static instabilities. Typical examples of static instability are flow excursion, flow patterns, transition instability and geysering (Bhattacharyya *et al.*, 2012).

2.3.1.1 Ledinegg-type instability

Ledinegg-type instability is generally classified by a sudden change in flow rate to a very low value or by flow reversal . The instability occurs in NCLs when the internal characteristic curve (pressure drop versus flow rate curve) of the loop has a smaller slope than the external characteristic curve, mathematically, this is represented as,

$$\left.\frac{\partial \Delta P}{\partial G}\right|_{internal} \leq \left.\frac{\partial \Delta P}{\partial G}\right|_{external} \tag{2.1}$$

(Boure *et al.*, 1973). These conditions are encountered when the pressure drop decreases with an increase in flow rate for instance in a system with sub-cooled boiling flow with high heat supply (Bhattacharyya *et al.*, 2012).

The instability is very commonly encountered in two-phase NCLs and is known to be problem in low pressure boiling systems. To avoid a Ledinegg instability a steeper external characteristic can be forced by throttling the flow. An increase in the system pressure can also stabilize the system (Bhattacharyya *et al.*, 2012).

2.3.1.2 Geysering-based instability

Geysering is found in systems where the liquid is heated close to the bottom of a long vertical channel or riser. If the heat supply is high enough a large amount of vapour is generated at the base of the riser section. This vapour generation results in a decrease in hydrostatic head and the bubbles are forced into the riser section. Sub-cooled liquid then returns to the heated sections and the cycle is repeated. The bubbles generated in the heated section, mixing with the sub-cooled liquid in the riser, can condense in the riser resulting in flow reversal or flow excursion.

This state is generally associated with a low flow and low pressure condition typically found during start-up in BWRs. Geysering in a reactor start-up due to a coupling of power and flow can cause the system to undergo power oscillations due to the strong reactivity feedback and void fluctuations within the core (Bhattacharyya *et al.*, 2012). This type of instability has received abundant attention in the last number of decades with Aritomi *et al.* (1992, 1993) performing some of the pioneering research (Bhattacharyya *et al.*, 2012).

Paniagua *et al.* (1999) noted the shortcoming of time-domain computational codes when dealing with start-up transients. Using a four-equation drift flux model a significant improvement was made when local pressure values based on local pressure distribution were used instead of system average values. The reduction of void fraction due to higher system pressure was reported to suppress geysering and a reduction in inlet sub-cooling was found to reduce geysering (Bhattacharyya *et al.*, 2012).

2.3.1.3 Instabilities associated with flow pattern transition instability

Flow pattern transition instability appears due to the differing pressure drop characteristics of different flow regimes. This form of instability may result in the flow rate varying from very high to low or vice versa. It is generally of greater significance than Ledinegg instabilities in two-phase NCLs and when the system operates near a transition point, small changes in flow rate can result in sustained oscillations.

Nayak *et al.* (2003), employing a one-dimensional two-phase homogeneous model and a drift-flux-type method to estimate the steady state pressure drop, have proposed the only significant analytical model for this type of instability Bhattacharyya *et al.* (2012). Nayak *et al.* (2003) mentions that the lack of experimental data in literature for flow pattern transition instability is due

to the possibility of the instability triggering other dynamic instabilities. The system then may experience a compound instability which makes it difficult to identify and separate each instabilities data in experiments (Nayak *et al.*, 2003). Nayak *et al.* (2003) came to the conclusion that the instability decreases with an increase in core inlet resistance or an increase in diameter of the riser pipe with investigated diameter sizes ranging from 75 to 300 mm.

2.3.2 Two-phase dynamic instabilities

Dynamic instability is generally of more importance than static instability to NCLs. A system subjected to a dynamic instability can experience large changes in circulation rate from very high to very low or vice versa, along with the possible presence of chaotic oscillations as well. The prediction of dynamic instability just from steady-state equations is impossible thus dynamic or transient characterization is required (Bhattacharyya *et al.*, 2012).

2.3.2.1 Density wave oscillations

Two types of density waves were classified by Fukuda and Kobori (1979), namely, type I and type II. Type I instability is governed by gravitational head and presents itself at low vapour qualities in contrast, type II appears at high vapour quality and is friction dominated (Fukuda and Kobori, 1979).

Type I instabilities' dependence on the gravitational head, means that the vertical riser section plays and important role. At a near-zero steam quality state a small change in flow rate can lead to a large change in void fraction due to the steep slope of the void fraction versus quality curve in initial phases. This large change results in a large change in the driving buoyancy force of the of the fluid and can result in a rapid increase of flow rate. With a constant input power the increase in flow rate can then reduce the quality in-turn reducing the flow again. This type of instability is characteristic of low power operation. A decrease in riser size can suppress the oscillations (Bhattacharyya *et al.*, 2012).

When the power input is increased the void fraction becomes less sensitive to changes in quality and can be observed to be stable. This is true until the frictional losses, that increase with an increase in exit quality, become dominant, reducing the flow for an increase in heating power. Type II instabilities thus appear with very high void fractions with the frictional forces governing the flow rate (Bhattacharyya *et al.*, 2012).

The prediction of such oscillations is not always possible with linear methods and thus nonlinear techniques have found popularity in the recent past. One-dimensional homogenous flow model has been utilised by Clausse and Lahey Jr (1991) and given predictions similar to experimental observations. Clausse and Lahey Jr (1991) found that their simple model yielded a rich variety in nonlinear phenomena. This lay the path for models also incorporating the neutron kinetics which, when combined with the instabilities, were observed to have strong effects on the dynamics of a BWR (Bhattacharyya *et al.*, 2012).

2.3.2.2 Flashing-induced instability

Flashing-induced instabilities are most commonly found during low-pressure operation and during the start-up of BWRs. Flashing-induced oscillations, which cause instabilities, are observed usually when the fluid reaches saturation in the riser section. Although it is similar to geysering with similar pressure level and large bubble presence, in the riser, it is a form of pure dynamic instability (Bhattacharyya *et al.*, 2012).

The mode of vapour generation is different to geysering as the liquid flashes into vapour along the flow path up the riser due to the reduction in hydrostatic pressure head and saturation enthalpy. The strong dependence of saturation enthalpy upon pressure, particularly at low pressure levels, implies that such void flashing is more important at lower pressures. As found with a type I density wave oscillation, the steep slope of the void fraction versus quality curve for lower qualities, means flashing can induce a large change in void fraction and in turn affect the driving gravitational head and is sometimes referred to as type I density wave oscillation. The change in driving head can result in a flow rate increase which in turn lowers the vapour quality in the core and riser resulting in a thermal hydraulic feedback which can cause self-sustained oscillations (Bhattacharyya *et al.*, 2012).

Wissler *et al.* (1956) first mentioned the possibility of the existence of flashing-induced instabilities through the observation of periodic flow oscillations in a low-pressure system. Their simple model, with one-dimensional conservation equations integrated around the loop, allowed for the dominating effect of the driving force generated by the riser to be noticed. Furthermore, their model estimated that the product of coefficient of expansion of a fluid and riser height must exceed a certain value for sustained oscillations (Bhattacharyya *et al.*, 2012). More recently Furuya *et al.* (2005) have illustrated an excellent discussion on the mechanism of flashing with the SIRUS-N facility which had a chimney/riser of 5.7 m and operating pressures of 0.1 to 0.5 MPa.

Manera *et al.* (2006) found that most existing experiments and models available in literature, relating to flashing, mainly refer to flashing in horizontal pipes as a result of sudden depressurisation. This literature cannot be directly applied to flashing flows in vertical pipes caused by the variation of gravitational head. Furthermore, Manera *et al.* (2006) found that literature is scarce focusing on steam-water flows with a heated section below an adiabatic test section and little is known about flashing flows which flash due to a drop in gravitational head along the system. This prompted Manera *et al.* (2006) to perform an experimental three-dimensional reconstruction and visualisation of stationary and transient flashing flows in a vertical pipe with a diameter of 47 mm.

2.4 Two-phase Flow Modelling

There are a large number of computer codes that have been developed to analyse, design, and operate complex two-phase flow systems. System computer

codes must not only simulate the phenomena and processes but also the subsystems. This difficulty is exacerbated by the complications of dealing with two-phase flow (Levy, 1999).

Two-phase flow can introduce many complications, as discussed by Levy (1999), such as:

- In single-phase modelling all the properties of the fluid are known. Whereas in two-phase flow the velocity, thermal conductivity and viscosity differs between the two states, thus introducing at least three unknowns.
- A gas-liquid interface exists between the two phases allowing for the transfer of mass, moment and energy. Furthermore, the interfaces and transfer mechanisms are hard to determine experimentally and are not yet fully understood.
- The two phases can form a multitude of flow patterns such as bubbly, dispersed, stratified, annular, slug and churn flow. All of which could affect fluid density, pressure drop and heat transfer.
- Further degrees of freedom, of two-phase flow, when compared to single-phase flow, include, co-current and counter-current flow; the presence of mechanisms such as condensation, evaporation and mass transfer and thermal non-equilibrium between the phases.
- The response time to transients for a two-phase flow system can be very slow (quasi-steady state) to very quick, reaching sonic velocities.

The computer codes historically originated using homogeneous models (Furutera, 1986) utilising uniform flow and thermal conditions. They then evolved into separated flow models which dealt with the differences between phases in gas-liquid flow without addressing the interfaces, flow patterns or any non-thermal equilibrium conditions. More recent codes execute two-fluid models also recognizing flow patterns and interface exchanges. The development of computer codes was only made possible after a large number of simplifications, assumptions and validation against experimental data took place (Levy, 1999).

The homogeneous model, also referred to as the homogeneous equilibrium mixture model, is the simplest of the two-phase transport models (Reyes, 2005). The homogeneous model presumes equal gas and liquid velocity (homogeneous) and that both phases are at saturated conditions, thus forgoing the need to consider the interfaces. The thermodynamic properties of each fluid phase can be approximated as a function of saturation pressure due to the assumption of equilibrium conditions (Reyes, 2005). The model requires expressions for the homogeneous viscosity and thermal conductivity. As the model assumes equal gas and liquid velocities, it can employ all the single-phase closure laws, thus giving it the ability to be run on a uniform property (single-phase) code with no adjustments to the existing analyses and empirical correlations (Levy, 1999). The homogeneous state is, however, only approached when the gas and liquid properties are similar, $\rho_l/\rho_g < 10$, or for high mass fluxes in excess of $2\,000\,\mathrm{kg/m^2{\cdot}s}$ and large pressure drops (Whalley, 1987).

Homogeneous/uniform property code is an important default tool for the development of system codes (Levy, 1999). The homogeneous computer codes are much easier to develop and implement, while they have the added benefit of typically being more computationally efficient which results in reduced simulation times. The main shortcoming of the model is that it presumes equal gas and liquid temperatures and velocities, modelling the mixture as a single incompressible fluid. This idealisation is justified only for flows that have rapid interfacial rates of energy and momentum transfer. The homogeneous model is therefore applicable when the two phases are well mixed across the cross sections such as mist or bubbly flow (Bhattacharyya *et al.*, 2012). The model can be used as a basis for developing other separated flow models with no interface exchange such as the *Lockhart-Martinelli* Model, *Martinelli-Nelson* model and drift flux model. These models attempt to compensate for the differing velocities but still suffer from the avoidance of dealing with the detailed structure of two-phase flow.

Two-fluid models that incorporate interface exchanges are currently used widely as they are able to handle differing gas and liquid velocities, flow directions and temperatures. Many of the models, however, still rely on one-dimensional formulations and upon time and spatial averaging. This means that the models do not deal with the properties (e.g. temperature and velocity) and their gradient variations at the interfaces or wall boundaries. Thus, the models require closure laws that are known to depend on the flow pattern, meaning flow regime maps must also be specified (Levy, 1999).

Ruppersberg (2008) and Levy (1999) are in agreement that a computer simulation without experimental validation cannot deliver quantitative results.

3 Theoretical Modelling of the Primary Loop

This chapter deals with the formulation of theory and a solution algorithm for the theoretical simulation of the primary loop illustrated in Figure 1.1. The theoretical model was used to predict the operation of the primary loop under varying conditions using a simple computationally efficient computer algorithm. The chapter begins with the general assumptions made in the analysis. The applicable theory is developed and the physical features of the theoretical model are discussed. The final section discusses the computer algorithm used, and the steps executed, to solve the theoretical model.

3.1 Assumptions

The following assumptions are made in the analysis of the primary loop's theoretical model:

- One-dimensional or so-called plug flow is assumed, implying that the average velocity is constant over the flow cross-sectional area.
- Any pressure difference of the fluid in the loop due to temperature induced density gradients, are small compared to the absolute pressure. This implies that the pressure is essentially constant at any elevation in the loop, resulting in a so-called hydrostatic problem. Thus the pressure, P, is a function of height only i.e: $P{=}f(\Delta z)$. The Boussinesqu approximation for natural convection for the volumetric expansion co-efficient, in the buoyancy term of the equation of motion, may be applied, if so desired.
- No super-heating of the fluid is possible.
- Liquid and vapour phases are at all times in thermal equilibrium with each other.
- The loss due to friction or changes in kinetic and potential energy in the conservation of energy equations are negligible when compared to the heat transfer and flow energy.
- The vapour and liquid phases are both assumed incompressible.
- The liquid and vapour phases are modelled as a homogeneous fluid.
- As per objective 3 a so-called *quasi-equilibrium* condition as defined by Dobson (2012) is assumed. A so-called *quasi-equilibrium* condition implies that the speed of sound in the working fluid is considerably greater than the particle speed or average fluid velocity. Therefore information, such as expansion or contraction of a control volumes contents, is assumed to be transported/communicated around the loop instantaneously. [Utilising the quasi-equilibrium condition as well as the fluid incompressibility, at any instant in time, although the density and average velocity of the working fluid might change around the loop, the volumetric flow rate, G, is constant for all positions around the loop. Hence the mass flow rate at any position i

is $\dot{m}$=$\rho_i G$ where i denotes an arbitrary control volume as seen in Figure 3.1.]

- The effects of thermal expansion and contraction on the physical size of components are negligible.
- A fully explicit solution method is used so that the time derivative of any property becomes

$$\frac{dX}{dt} = \frac{\Delta X}{\Delta t} = \frac{X^{t+\Delta t} - X^t}{\Delta t} \tag{3.1}$$

where X is the property, t is the current time and $t + \Delta t$ is the next time step with a duration Δt.

As the liquid, l, and gas, g, components are modelled as a homogeneous substance, the following definitions are applicable. These definitions allow for the calculation of the thermo-physical properties of the fictitious fluid, providing closure for the solution algorithm. For a single control volume i, as shown in Figure 3.1 (a), consisting of both liquid, l, and gas, g, phases the mass fraction of vapour for the control volume i is defined as

$$x_i = \frac{m_{i,g}}{m_{i,l} + m_{i,g}} \tag{3.2}$$

and the void fraction as

$$\alpha_i = \frac{V_{i,g}}{V_{i,l} + V_{i,g}} = \frac{V_{i,g}}{V_i} \tag{3.3}$$

when the void fraction is written in terms of the density and mass fraction it becomes

$$\alpha_i = \left(1 + \frac{1 - x_i}{x_i} \frac{\rho_{g,sat@T_i}}{\rho_{l,sat@T_i}} SR\right)^{-1} \tag{3.4}$$

where SR is the slip ratio. For homogeneous flow only $SR = 1$ and hence the density of a homogeneous control volume is

$$\rho_i = \alpha_i \rho_{i,g} + (1 - \alpha_i)\rho_{i,l} \tag{3.5}$$

The enthalpy of the homogeneous control volume is

$$h_i = h_{i,l}(1 - x_i) + x_i h_{i,g} \tag{3.6}$$

and the viscosity as suggested by Whalley (1987) is

$$\mu_i = 1/\left[x_i/\mu_g + (1 - x_i)/\mu_l\right] \tag{3.7}$$

3.2 Applicable Theory

In this section the theory is presented from conception until the basic form used in the theoretical model is obtained. This section begins with the control volumes and then derives the equations for conservation of mass, momentum and energy using the assumptions stated in section 3.1.

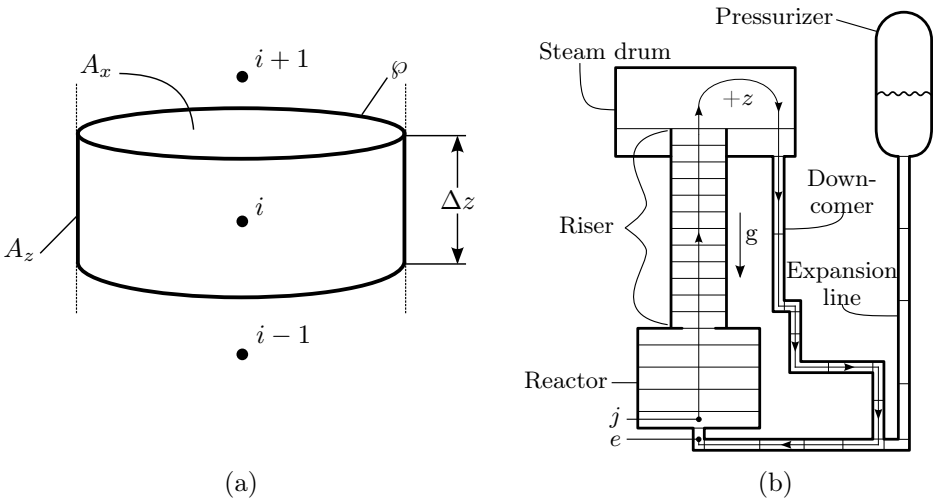

Figure 3.1: (a) Geometric description and (b) the layout of control volumes

3.2.1 The basic control volume and model layout

As per the selected method of analysis a one-dimensional control volume for the i^{th} control volume is shown in Figure 3.1 (a). $\wp$ is the wetted perimeter, A_x the cross sectional area through which the flow passes, Δz the length of a control volume and $A_z = \wp \Delta z$ is the circumferential area.

A general layout of the control volumes, in a simple schematic of the loop and expansion line, is shown in Figure 3.1 (b) with the direction of gravity, g, indicated. The loop consists of the reactor, the riser, the steam drum and the down-comer sections. The positive flow direction in the loop, $+z$, is clockwise (as indicated in Figure 3.1 (b) by the line with arrows) starting at control volume j and ending at e. Integration/summation around the loop begins at control volume j, going up against the force of gravity, and ends at e after coming down through the down-comer where the gravitational force is positive. The control volumes are not necessarily all cylindrical in shape as in the case of the steam drum and reactor sections of the model, which are rectangular.

3.2.2 Mass conservation

Applying the law of the conservation of mass to a control volume as seen in Figure 3.2 (a) one obtains

$$\frac{\Delta m_i}{\Delta t} = \sum \dot{m}_{in} - \sum \dot{m}_{out} \qquad [\text{kg/s}] \tag{3.8}$$

or rearranged using the assumption for the time derivative

$$m_i^{t+\Delta t} = m_i^t + \Delta t \left[\sum \dot{m}_{in}^t - \sum \dot{m}_{out}^t \right] \qquad [\text{kg}] \tag{3.9}$$

Utilising the assumption $\dot{m} = \rho G$ with G constant, for a quasi-equilibrium state in the loop, equation 3.9 becomes

$$m_i^{t+\Delta t} = m_i^t + \Delta t |G^t| \left[(\rho)_{in}^t - (\rho)_{out}^t \right] \qquad [\text{kg}] \tag{3.10}$$

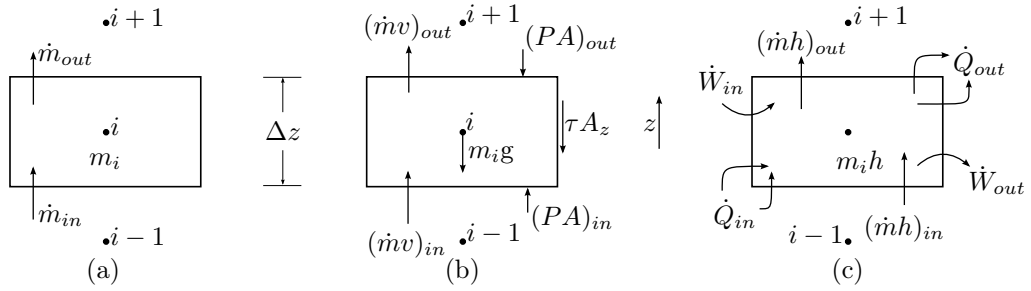

Figure 3.2: (a) Mass, (b) Momentum and (c) Energy conservation applied to the control volume respectively

3.2.3 Momentum conservation

Using the second control volume and applying the conservation of momentum, as shown in Figure 3.2 (b), gives

$$\frac{\Delta(mv)}{\Delta t} = (\dot{m}v)_{in} - (\dot{m}v)_{out} + P_{in}A_{x,i} - P_{out}A_{x,i} - \tau A_{z,i} - m_i(\pm \mathrm{g}) \qquad [\mathrm{N}] \quad (3.11)$$

but with reference to Figure 3.1 (a)

$$\dot{m} = \rho v A_x = \rho G \qquad [\mathrm{kg/s}]$$

$$m = \rho A_x \Delta z \qquad [\mathrm{kg}]$$

and thus at any cross-section the velocity is

$$v = \frac{\dot{m}}{\rho A_x} = \frac{G}{A_x} \qquad [\mathrm{m/s}] \quad (3.12)$$

however the velocity entering or leaving the i^{th} cell is based on the minimum entrance and exit areas respectively. Using the above manipulations equation 3.11 becomes

$$\frac{\Delta\left(\rho_i A_{x,i}\Delta z_i \left(\frac{G}{A_{x,i}}\right)\right)}{\Delta t} = \left(\frac{\dot{m}G}{\min(A_x)}\right)_{in} - \left(\frac{\dot{m}G}{\min(A_x)}\right)_{out} + P_{in}A_{x,i} - P_{out}A_{x,i} - \tau A_{z,i} \pm \mathrm{g}\left(\rho A_x \Delta z\right)_i \qquad [\mathrm{N}] \quad (3.13)$$

where $\min(X)$ is a function which returns the minimum value of given set of values, X. For each control volume the cross-sectional area is constant thus dividing 3.13 through by $A_{x,i}$ for the current control volume, noting that *out* is the flow leaving the i^{th} control volume with its properties, and using the definition for $\dot{m}$ gives

$$\frac{\Delta\left(\frac{\rho_i \Delta z_i G}{A_{x,i}}\right)}{\Delta t} = \left(\frac{\rho_{in}G^2}{\min(A_{x,in})}\right)/A_{x,i} - \left(\frac{\rho_i G^2}{\min(A_{x,out})}\right)/A_{x,i} + P_{in} - P_{out} - \tau A_{z,i}/A_{x,i} \pm \mathrm{g}(\rho\Delta z)_i \qquad [\mathrm{Pa}] \quad (3.14)$$

Then by utilising the Boussinesq approximation and integrating around the loop, which in the case of a discretized loop equates to summing around the loop, the summation of the pressure term is

$$\sum_{j}^{e}[P_{in} - P_{out}] = 0 \tag{3.15}$$

Following the direction, $+z$, as shown in Figure 3.1 (b) and summing, equation 3.14 becomes

$$\frac{\Delta}{\Delta t}\left[\sum_{j}^{e}\frac{\rho_i \Delta z_i G}{A_{x,i}}\right] = \sum_{j}^{e}\left[\left(\frac{\rho_{in}G^2}{\min(A_{x,in})}\right)/A_{x,i} - \left(\frac{\rho_i G^2}{\min(A_{x,out})}\right)/A_{x,i}\right] - \sum_{j}^{e}\left[\tau\frac{A_{z,i}}{A_{x,i}}\right] + \sum_{j}^{e}(\pm \mathrm{g}\rho_i \Delta z_i) \qquad [\mathrm{Pa}] \tag{3.16}$$

and using the assumption that G is constant around the loop for a specific time step and defining the separate components of the momentum equation as

$$M = G^2 \sum_{j}^{e}\left[\left(\frac{\rho_{in}}{\min(A_{x,in})}\right)/A_{x,i} - \left(\frac{\rho_i}{\min(A_{x,out})}\right)/A_{x,i}\right] \tag{3.17}$$

$$F = \sum_{j}^{e}\left[\tau\frac{A_{z,i}}{A_{x,i}}\right] \tag{3.18}$$

$$B = \sum_{j}^{e}(\pm \mathrm{g}\rho_i \Delta z_i) \tag{3.19}$$

for the momentum, friction and buoyancy terms respectively, equation 3.16 can be manipulated, using the assumption for the time derivative, to calculate the volumetric flow rate for the next time step

$$G^{t+\Delta t} = \left\{\left[G\left(\sum_{j}^{e}\rho_i\right)\right]^t + \Delta t\frac{\pm M^t \mp F^t + B^t}{\sum_{j}^{e}\left(\frac{\Delta z_i}{A_{x,i}}\right)}\right\} / \left(\sum_{j}^{e}\rho_i\right)^{t+\Delta t} \qquad [\mathrm{m}^3/\mathrm{s}] \tag{3.20}$$

using the top sign then the bottom sign of the '$\pm M$'and '$\mp F$'for forward and reverse flow respectively.

3.2.4 Energy conservation

Using the conservation of energy as applied to a control volume, as shown in Figure 3.2 (c), gives

$$\frac{\Delta E}{\Delta t} = \sum \dot{E}_{in} - \sum \dot{E}_{out} \qquad [\mathrm{W}] \tag{3.21}$$

Expanding equation 3.21 into the individual energy components results in

$$\frac{\Delta(U+KE+PE)}{\Delta t} = \left[\dot{m}\left(u+\frac{v^2}{2}+zg+\frac{P}{\rho}\right)\right]_{in} - \left[\dot{m}\left(u+\frac{v^2}{2}+zg+\frac{P}{\rho}\right)\right]_{out} + \dot{Q}_{in} - \dot{Q}_{out} + \dot{W}_{in} - \dot{W}_{out} \quad [\text{W}] \quad (3.22)$$

As the control volume is not moving the potential and kinetic energies are negligible when compared to the changes in energy due to heat transfer, thus $KE \approx 0$, $PE \approx 0$, $\Delta(v^2/2) \approx 0$ and $\Delta(zg) \approx 0$. The $\dot{W}_{out}$ is the work required to keep a constant pressure in the system as caused by the expansion line and tank. Total work done on moving the fluid, at a constant pressure, out and into the loop through expansion line is

$$\dot{W} = \dot{W}_{in} - \dot{W}_{out} = -P\frac{\Delta V}{\Delta t} \quad (3.23)$$

and thus

$$\frac{\Delta(U+PV)}{\Delta t} = \left[\dot{m}\left(u+\frac{P}{\rho}\right)\right]_{in} - \left[\dot{m}\left(u+\frac{P}{\rho}\right)\right]_{out} + \dot{Q}_{in} - \dot{Q}_{out} \quad [\text{W}] \quad (3.24)$$

using the definition of static enthalpy $H = U + PV$ and $h = u + P/\rho$, equation 3.24 becomes

$$\Delta H/\Delta t = (\dot{m}h)_{in} - (\dot{m}h)_{out} + \dot{Q}_{in} - \dot{Q}_{out} \quad [\text{W}] \quad (3.25)$$

The specific enthalpy, $h_i = H_i/m_i$, may then be determined using the assumption for the time derivative as:

$$h_i^{t+\Delta t} = \frac{(mh)_i^t + \Delta t\left((\dot{m}h)_{in}^t - (\dot{m}h)_{out}^t + \dot{Q}_{in}^t - \dot{Q}_{out}^t\right)}{m_i^{t+\Delta t}} \quad [\text{J/kg}] \quad (3.26)$$

3.3 Primary Loop Theoretical Model

This section begins with the physical layout of the theoretical model for the primary loop. The section then discusses the pressure calculation. The heat transfer of the control volumes and the modelling of the expansion line and tank are also discussed. The expansion/contraction of the fluid and its resulting modelling implications can be found in section B.2, of Appendix B.

3.3.1 Physical layout

The physical hydrodynamic layout of the theoretical model is based on the experimental set-up dimensions as illustrated in Figure 3.3. The down-comer piping is made up of glass tubes, with an ID=34 mm (numbers 1 to 2), and stainless steel tubing, with an ID=31 mm (numbers 3-4-5), with the numbers corresponding to those in Figure 3.3. Similarly, the rubber tube of the expansion line, ID=25 mm (numbers 6-7), is also illustrated in Figure 3.3. The inner diameter of the expansion tank is 0.8 m.

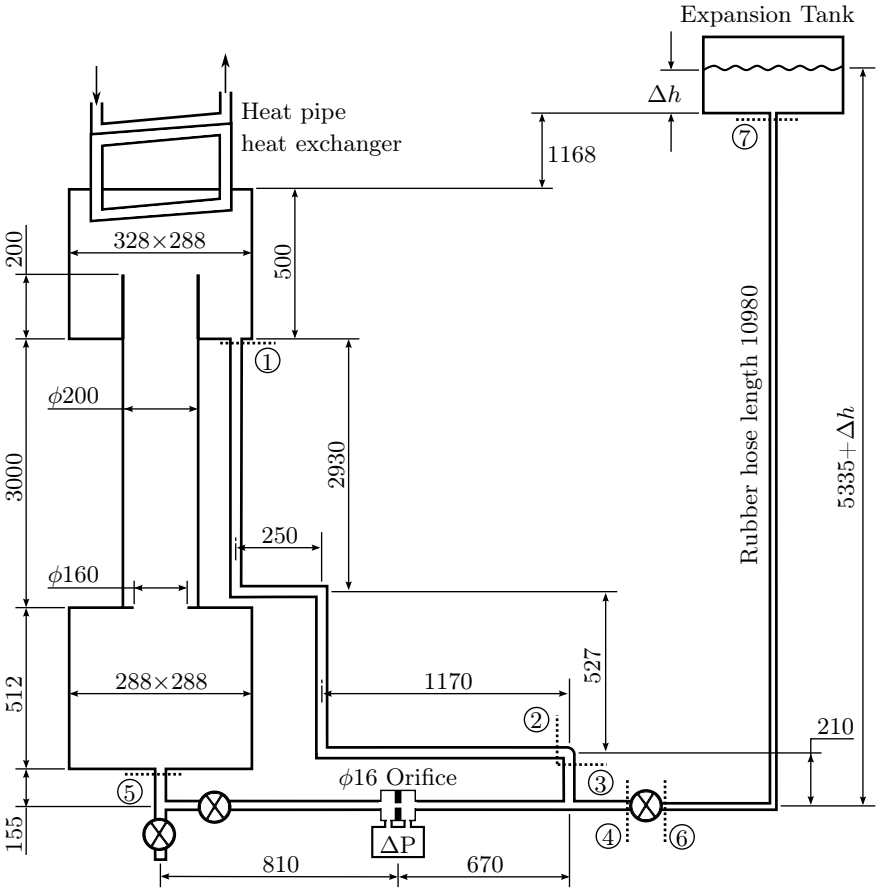

Figure 3.3: Hydraulic pipe work dimensions [mm] of experiment

The model was broken up into different zones to structure the computer simulation: Zone 1 is the reactor of the experiment; Zone 2 is the riser tube above the reactor (referred to as the riser); Zone 3 is the steam drum; Zone 4 the condensate return pipe (the down-comer) and Zone 5 the expansion tank/pressurizer and its connection pipe, referred to as the expansion line, as seen in Figure 3.4. The loop, zones 1 to 4, begins with the first cell in the reactor, j, and ends with the last cell in the down-comer, e, as shown in Figure 3.1 (b). Similarly, the expansion line begins with the first control volume, m, and ends in the expansion tank which is modelled as one control volume, n. The Zones are further broken up into sections, typically at interfaces or changes in orientation resulting in a change in the gravitational force direction. This allowed for the simpler allocation of properties, such as frictional minor losses, in the program. Furthermore, the number of control volumes in a section can be specified arbitrarily.

All the control volumes except for the expansion tank, n, are of the Eulerian type; they are constant in size and allow fluid to cross over the control volume boundaries. The expansion tank is a combination of both the Eulerian and

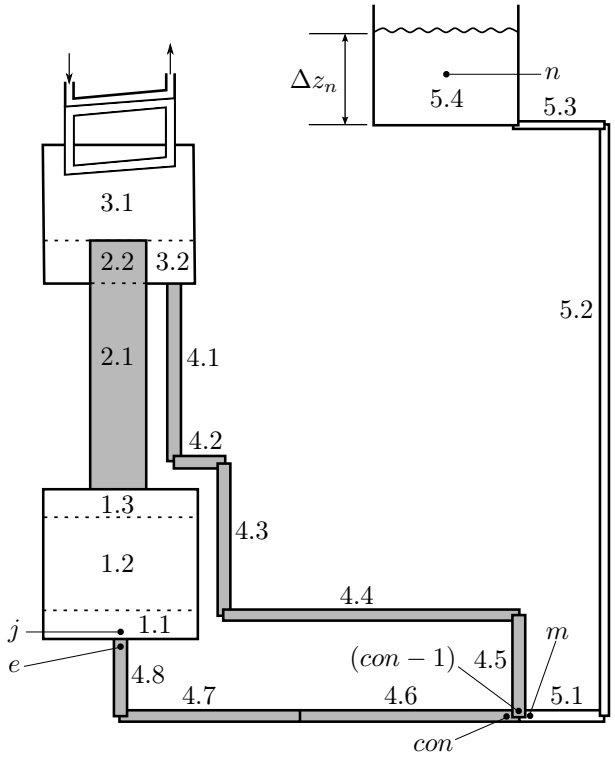

Figure 3.4: Different Zones *i,j* for theoretical model of experiment

Lagrangian view of control volumes. The expansion tank, n, is Eulerian at its connection to the expansion line, but it is Lagrangian at its top surface which is allowed to move up and down to allow for the expansion and contraction of the fluid in the entire system, the same as in the experimental set-up. The expansion tank is restricted to one control volume. The connection cell between the loop and the expansion line is the first control volume in Zone 4.5, *con*, as shown in Figure 3.4.

3.3.2 Pressure calculation

The working pressure of the primary loop's individual control volumes is calculated using the assumption that the pressure is constant at any height-level or elevation in the loop and expansion line. The only known pressure is the pressure at the surface of the expansion tank with the pressure being the atmospheric pressure and approximated at 101.325 kPa. The level of the expansion tank is re-calculated each time step resulting in a new working pressure of the primary loop for each time step. Thus, the pressure at any point in the loop is calculated by the summation of the hydrostatic pressures from the surface of the expansion tank, n, to the desired points corresponding to the elevation in the expansion line.

3.3.3 Flow frictional loss model

The frictional losses used to develop τ, as used in equation 3.20, follows the following procedure. $\tau = \frac{C_f \rho v^2}{2}$ for simple pipe wall friction losses with the loss coefficient C_f defined according the Reynolds number, Re, value:
if $Re \leq 1$ then (arbitrarily chosen)

$$C_f = 16$$

if $1 < Re \leq 1181$ then ($16/Re \approx 0.078 Re^{-0.25}$ when $Re = 1181$)

$$C_f = 16/Re$$

if $Re > 1181$ then a Blasius type friction factor is used

$$C_f = 0.078 Re^{-0.25}$$

(Çengel and Cimbala, 2006; Whalley, 1987). The so-called *minor losses* from bends, valves, expansions and contractions are incorporated by an addition of an equivalent length of pipe for the affected control volumes. The minor losses, K_L, values according to Batty and Folkman (1983) are shown in Table 3.1. The equivalent length and respective areas are defined as

$$L_{eq} = D_h K_L / (4 C_f)$$

$$A_{eq} = L_{eq} D_i \pi$$

with K_L being the minor loss co-efficient. This addition length L_{eq} is then added to length of the control volume for the calculation of the friction term in the momentum equation 3.20. For a control volume the addition to equation 3.20 is thus

$$\left[\tau \frac{A_z}{A_x}\right]_i = \tau \frac{\pi D_{h,i} (\Delta z_i + L_{eq,i})}{A_{x,i}} \tag{3.27}$$

where $\tau = |\left(C_{f,i} \rho_i \left(|G|/A_{x,i}\right)^2\right)/2)|$.

Table 3.1: Minor loss coefficients for pipe fittings Batty and Folkman (1983)

Description	K_L	**Description**	K_L
Pipe Contraction	0.5	Pipe Expansion ($A_1 < A_2$)	$(1 - A_1/A_2)^2$
Tank expansion	1	Tank Contraction	0.75
Elbow	0.45	Tee	1
Ball valve	0.05	(Çengel and Cimbala, 2006)	

3.3.4 Heat transfer in and out of a control volume

The heat transfer rate out of the control volume was modelled for heat loss to the environment as

$$\dot{Q}_{env,out} = (T_i - T_{amb})/R_{tot} \qquad [\text{W}] \tag{3.28}$$

where R_{tot} is the thermal resistance, as explained in Appendix A. Heat transfer by conduction between adjacent cells is

$$\dot{Q}_{i,con} = k_{ave,(i,i-1)} A_{x,min(i,i-1)} \frac{T_i - T_{i-1}}{(\Delta z_i + \Delta z_{i-1})/2} + k_{ave,(i,i+1)} A_{x,min(i,i+1)} \frac{T_i - T_{i+1}}{(\Delta z_i + \Delta z_{i+1})/2} \tag{3.29}$$

where $k_{ave,(i,i\pm1)}$ is the average thermal conductivity and $A_{x,min(i,i\pm1)}$ is the smaller of the two cross-sectional areas. Thus the heat transfer out of a typical control volume is

$$\dot{Q}_{out} = \dot{Q}_{env,out} + \dot{Q}_{con} \qquad [\text{W}] \tag{3.30}$$

The heat input from the reactor, $\dot{Q}_{ele,in}$, and the heat extracted by the secondary loop heat exchanger, $\dot{Q}_{HE}$, only affects the respective control volumes in the reactor, zone 1.2, and in the steam drum, zone 3.1. The amount of heat extracted in zone 3.1 of the steam drum is determined by the theoretical model for the secondary heat exchanger loop as described in Chapter 4.

3.3.5 Modelling of zone 5

The control volumes making up the expansion tank and connection line, which made up zone 5, are handled differently to the control volumes of the loop. Although zone 5 is also broken up into separate control volumes, the separate control volumes are only used to calculate the heat losses of zone 5, the height of the expansion tank, $\Delta z_n = \Delta h$, and in the pressure calculation for the primary loop. To simplify and speed-up the solution algorithm, zone 5 is modelled as one control volume in all other respects. This single control volume uses the total of all the heat losses from all the individual control volumes in zone 5 to model the heat loss.

As zone 5 is treated as a single control volume the momentum equation in the form of equation 3.20 is not applied to zone 5. Instead of the volumetric flow rate being calculated by equation 3.20, the flow rate in and out of zone 5 is defined by the expansion/contraction, equation B.2, of the fluid in the loop, with all fluid outflow from zone 5 leaving at zone 5's bulk temperature and all inflows from the loop affecting this bulk fluids properties.

The bulk fluid properties are found by applying the conservation of energy, equation 3.20, to zone 5 which is viewed as one control volume. The mass of the fluid in the expansion line, zones 5.1-5.3 in Figure 3.4, is calculated using the new density and V_i. The total mass in the loop, expansion line and

expansion tank must remain constant as no mass is leaving the system. Thus, the mass in the expansion tank is

$$m_n^{t+\Delta t} = m_{orig} - \sum_{i=j}^{e} m_i^{t+\Delta t} - \sum_{i=m}^{n-1} m_i^{t+\Delta t} \tag{3.31}$$

where m_{orig} is the original mass of the system's fluid at t=0 s. As mass cannot pass out of the top of the expansion tank, control volume n, due to its Lagrangian nature, the tank's height must increase. Thus, the new volume for the tank is

$$V_n^{t+\Delta t} = m_n^{t+\Delta t} / \rho_{zone5}^{t+\Delta t} \tag{3.32}$$

from which the new Δz_n can be calculated and used in the pressure calculation.

3.4 Primary Loop Solution Algorithm

The solution algorithm to solve the theoretical model for the primary loop was written in Fortran 90 using Microsoft Visual Studio 2010 Ultimate. The solution algorithm uses an explicit numerical method to solve the mass, energy and momentum conservation equations applied to the control volumes seen in Figure 3.2 for the loop and expansion line shown in Figure 3.1 (b) using the geometries given in Figure 3.4. Due to the large size and number of aspects of the theoretical model, the solution algorithm was broken up into a number of subroutines and is presented in a sequential fashion in this section with all major subroutines executed given in individual sections.

The main routine of the computer program is shown in Figure 3.5. During development rough algorithms were created on which the code was based however the algorithms presented in the text are derived from the raw and finally

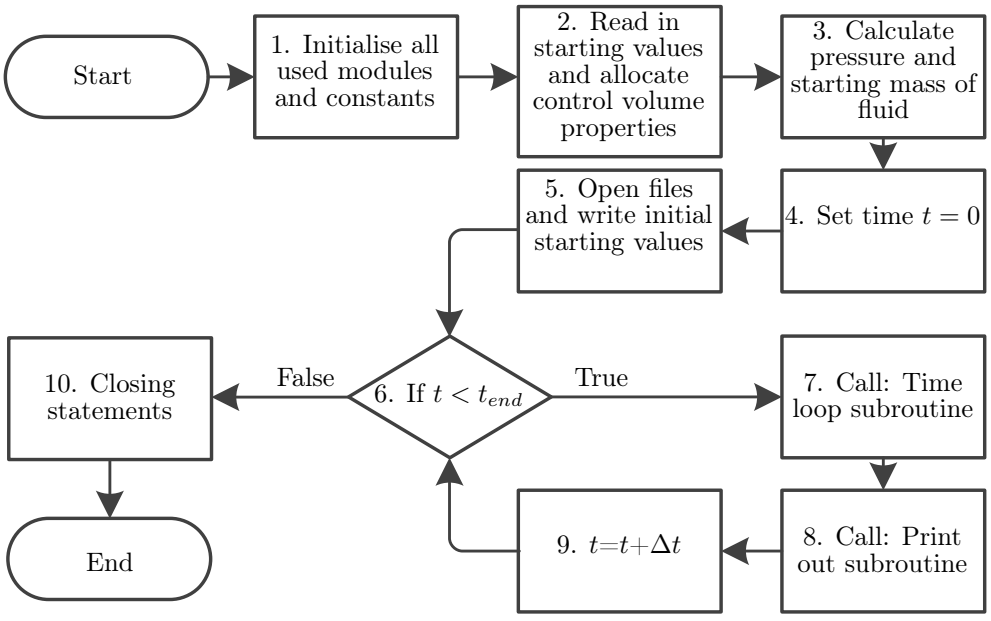

Figure 3.5: Primary loop main routine algorithm

implemented Fortran code. Thus, Figure 3.5 along with all other algorithms and routines presented in Appendix B are determined/created from raw Fortran code and not the other way around with the code written/implemented to reproduce the shown algorithm. This was done to show the true implementation of the code and used as means of verifying the code.

The main program consists of starting operations, steps 1 to 5 as seen in Figure 3.5, where all the properties of the primary loop are defined. The program then enters into a loop and predicts all the properties for the next time step by executing the *time loop* subroutine, step 7 in Figure 3.5. The contents of the *time loop* subroutine as well as time step selection criteria are discussed in Appendix B. During steps 8 and 9, the program writes results to file for a select number of time steps, by executing *print out* subroutine, before increasing the time step by an increment as seen in Figure 3.5. The program terminates when the time has reached the selected amount of time, after which the program writes to file and ends, step 10 in Figure 3.5.

4 Theoretical Modelling of Secondary Heat Exchanger Loop

The purpose of modelling the secondary heat exchanger was so that the model could be implemented in a simulation of the complete experimental set-up. The model's inputs would be the bulk temperature of the fluid surrounding the evaporator section, T_{eo}, the mass flow-rate of the cooling water, $\dot{m}_{cw}$, and the inlet temperature of the cooling water, $T_{cw,in}$. From the inputs the major outputs of the model would be the overall heat transferred, $\dot{Q}$, the internal temperature of the heat pipe, T_i, and the temperature of the exiting cooling water, $T_{cw,out}$.

To model the secondary heat exchanger a thermal resistance analogy was

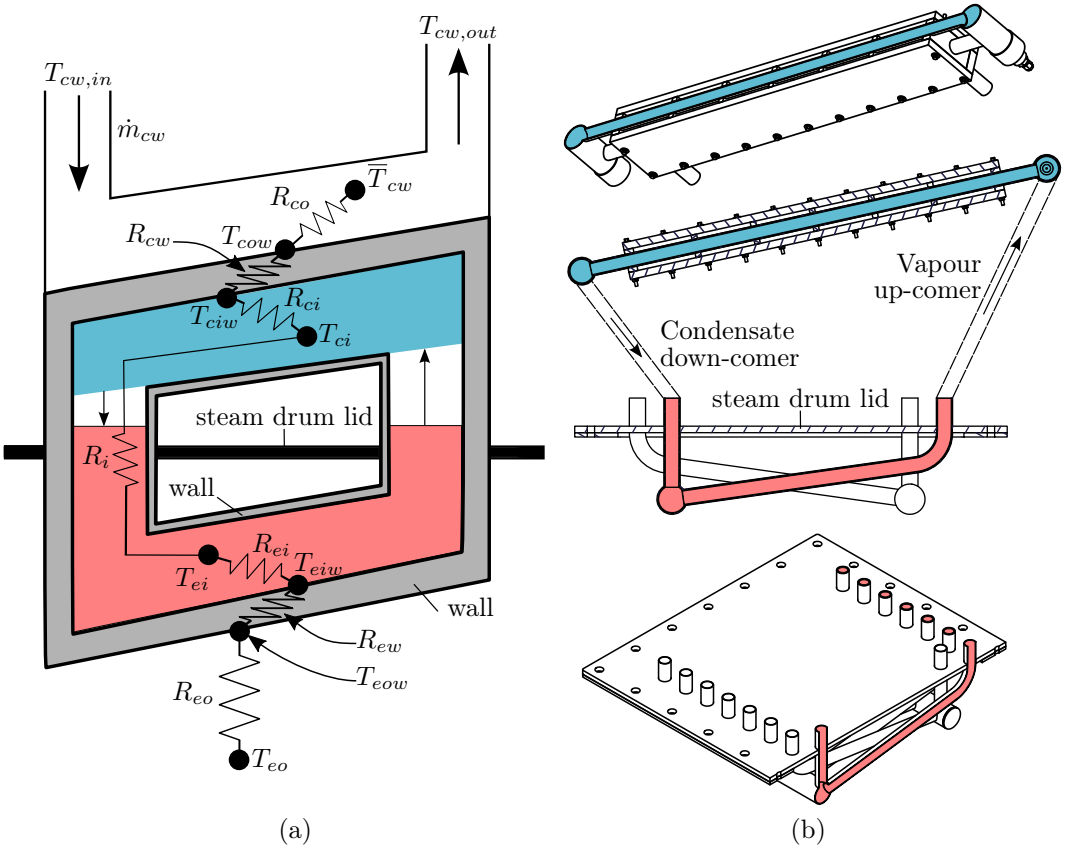

Figure 4.1: The secondary loop heat exchanger shown as, (a), a vertically sectioned diagram showing the evaporator section in pink and condenser in blue with overlaid thermal resistance diagram and, (b), isometric view of the vertically sectioned condenser (top) and evaporator (bottom), and side view of vertically sectioned complete secondary loop (middle).

used. The resulting thermal resistance diagram can be seen in Figure 4.2 and repositioned and placed on a schematic of the secondary loop heat pipe in Figure 4.1. Figure 4.1 also shows the internal surfaces of the evaporator and condenser sections for the model and relates them to cutaways from the CAD model using colours pink and blue for the evaporator and condenser respectively. There are a number of reasons for modelling with the thermal resistance analogy rather than trying to model the physical flow inside the secondary heat exchanger. Firstly, the flow phenomena in natural circulating thermosyphon type heat pipes is not well established or understood and is case specific. Secondly, the computational intensity for performing a computational fluid dynamics simulation on the heat exchanger would be too great. Thirdly, the unique geometry of the heat pipe under investigation adds modelling complications, for instance the evaporator and condenser sections are multi-tubed.

Furthermore, the number of transfer units (NTU) approach, that typically can be used to find $\dot{Q}$ and $T_{cw,out}$ with ease, could not be used to fully describe the secondary loop heat exchanger. This is because the secondary loop effectively consists of two heat exchangers with the evaporating section having phase change procedures on both the inside and outside when transferring heat under normal operating conditions. With a double sided phase change procedure the effectiveness-NTU approach was not applicable. However, for the condensing side of the secondary loop the effectiveness-NTU approach, as set out by Çengel *et al.* (2011), can be used, but the internal temperature, T_i, must first be defined.

To solve for T_i, the thermal resistance model would need to be solved through an iterative process. As an iterative process would be required it was decided to solve the resistance model in its entirety. The resistance model would additionally allow for a sensitivity analysis to be performed on the selected variables allowing their direct influence on the individual resistances as well as the entire model to be seen. The effectiveness-NTU model would

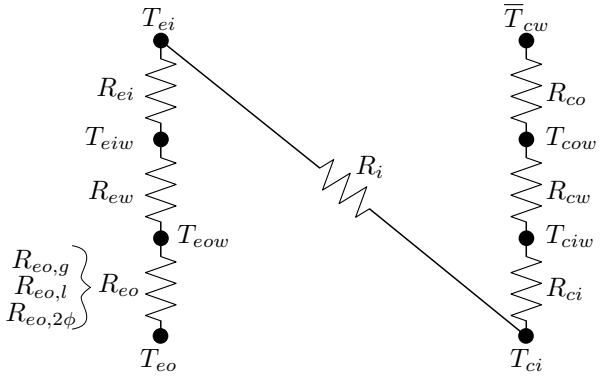

Figure 4.2: Simple thermal resistance diagram of the secondary loop heat exchanger

be used to speed up the iterative process by providing good estimated initial values, for the condenser section, for a defined T_i.

The thermal resistance model contains seven thermal resistances as seen in Figure 4.2. The first major assumption is that the internal thermal resistance between the evaporator and the condenser section is negligible, $R_i \approx 0$ thus

$$T_i = T_{ei} = T_{ci} \tag{4.1}$$

leaving six resistances to be defined. This effectively models the heat pipe as a reservoir governed by the saturation temperature and pressure of the working fluid. These six thermal resistances are divided into two groups and summed giving the resistances

$$R_e = R_{eo} + R_{ew} + R_{ei} \tag{4.2}$$

$$R_c = R_{co} + R_{cw} + R_{ci} \tag{4.3}$$

for the evaporator and condenser sections respectively, seen on the left and right sides of R_i in Figure 4.2. The heat transfer through the evaporator section is

$$\dot{Q}_e = \frac{T_{eo} - T_i}{R_e} \tag{4.4}$$

and for the condenser section is

$$\dot{Q}_c = \frac{T_{ci} - \overline{T}_{cw}}{R_c} \tag{4.5}$$

where $\overline{T}_{cw}$ is a representative value of the average cooling water temperature. Additionally the overall heat transfer coefficient, which is the inverse of the thermal resistance, is defined as

$$(UA) = \frac{1}{R} = \frac{\dot{Q}}{T_{hot} - T_{cold}} \tag{4.6}$$

where T_{hot} and T_{cold} are the temperatures of the heat source and sink respectively. The thermal resistance of the wall for both the condenser and evaporator is approximated as steady heat conduction through a wall as

$$R_w = \frac{\delta_w}{kA} \tag{4.7}$$

where the wall thickness is δ_w, k is the thermal conductivity and surface area is A. The remaining individual resistances are found using a combination of theory and experimental correlation explained in the following sections.

4.1 Evaporator Thermal Resistances

The thermal resistances for the evaporator section, as illustrated in Figure 4.1, are as follows: R_{eo}, the resistance from the bulk fluid surrounding the evaporator to evaporator outside wall; R_{ew}, the resistance of the wall; and R_{ei}, the resistance from the evaporator's inside wall to the heat pipes inside. R_{ew} is found using equation 4.7.

4.1.1 External thermal resistance

The external thermal resistance of the evaporator was modelled for the three different states of fluid the evaporator section could be submerged in. These regimes are when the steam drum is filled with either water (liquid regime), gas (condensing regime) or a combination of both water and gas (two-phase regime). A liquid ($R_{eo,l}$), condensing ($R_{eo,g}$) and two-phase ($R_{eo,2\phi}$) thermal resistance is used for the water, gas and liquid/gas regimes respectively.

For the condensing regime $R_{eo,g}$ is found by first determining the average heat transfer coefficient for film condensation on the outer surfaces of the horizontal tubes as given by Çengel *et al.* (2011) being

$$h_{eo,g} = 0.729 \left[\frac{\mathrm{g}\rho_l(\rho_l - \rho_g)h^*_{fg}k_l^3}{\mu_l(T_{sat} - T_s)D_c} \right]^{1/4} \tag{4.8}$$

where $h^*_{fg} = h_{fg} + 0.68c_{pl}(T_{eo} - T_{eow})$ is the modified latent heat of vaporization and the film temperature is approximated as $T_{eo_{film}} = (T_{eo} + T_{eow})/2$. Using this average heat transfer coefficient the thermal resistance is

$$R_{eo,g} = \frac{1}{h_{eo,g}A_e} \tag{4.9}$$

The unique shape of the heat exchanger made it difficult to find an applicable case, within established theory, to model the heat transfer coefficient for the liquid regime. It was decided to use simple natural convection theory to find the *Nusselt number* using the Rayleigh number in combination with experimentally correlated factors. Simple empirical correlations for the *Nusselt number* are typically of the form

$$Nu_{eo} = CRa_D^n \tag{4.10}$$

for natural convection, with the Rayleigh number defined as

$$Ra_D = \frac{\mathrm{g}\beta(T_{eo} - T_{eow})D^3}{(\mu/\rho)^2}Pr \tag{4.11}$$

(Çengel *et al.*, 2011) giving the heat transfer co-efficient as

$$h_{eo,l} = \frac{Nu_{eo}k_l}{D} \tag{4.12}$$

with all properties evaluated at the film temperature $T_{eo_{film}}$. As the secondary heat exchanger is intended to operate for the majority of the time in the condensation regime, it implied that, errors associated with this approximated heat transfer for the liquid regime would typically only affect the start up and possibly some system transient predictions (when the steam space collapsed in the steam drum). Finally the thermal resistance for the liquid regime becomes

$$R_{eo,l} = \frac{1}{h_{eo,l}A_e} \tag{4.13}$$

It was decided that the two-phase operation regime would just use a percentage combination of the liquid and condensation resistances such that

$$R_{eo,2\phi} = F_{2\phi}R_{eo,l} + (1 - F_{2\phi})R_{eo,g} \tag{4.14}$$

where $F_{2\phi}$ is appropriately selected between zero and one to approximate the experimental results.

4.1.2 Internal boiling thermal resistance

The internal thermal resistance of the evaporator was found assuming that the boiling was taking place in the nucleated boiling regime. This is a reasonable assumption as the charge of working fluid in the secondary loop would be sufficient to ensure the heat pipe's evaporator section would not dry out. Furthermore, the heat source at its peak heat flux would be when the evaporator was in the condensing regime and thus the temperature of the surface could not increase uncontrollably as in the case of electrically heated devices. Thus, the peak heat flux is expected to be lower than the critical heat flux. As no burn out can occur the liquid and vapour would always remain in the vapour dome. The Rohsenow correlation for nucleated boiling is typically given in the form

$$\left[\frac{c_{pl}(T_s - T_{sat})}{h_{fg}}\right] = C_{sf}\left[\frac{\dot{q}''_{ei}}{\mu_l h_{fg}}\left(\frac{\sigma}{g(\rho_l - \rho_g)}\right)^{1/2}\right]^{1/m} Pr_l^n \tag{4.15}$$

as in the works of Pioro (1998) and Kew and Reay (2006) where m=3 for most fluids. This correlation can be manipulated to give the nucleated boiling heat flux

$$\dot{q}''_{ei} = \mu_l h_{fg}\left[\frac{g(\rho_l - \rho_g)}{\sigma}\right]^{1/2}\left[\frac{c_{pl}(T_s - T_{sat})}{C_{sf}h_{fg}Pr_l^n}\right]^3 \quad [\mathrm{W/m^2}] \tag{4.16}$$

as done by Çengel *et al.* (2011). Typically C_{sf} and n varies corresponding to the surface fluid combination in Çengel *et al.* (2011) and Kew and Reay (2006). This is further confirmed in the works of Pioro (1998) where correlations for C_{sf} and n were found while $m = 3$ for multiple fluid surface combinations. The same approach is used by manipulating equation 4.15 using the natural logarithm into a form of

$$Y_1 = C_1 + C_2(X_1) \tag{4.17}$$

where C_1 and C_2 can be found using linear regression. The manipulating of equation 4.15 into the form of equation 4.17 results in

$$Y_1 = ln\left[\frac{c_{pl}(T_s - T_{sat})}{h_{fg}}\left(\frac{\mu_l h_{fg}}{\dot{q}''_{ei}}\left(\frac{g(\rho_l - \rho_g)}{\sigma}\right)^{1/2}\right)^{1/3}\right] \tag{4.18}$$

where $C_1 = ln(C_{sf})$, $C_2 = n$ and $X_1 = ln(Pr_l)$. This form allows Y_1 and X_1 to be calculated using experimental results then using linear regression C_1 and

C_2 can be found. Using the experimentally determined constants the overall heat transfer coefficient becomes

$$h_{ei} = \frac{\dot{q}''_{ei}}{T_{eiw} - T_{ei}} \tag{4.19}$$

and thus the internal resistance of the evaporator is

$$R_{ei} = \frac{1}{h_{ei} A_e} \tag{4.20}$$

4.2 Condenser Thermal Resistances

Similar to the evaporator, the thermal resistances for the condenser section of the secondary heat pipe loop are: R_{ci}, the resistance from the internal temperature of the condenser to the inside of the wall; R_{cw}, the resistance of wall; and R_{co}, the resistance from condenser's outside wall to the cooling water as shown in Figure 4.1. The condenser section's wall resistance, R_{cw}, is found using equation 4.7.

Using the effectiveness-NTU approach, as laid out by Çengel *et al.* (2011), the heat transfer of the condenser section could be estimated by first finding the overall heat transfer coefficient

$$(UA)_c = \frac{\dot{Q}}{T_i - \overline{T}_{cw}} \tag{4.21}$$

from experimental results. An appropriate function can be found to predict $(UA)_c$. The number of thermal units is found through

$$NTU = \frac{(UA)_c}{(\dot{m}c_p)_{cw}} \tag{4.22}$$

and then allows the effectiveness of the heat exchanger and its maximum heat transfer capability to be found through

$$\varepsilon = 1 - e^{-NTU} \tag{4.23}$$

$$\dot{Q}_{max} = (\dot{m}c_p)_{cw}(T_i - T_{cw,in}) \tag{4.24}$$

This, in turn, allows the heat transfer and the cooling water outlet temperature to be estimated using

$$\dot{Q}_{est} = \varepsilon \dot{Q}_{max} \tag{4.25}$$

$$T_{cw,out,est} = T_{cw,in} + \frac{\dot{Q}_{est}}{(\dot{m}c_p)_{cw}} \tag{4.26}$$

The estimated values can be used as initial values for an iterative solution of the condenser resistance model.

4.2.1 Internal thermal resistance

The internal heat transfer for condensation was found using

$$h_{ci} = 0.555 \left[\frac{g\rho_l(\rho_l - \rho_g)k_l^3}{\mu_l(T_{sat} - T_s)D} \left(h_{fg} + \frac{3}{8} c_{pl}(T_{sat} - T_s) \right) \right]^{1/4} \tag{4.27}$$

which is for film condensation on the inside of a tube as given by Çengel *et al.* (2011). The novelty of this equation is it requires no knowledge of the actual flow conditions inside the tubes but rather just the thermo-physical properties of the fluid. The internal thermal resistance for the condensation section thus becoming

$$R_{ci} = \frac{1}{h_{ci} A_c} \tag{4.28}$$

4.2.2 External thermal resistance

The external heat transfer from the condensing tubes to the cooling water can be defined as a multi-pass cross flow heat exchanger with forced flow across a cylinder bank with a constant surface temperature. The average Nusselt number for forced convection over a cylinder can be expressed compactly as

$$Nu_{cyl} = \frac{hD}{k} = CRe^m Pr^n \tag{4.29}$$

where $n = 1/3$ and constants C and m are given by empirical correlations (Çengel *et al.*, 2011). The fluid properties are calculated at the film temperature. This formulation is typically only valid for flow over a single cylinder, however Zukauskas, as cited in Çengel *et al.* (2011), has proposed a solution of the general form

$$Nu_{cyl} = \frac{hD}{k} = CRe^m Pr^n (Pr/Pr_s)^{0.25} \tag{4.30}$$

for cross flow over tube banks where all properties are evaluated at the arithmetic mean temperature. The external resistance in the condenser of the secondary loop was unique, in that it was neither a multiple tube bank or a single tube as used in theory. Thus to characterise the Nusselt number for this unique application it was decided to use the results of the experiment, using the definitions $V = \dot{m}/(\rho_l A_{ch})$ and $Re = (\rho_l V D_h)/\mu_l$ where A_{ch} is the cross-sectional flow area and D_h the hydraulic diameter of the channel (both at its smallest), and the form

$$Nu_{cyl} = \frac{hD}{k} = CRe^m Pr^n (Pr/Pr_s)^k \tag{4.31}$$

where C, m, n and k are all found through linear regression of the logarithmic form of equation 4.31. The Nusselt number is then used to find the heat transfer co-efficient and thus thermal resistance R_{co} using

$$h_{co} = \frac{Nu_{co} k_l}{D_h} \tag{4.32}$$

and

$$R_{co} = \frac{1}{h_{co} A_c} \tag{4.33}$$

4.3 Secondary Loop Solution Algorithm

To solve the secondary loop thermal resistance model an iterative process is required. The basic logic behind the algorithm is that the internal temperature of the heat pipe is needed to find the resistances of the condenser and evaporator. The secondary loop can be viewed as two heat exchangers connected by the same internal temperature T_i. The algorithm iterates for the internal temperature by changing the temperature value in accordance with the energy balance sign. The energy balance is found by calculating the energy entering through the evaporator section, $\dot{Q}_e = (T_{eo} - T_i)/R_e$, and energy extracted by the condenser section, $\dot{Q}_c = (T_i - \overline{T}_{cw})/R_c$, and subtracting the two. T_i is adjusted incrementally such that if $\dot{Q}_e > \dot{Q}_c$ then T_i is increased meaning a reduction in $\dot{Q}_e$ and an increase in $\dot{Q}_c$. This is done to ensure a net energy balance of $\dot{Q}_{in} = \dot{Q}_{out}$, assuming negligible losses. Once a balance of energy is found the algorithm is considered complete and the results are outputted. A basic description of the model's flow is shown in Figure 4.3.

Steps 5 & 6 and 7 & 8, in Figure 4.3, are also iterative steps in themselves as the wall temperatures within the separate resistance models for the condenser and evaporator sections must be found iteratively. This iteration is required as the wall temperatures have an influence on the thermal resistances. Iteration to the point where the resistances no longer change, gives the actual resistance, rather than a resistance based on an approximated temperature value.

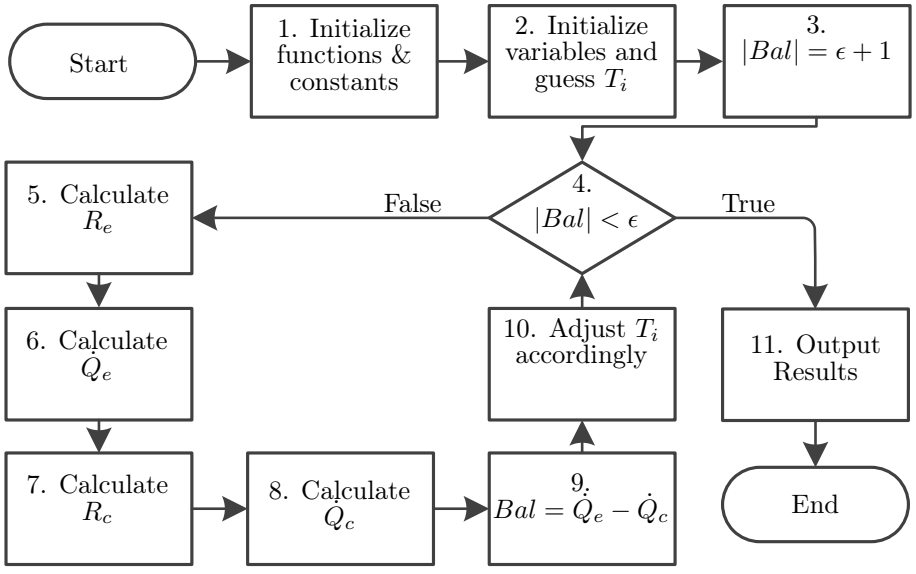

Figure 4.3: Basic algorithm to solve the secondary loops thermal resistance model

5 Experimental Set-Up

An experimental set-up of the primary and secondary loops was designed, built and tested to check the validity of the theoretical models created for both objectives 3 and 5. In this section the experiment's design, layout, construction and equipment will be discussed. The specifics of the instrumentation and data acquisition system can be found in Appendix C. The operation and safety of the experiment is discussed in Appendix E.

5.1 Geometry and Layout

The experimental set-up consisted of both the primary and secondary loops. The experimental set-up was designed with the aid of Autodesk Inventor Professional 2012, and a resulting CAD model of the side and front views of the primary and secondary loops is shown in Figure 5.1 (b) and (c). Figure 5.1 highlights the major components of the experimental set-up namely; 1) the reactor; 2) the riser; 3) the steam drum (liquid-steam separator); 4) the secondary loop; 5) the down-comer; 6) the orifice plate; 7) the expansion line connection; 8) the expansion tank; 9) the constant head tank.

The primary loop, with the evaporator section of the secondary loop, was constructed and tested first. A cut away view of the steam drum can be seen in Figure 5.4 showing the evaporator section of the secondary loop. The evaporator section of the secondary loop acted as a heat exchanger for the primary loop using water as the cooling medium in initial tests (test batches one and two). After the initial construction and testing was successful the condenser section with the connecting manifolds and pipe work of the secondary loop was constructed and attached to the primary loop with the evaporator. After attachment the entire system of the primary loop and secondary loop was tested (producing test batch three).

5.1.1 Primary loop layout

The major geometric considerations of the primary loop were primarily driven by the height of the laboratory. The laboratory roof was 8 m high, as illustrated in Figure 5.1 (a). The total height of the supporting frame from the base to the top was 5 m. Another determining factor in the height was to have a constant head tank in the lab to allow for easier control of the supply of cooling water to the heat exchanger. With the cooling water to the heat exchanger being gravity fed from a constant head tank, space had to be left between the heat exchanger and the roof so that the constant head tank was above the heat exchanger. The 3 m space left between the experiment and the roof of the laboratory also allowed for the expansion tank to be located inside the laboratory.

The overall hydraulic pipe work dimensions of the experiment are shown in Figure 3.3. The riser section of the experiment was limited to 3.2 m as that was the length of the ϕ200 mm stainless steel pipe already available. The top

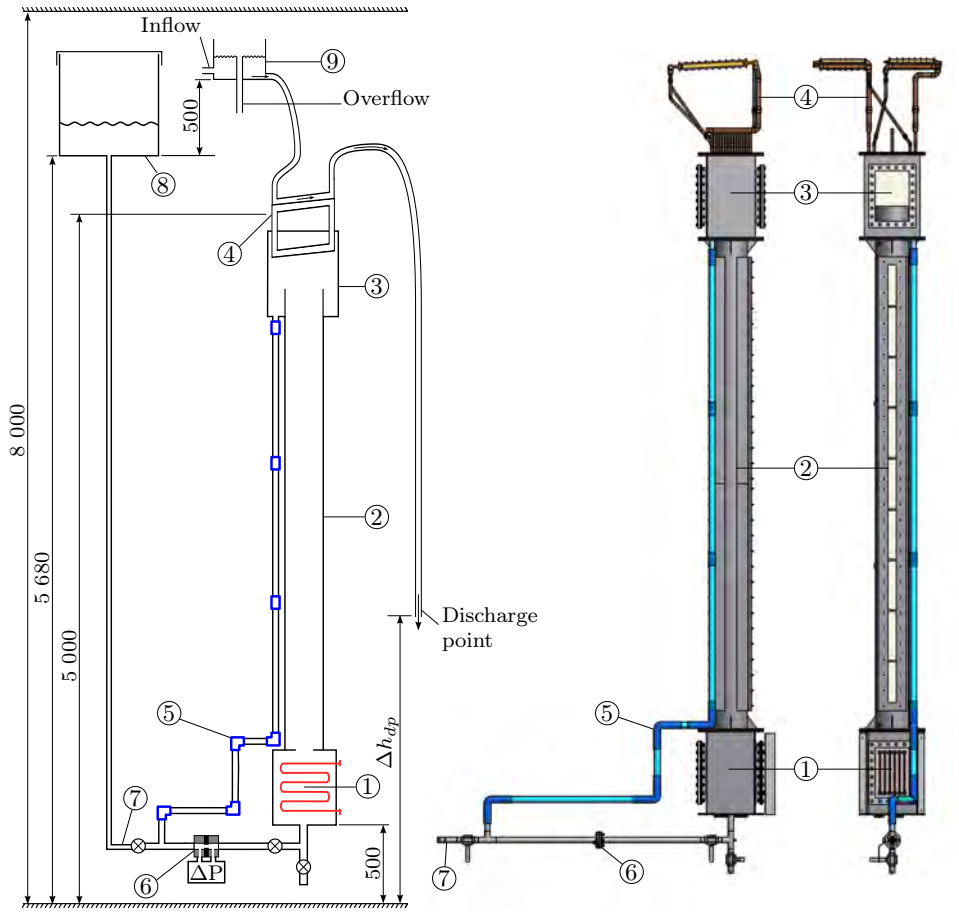

Figure 5.1: (a) A schematic showing dimensions [mm], (b) side and (c) front view of the experimental set-up showing the: 1) reactor; 2) riser; 3) steam drum; 4) secondary loop; 5) down-comer; 6) orifice plate; 7) expansion line connection; 8) expansion tank; 9) constant head tank with flow path of cooling water from inflow into the constant heat tank until discharge point Δh_{dp} from the floor.

of the riser protruded into the steam drum by 200 mm as seen in Figure 3.3, 5.1 and 5.4. The protrusion was designed to prevent the condensate from the evaporator running back into the riser section.

The plate at the top of the riser formed the bottom of the steam drum section and had a hole with hose connector to which the down-comer was connected. The plate at the bottom of the riser formed the lid of the reactor and had a smaller diameter opening than the riser section. The opening diameter was smaller so that plates with different sized orifices could be connected and used to restrict the flow out of the reactor section. The idea was to induce a pressure increase in the reactor by restricting the flow that would in turn ensure that boiling/flashing would happen in the riser only, as in the work of Yadigaroglu and Zeller (1994).

The experiment was designed so that visual observations of the flow phenomena within the experiment could be made. The experiment had windows in the reactor, steam drum and running the length of the riser section. Furthermore, to aid with the visibility and ensure no vapour was entrained in the down-comer during operation, the down-comer was made from lengths of glass tube, ID 28 mm, and joined by silicon rubber tubes.

The primary loop had three 1 inch BSP ball valves. One valve was placed between the primary loop and expansion line. This valve assisted in the filling of the primary loop but also allowed the experiment to be run in heat pipe mode by isolating the primary loop from the expansion line and tank. The other valve was at the lowest point of the experimental set-up below the reactor and was used to drain the experiment as well as perform leak tests on the system. A valve was placed between the inlet of the reactor and the orifice. The purpose of this valve was to allow for the measurement of the void fraction in the riser section.

The primary loop had an air and a pressure relief valve connected to a protruding copper tube from the copper base plate of the secondary loop, as seen in Figure 5.3. The protruding copper tube was the highest point in the primary loop through which any non-condensible gases that collected in the primary loop could be removed. A pressure relief valve was connected to the copper tube before the air relief valve and set to open at 2 $\text{Bar}_{(\text{abs})}$ which equates to a saturated vapour temperature of 121 ℃.

Thermal expansions and contractions of the experimental set-up were considered when designing the frame to hold the entire set-up. The frame was made out of angle iron sections welded to laser cut profiles. The frame consisted of two identically long sections that where placed on top of one another and bolted together. The frame had a maximum width and breadth of 412 mm and the experiment was sized to a maximum of 400 mm×400 mm to allow sufficient space for expansion in the horizontal directions. For expansion in the vertical direction it was decided to only support the experiment from the reactor section's base plate. This allowed the riser, steam drum and secondary loop to be lifted up within the frame due to thermal expansion without inducing any stress on the components.

The base plate of the reactor was raised 0.5 m off the ground to allow space for the draining valves and orifice plate set-up as well as to be a more comfortable height to work at. The reactor's inlet was situated in the middle of its base plate and had a ID=31 mm.

5.1.2 Secondary loop layout

The secondary loop consisted of two separate natural circulating, gravity driven, two-phase, thermosyphon type heat pipes. As gravity is what drives the working fluid, the heat pipes were designed so that condensate would find its way to the evaporator. Figures 5.2 (b) and (c) show the angles α and β for the evaporator and condenser slopes respectively. The final design had angles,

$\alpha = 8°$ and $\beta = 3°$, however, they were in different planes as shown by the front and side views of one loop in Figure 5.2 (b) and (c). The evaporator of the secondary loop was designed first to be used as a water cooled condenser for the primary loop in initial tests. Only after the primary loop performed satisfactorily and safely, was it decided to continue and build the remaining components of the secondary loop. The secondary loops were each charged with 320 ml of methanol. This amount of methanol charge was used to ensure that the evaporator would be filled to the point where the ϕ15 mm evaporator tubes of each loop crossed one another.

5.1.2.1 Evaporator

The evaporator was sized to be able to remove 9 kW from the primary loop, with the evaporator outside in liquid water and cooling water flowing inside the evaporator. This sizing would allow for a large enough evaporator section

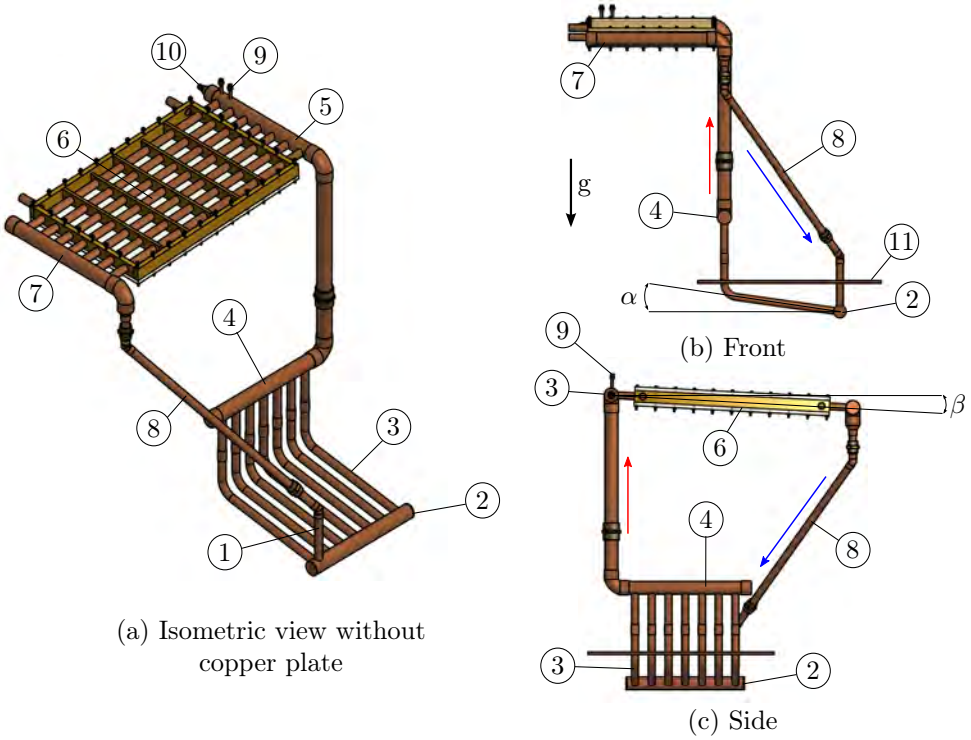

(a) Isometric view without copper plate

(b) Front

(c) Side

Figure 5.2: Heat pipe 1 of the secondary loop shown in (a) without steam drum lid, (b) from the front showing the angle α of evaporator pipes and (c) from the side showing the angle of the condenser β, (a) and (b) also showing the upwards flow of vapour and downwards flow of condensate. The ballooned sections are: 1) condensate return tube; 2) manifold within steam drum; 3) 15 mm pipe evaporator pipe; 4) vapour collection manifold; 5) vapour distribution manifold; 6) multi-pass condenser; 7) condensate collection manifold; 8) condensate return down-comer; 9) Schrader valves; 10) thermocouple probe compression fitting; 11) steam drum lid.

for the heat pipe secondary loop. Sizing in this manner would in turn allow for additional safety because the heat exchanger would be able to remove all power added to the loop by the heating elements no matter the phase of the water the evaporator was submerged in.

Using general heat transfer theory from Çengel *et al.* (2011), the evaporator was sized through an iterative process. It was decided the design would have to be flexible in allowing only portions of the condenser to be used so that the amount of heat to be removed could be controlled. This enabled an operator to control the difference in temperatures of the cooling water, in and out, ensuring it was not too large while remaining accurately measurable. Flexibility was also needed due to the inherent over-design of the evaporator through using a higher liquid to liquid thermal resistance instead of the lower condensation to liquid thermal resistances. The desired flexibility was achieved by building two equivalently sized evaporators.

Due to the limited space and taking into account ease of fabrication, it was decided that the tubes would be fed condensate/cooling water by a single pipe connected to a manifold in the steam drum, points 1 and 2 in Figure 5.2 respectively. Seven tubes would be connected to this manifold and then make their way through the copper plate which formed the lid of the steam drum as seen in Figure 5.2.

The evaporator and condenser were designed so that they were a mirror of one another, see figures 5.3 and 5.5. The space between the tubes coming from the manifold were sized to allow the tubes from the opposing evaporator to pass through with 3 mm of clearance either side. The angles, α in Figure 5.2, of the tubes allowed for the opposing evaporator's manifold to sit below the other evaporators tubes. This allowed the two opposing evaporators to interlock without physically touching. This criss-cross interlocking resulted in the pipe layout seen in Figure 5.3. The interlocking allowed for a tightly packed bundle of pipes to act as an evaporator, which had sufficient area but also fitted into the steam drum. An additional benefit of constructing this criss-cross interlocking evaporators is that when the evaporators condensed the steam in the steam drum the condensate it formed would run down the angled pipes, due to angle α, see Figure 5.4 (b), and collect on the bottom of the manifold. The design ensured that from the base of the manifold the condensate would then form drops and fall into the liquid portion of the steam drum and not drop back down into the riser as illustrated in Figure 5.4 (b).

Furthermore, for the initial tests one of the evaporators was fitted with valves on the ϕ15 mm tube protrusions on the outside of the copper plate. The valves were situated before the exterior manifold and can be seen in Figure 5.3. The valves allowed the operator to control the flow of water through the individual pipes. The valves allowed for flexibility as seven of the fourteen tubes could be controlled independently with the other seven either open or closed as a group. The design of the evaporator also allowed the cooling water to be distributed from the bottom most point. This was done to ensure that

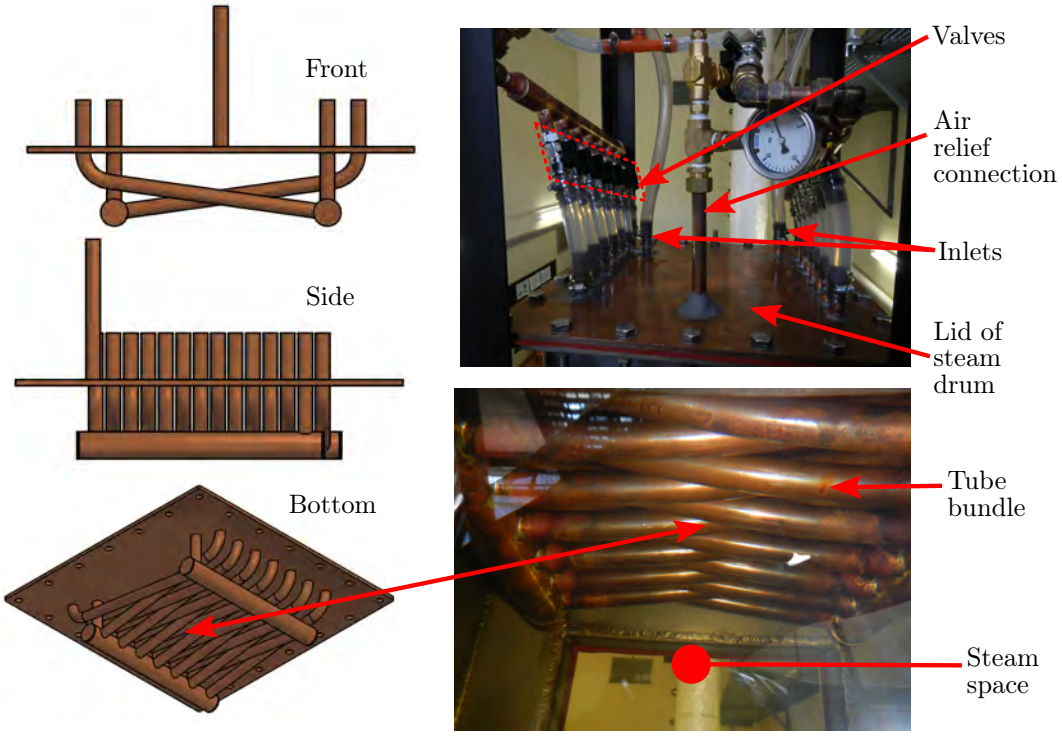

Figure 5.3: Condenser set-up of primary loop for initial tests showing 3 CAD views, front, side and bottom, as well as picture taken of lid (top), showing pipe and valve assembly, and picture from bottom looking up into the steam drum showing evaporator pipe bundle.

unwanted non-condensible gases would find their way out of the evaporator and not get trapped. When the evaporator was converted to a heat pipe the shape also helped with the performance, as the condensate would flow into the lowermost point of the evaporator.

5.1.2.2 Condenser

Two identical condensers were constructed for the two evaporators of the secondary loop. The major design constraints for the condenser were that the condenser had to: 1) have an inclined angle β as seen in Figure 5.2 (c); 2) fit on top of the frame of the primary loop set-up; 3) ensure that thermal expansion did not put stress on the components; 4) seal for both pressure and vacuum and 5) the flow of the cooling water had to be visible.

The condenser was constructed from seven ϕ15 mm copper tubes soldered at either end to manifolds, numbers 5 and 7 in Figure 5.2. Between the manifolds a 25×10 mm brass plate formed the outer perimeter of the multi pass heat exchanger, item 6 in Figure 5.2. A top view of this multi pass heat exchanger is shown in Figure 5.4 (a). The 25×6 mm brass baffle plates formed six passes for the cooling water to follow. The first and last passes were 65 mm wide while the rest were 60 mm wide. A 7.5 mm gap was left for the cooling

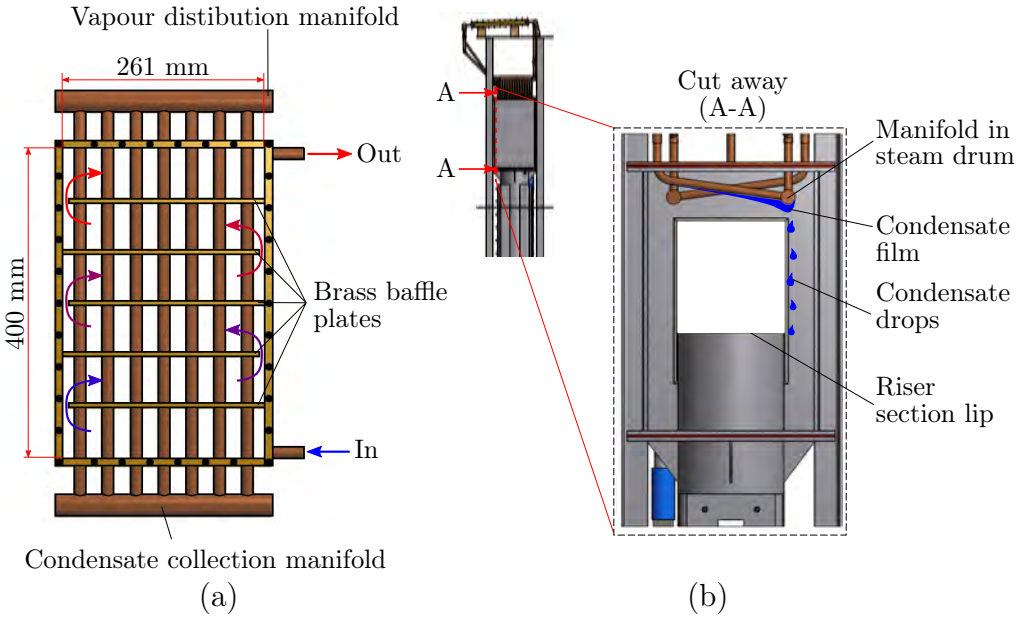

Figure 5.4: (a) Condenser of secondary loop showing internal dimensions of counterflow heat exchanger and water flow path, (b) cut away section of steam drum with riser lip extrusion into steam drum, both evaporators and showing condensate film and drop path from one manifold.

water to pass each baffle plate at alternating ends. The resulting flow direction is shown in Figure 5.4 (a). The baffle and perimeter plates were silver soldered to one another while the ϕ15 mm tubes were only soldered to the perimeter brass plates. The fit, where ϕ15 mm tubes passed through the baffle plates, was tight enough that no soldering was required. The resulting condenser had a length of $\pm\,400$ mm of copper pipe being cooled, as seen in Figure 5.4 (a).

A gasket was cut for each side to seal between the brass and a piece of clear Perspex. This Perspex became the top and bottom of the condenser. The Perspex was pressed against the brass frame by 3 mm bolts passing right through the brass outer frame. Perspex was used so that the operator could see how the cooling water was flowing through the channels.

The condensers were held in place by the connected piping and rested on a block of wood with one surface cut at angle β. After the satisfactory initial primary loop tests the evaporator (steam drum lid) was retrofitted with two 28 mm vapour collection manifolds, item 4 in Figure 5.2, and angled pipes so that the condensate return pipe could be fitted with an extension and joined to the condensate collection manifold, items 1, 8 and 7 in Figure 5.2 respectively. The angled pipes had unique angles and lengths for each evaporator of the two heat pipes.

The vapour distribution manifold, item 5, of each condenser had a thermocouple probe compression-fitting-type connector on the one side, item 10, in Figure 5.2. On the other side of the vapour distribution manifold the nec-

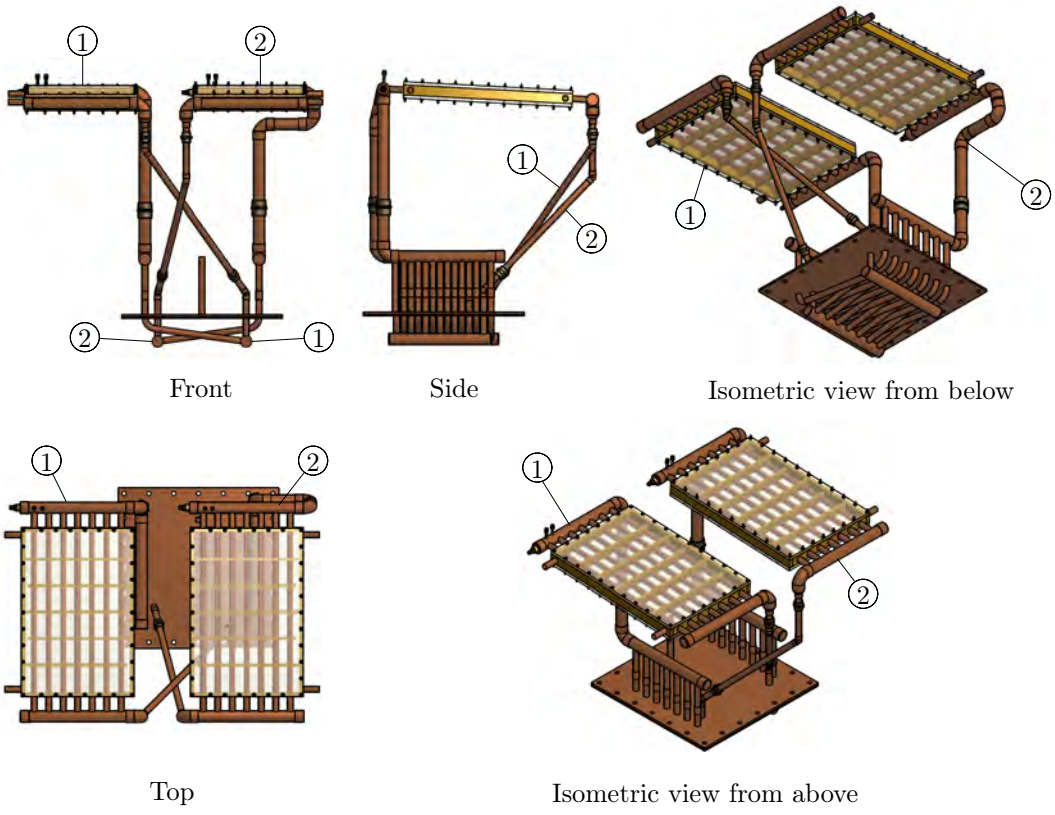

Figure 5.5: Secondary loop shown in different orientations showing the layout of both the heat pipes, numbered 1 and 2, that make up the secondary loop

essary 28 mm pipe connections were soldered to line it up with a compression fitting that was soldered above a bend connected to the vapour collection manifold. The vapour distribution manifold also received two Schrader valves for the charging of the working fluid and release of non-condensible gases within the secondary loop, item 9 in Figure 5.2. The final completed secondary loop set-up with both heat pipes can be seen in Figure 5.5.

5.1.3 Expansion and constant head tank

The expansion tank, an opaque plastic tank ϕ800 mm and 800 mm high, of the primary loop performed a dual purpose. Firstly, it was needed to pressurize the system so that the internal pressure was above atmospheric pressure allowing for the removal of dissolved non-condensible gases in the primary loop. Secondly, the tank was of sufficient size to contain the liquid expanded out of the primary loop when phase change occurred. The tank was fitted with a connection for the expansion line and an overflow pipe at its base and served as the filling point for the primary loop.

The expansion tank was connected to the primary loop, with ID 25 mm heater hose, at point 7 shown in Figure 5.1. The expansion tank was initially placed outside on the roof of the laboratory adding an additional ± 8 m of

pressure head allowing the preliminary tests of test batch 1 to reach a maximum temperature of ± 117 °C. Due to the time required to heat up to 117 °C, as well as safety concerns for the structural integrity of the windows at high temperatures, the expansion tank was brought into the laboratory, as seen in Figure 5.1, with the maximum working temperature reduced to ± 110 °C as well as a reduction in heat losses from the expansion line and tank. A total length of 10.89 m of radiator hose was required to connect the expansion tank to the primary loop.

The constant head tank, item 9 in Figure 5.1, was supplied with enough cooling water so that it overflowed ensuring the pressure head of the cooling water supplied to the experiment remained constant and was independent of pressure fluctuations in the building's water works. The cooling water pipes were arranged as such the mass flow rate of the water coming from the condenser could be measured in the lab at the base of the primary loop. The flow rate was controlled by changing the height of the discharge point relative to the ground as seen in Figure 5.1.

5.1.4 Orifice plate flow meter

The orifice plate had to measure the volumetric flow rate in both directions. The ASME standard for measurement of fluid flow using small bore precision orifice meters was consulted and considerations such as orifice diameter, $0.15 \leq d_{orifice}/D_{pipe} \leq 0.7$, equidistant flange tap distance from orifice plate, 1 in, and lengths of pipe before and after the orifice plate ($l/D_{pipe} > 20$) were taken from the standard (ASME, 2003). The flow meter was calibrated with the measuring equipment rather than the standard formula used to calculate the flow rate as the flow was expected to flow in both directions thus falling out of the scope of the standard.

The orifice plate set-up was constructed in the horizontal direction to minimise the effect gravity would have on the pressure readings. To have the orifice plate in the horizontal plane the pipe work had to jut out from the base of the reactor as seen in Figure 5.6. This protrusion was designed such that the minimum length of pipe leading to the orifice would satisfy $l/D > 20$ and as seen in Figure 5.6 with $621/31 > 20$.

The orifice plate was made from ϕ36×4.5 mm stainless steel with a ϕ16 hole in the center. The ϕ16 mm hole had 45°×2 mm chamfers on either side leaving 0.5 mm in the middle. Two flanges, item 2 and 4 in Figure 5.6, to join the left and right sides were machined from stainless steel with a ϕ31 mm hole through their centre with a step machined in so that an ID 31 mm pipe could fit inside and be welded. The one flange's step, item 4 Figure 5.6, was shorter allowing a ϕ36.1×5 mm hole to be cut in from the other side. This ϕ36.1 mm hole would house the orifice plate and the 0.5 mm difference in widths would allow the gasket to seal around the orifice.

As the orifice would measure flow rates in both directions it was decided to use equidistant flange tap holes so that readings for forward and reverse

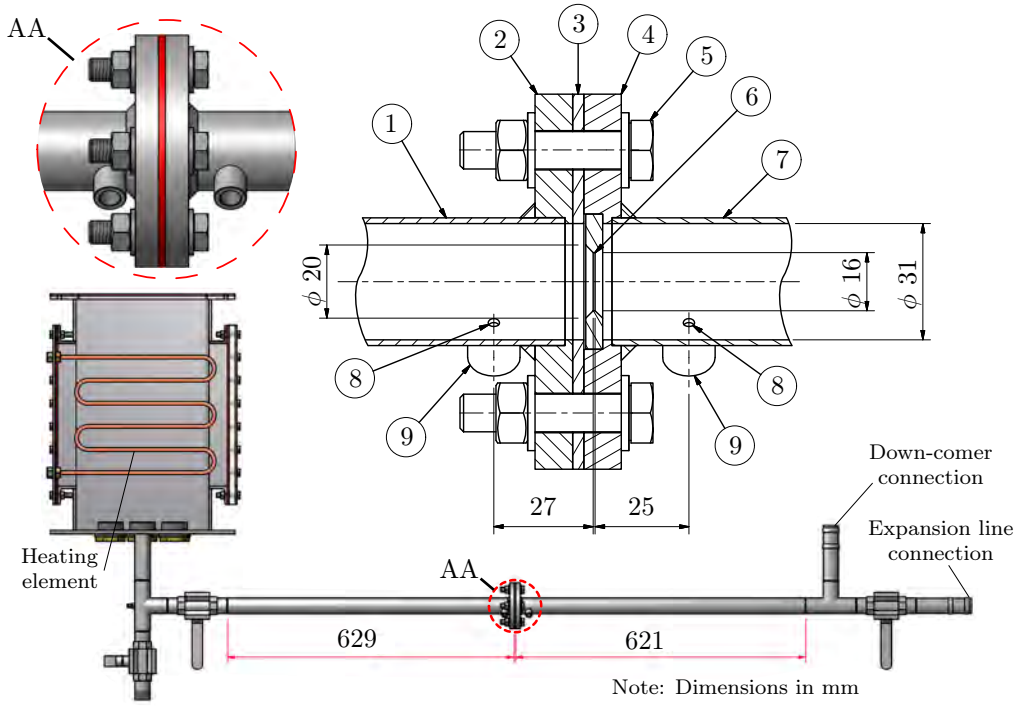

Figure 5.6: Bottom: Base of reactor with pipes and valves with cut away to display interior of reactor. Top left: Enlarged view of orifice plate exterior with pressure tap connection sockets. Top right: Assemble drawing of orifice plate showing: 1) & 7) stainless steel tubes; 2) & 4) orifice flanges; 3) gasket; 5) M10 bolts; 6) orifice plate; 8) ϕ3 mm pressure tap holes; 9) threaded connection sockets

would have similar absolute ranges and profiles. The ϕ3 mm pressure tap holes were placed at different distances from the orifice, as seen in Figure 5.6, so that when the flanges were tightened together and the gasket compressed, the resulting distance of each hole from the orifice would be ± 25 mm (ASME, 2003). The internal surface surrounding the pressure tap holes was smoothed to ensure it did not affect the local pressure.

The pressure taps orientation was initially on top of the pipe but was later changed to just off the centre of the pipe at the bottom. The change in location of the pressure taps was done after an air bubble was found in the one pressure line mid-way through a test even after the line was fully purged of air at the beginning of the experiment test. By having the taps at the bottom it ensured no air bubbles would collect in the pressure lines and just off centre minimised obstruction from the possible collection of particles. The pressure lines were transparent and connected to pipe connectors that were screwed into the pressure tap sockets.

5.2 Working Fluid, Materials and Heating Elements

Water was chosen as the working fluid for the primary loop because it is the primary source of coolant in most nuclear reactors. Furthermore, water is well researched and its properties are well defined. Methanol was used as the working fluid for the secondary loop as it is readily available, cheap and is more volatile than water. The volatility of methanol was necessary as it would allow the secondary loop to be purged of air at a lower temperature compared to if water was used. The vapour pressure of methanol is above 1 atm at 70 °C after which the purging of air is possible.

Stainless steel was used for the majority of the experiment as it was relatively inexpensive, accessible, corrosive resistant and easily manufacturable. Copper was used for the heat transfer sections due to its high thermal conductance thus reducing the effect of its thermal resistance on the results. Copper was used for the steam drum lid as it allowed pipes passing through the lid to easily be soldered to it. The frame was made from mild steel. All bolts used on the stainless steel components were stainless steel to prevent any anode cathode reactions.

Polycarbonate was used for the windows of the set-up as it had dimensional stability at temperatures up to 130°C. The gaskets used for the primary loop were made from high temperature resistant silicon sheets. The gaskets for the secondary loop were made from closed-cell neoprene sheets. Isover-duct wrap, a 25 mm thick thermal insulation glass fibre blanket with an aluminium foil laminate on the one side, was used to insulate the experiment. The blanket was placed in two layers around the majority of the experiment to reduce heat losses to the environment.

The experiment used 9 kW of electrical heating elements to simulate power input from a nuclear core. The power to the elements was supplied by a 3 phase cable with 3 kW per phase. Each 3 kW element was supplied with electrical power independently. Each element had its own switch and using a Variac to vary the voltage supplied to one of the elements, from 0-230 V, allowed the power input to be set anywhere between 0-9 kW.

In initial testing the three heating elements used were 3 kW Kwikheat geyser elements. The surface heat flux, ≈12 W/cm^2, of the geyser elements in initial tests proved to be too high as discussed in Section 6.3. Six, custom made, 1.5 kW elements with a surface heat flux of 3.2 W/cm^2, were installed instead of the geyser elements. Figure 5.6 shows the custom elements shape and placement within the reactor, and also shows the blanked off holes of the geyser elements at the base of the reactor.

5.3 Instrumentation

The measurement of the flow rate within the primary loop, the voltage supplied to the heating elements and the temperature at different points of experimental set-up was required. The power input into the system could be measured by

the taking of the voltage supplied to each element. The voltage could be converted to power through $P = V^2/R$.

The volumetric flow rate in the primary loop was measured from the pressure drop over the orifice plate. The rate of sampling for measuring this pressure difference had to be high enough so that the transients caused by boiling could be captured. The range of pressure measurements was also expected to be large as the system was expected to have small flow rates when operating with only single phase, and large positive and negative flow rates during two-phase flow operation. The pressure transducer, therefore, had to not only measure quickly but also accurately for the entire range of flow with great sensitivity to minor fluctuations in pressure.

The temperature increase over the elements was measured at the inlet and exit of the reactor. The temperature at the exit of the reactor, above the reactor, would be where the temperature in the loop should reach its maximum. A temperature profile along the riser was also desired so the effect of heat losses and transients of the temperature during heating up and boiling could be observed. The temperature at the end of the riser was needed in order to know the temperature of water/steam being supplied to the steam drum. The steam drum's condensate/liquid pools temperature as well as the steam space temperatures were also required. The secondary loop's evaporator external temperature would use the steam space temperature. The condensate return temperature was also required to be measured so that it could be compared to that of the theoretical model.

The internal temperature of the secondary loop was also required as well as the temperature near the top most point to ensure that the non-condensible gases were removed. The temperature of the cooling water before it entered and after it left the heat exchanger was measured along with the mass flow rate of the cooling water. Knowing both the flow rate and temperature difference the energy extracted by the heat exchanger could be calculated.

The details and further explanations on the data acquisition system, namely: equipment; thermocouple specifics and positioning, and the data post processing procedure is found in Appendix C.

5.4 Thermocouple and Orifice Flow Meter Calibration

The thermocouple probes and orifice flow meter calibration procedure and results can be found in Appendix D. The calibration of the thermocouple probes resulted in all the calibrated values falling well within ± 0.5°C of the reference temperature probe value. The orifice flow meter was calibrated for a flow range of ± 0.8 l/s at different temperatures. Temperature was found not to have a noticeable influence on the results. For low flow rates, those below ± 0.1 l/s, the calibration of the flow meter was found not to be accurate as 25 % of the calibration points had an error larger than 10 %. For flow rates below ± 0.05 l/s, no repeatable calibration points could be captured due to the exceptionally small flow rate. With no data available for flow rates

below ± 0.05 l/s no conclusion can be drawn about the accuracy of the results, however, the power function used to predict flow rates is expected to enlarge the error at small flow rates, particularly for small perturbations around zero, due to a point of inflection at (0,0) of the curve fit.

6 Observations

This section deals with the visual observations made during experimentation. Where possible the phenomena observed were captured using cameras. The primary loop was designed with viewing windows to allow for good insight into the experiment's internal operation. The observations recorded were made during the twenty-seven, 2 to 8 hour, experiments performed on the experimental set-up. During individual test runs similar general observations were made despite many of the tests having different objectives.

6.1 Flashing In Riser Section

The riser section was placed above the reactor section with the purpose of creating a pressure increase in the reactor. The idea was that this increased pressure would prevent water from boiling in the reactor but rather let it flash in the riser tube or steam space. The experiment was designed with the idea that the level at which this boiling occurred could be controlled. However in experimentation it was found that the control of the level of the boiling was not easy to accomplish.

The working fluid of the primary loop was observed to have a repetitive transitory pattern. A flow pattern of one of these transitory occurrences consisted typically of the water boiling near the vapour-liquid surface interface with not many bubbles in the riser section as seen in frame (1) of Figure 6.1. A hot plume of water would then rise from the reactor with the upper part of the plume boiling and flashing violently in the riser section. This is seen in frames (2) and (3) of Figure 6.1.

Flashing happened normally well below the liquid-steam interface, with the nucleation sites observed at the gasket between the window section and the riser. The flashed steam bubbles would then rise quickly in the riser section creating a very churned-up flow pattern. The steam bubbles would not all rise at the same speed and typically after a flashing incident there would be a stream of steam bubbles flowing behind the main plume bubble coming from still active nucleation sites, as seen in frames (4) and (5) of Figure 6.1. Frames (4) and (5) of Figure 6.1 also show the steam bubbles' movement up the riser section. The bubbles in frame (5) would make their way up the riser and the cycle would repeat with the time between repetitions varying greatly.

The characteristic rapid radially diverging burst of bubbles is shown in frame (3) in Figure 6.1 (indicated by the star). Figure 6.1 illustrates the relative violence of the flow phenomena, where the steam bubbles were ejected sideways, and sometimes downwards, from the nucleation sites on the windows. The bubbles ending up shooting towards the middle of the riser section. This sudden ejection of steam is apparent by the bubbles radiating away from the nucleation site at the edge of the window next to the star on Frame (3) in Figure 6.1 with Figure 6.2 showing an enlargement of the specific section. The

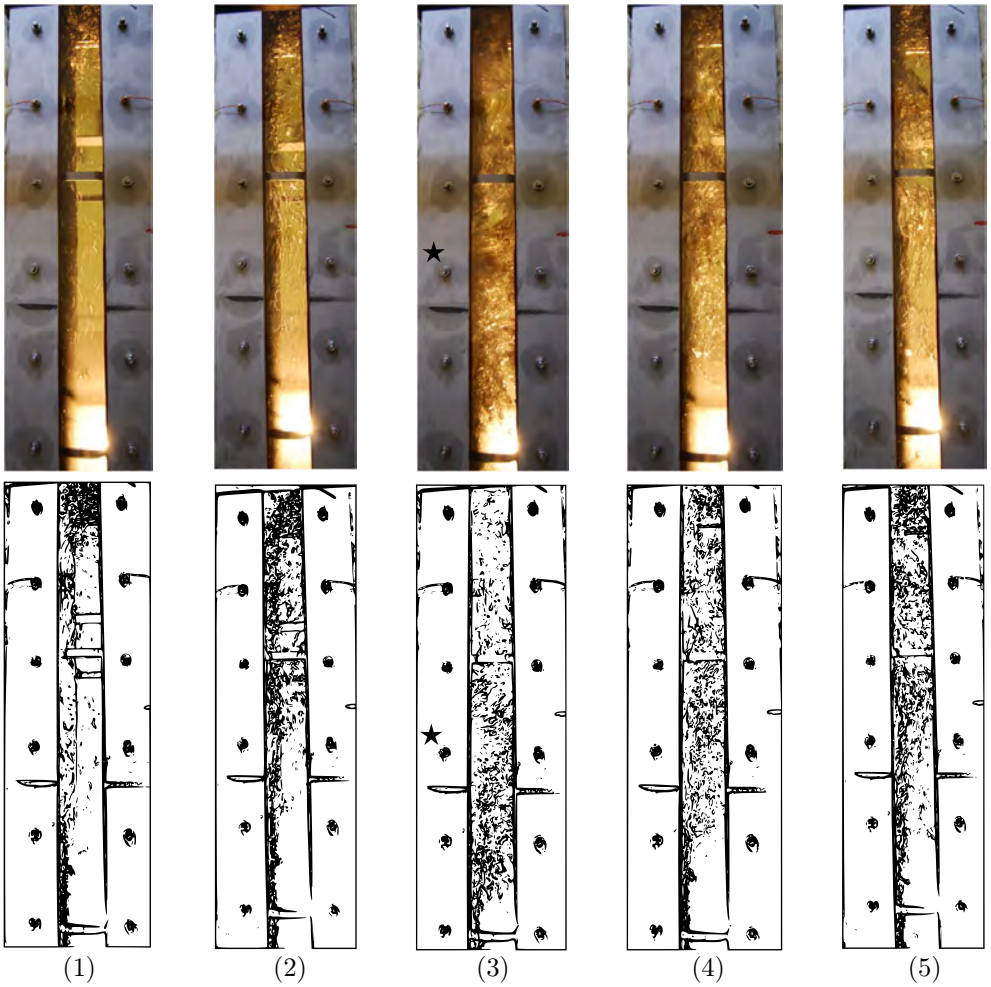

Figure 6.1: Flashing shown in riser section with photos and tracings of same section at consecutive times. The darker areas in the lower represent the two-phase boiling regions with the white area representing predominantly single phase flow.

opaque red arrows in Figure 6.2 show the direction of the steam bubble flash along the inside face of the window, however, the bubbles were also blasted towards the middle of the riser section. The flashing also corresponded with large changes in the differential pressure measurement across the orifice plate.

Despite the flashing being repetitive in nature there was no discernible frequency in the repetition of the event. Furthermore, the flashing intensity also showed no discernible pattern but, it was noted to be dependent on the power input and removal. For example, at the end of a test when the primary loop was still in heat pipe mode, the air relief was opened, thus reducing the pressure, and flashing took place along the entire length of the riser.

When the water in the riser flashed violently it would shake the entire experiment within its frame. The flashing in the riser was observed to be so great

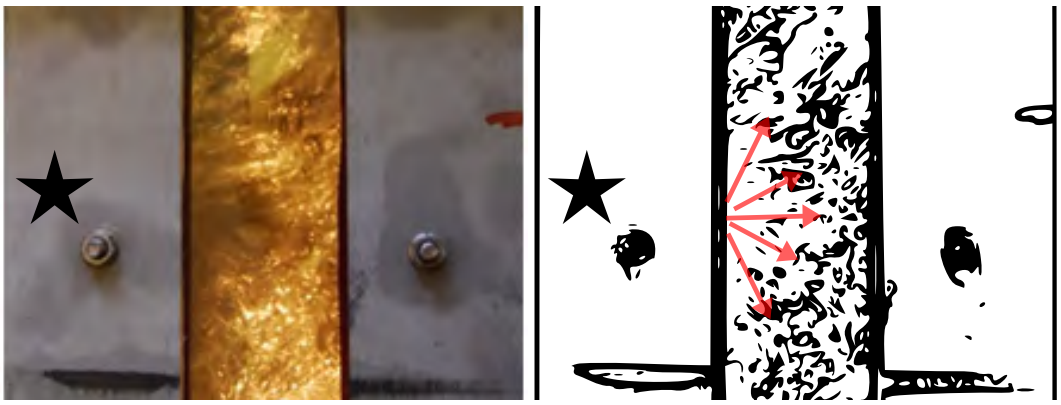

Figure 6.2: Enlargement of starred section of frame (3) of Figure 6.1 with opaque red arrows indicating the bubble blast resulting from flashing

at times that a slug filling the entire ϕ200 mm riser tube was created. This slug, upon reaching the top, would fling liquid into the steam space if present. The slug would not necessarily be formed by one individual bubble but could be created by a combination of large bubbles. Bubbles sequentially following one another, it was observed, would catch each other using the eddy/vortex created behind the bubble to drag the lower bubble towards it, combining with it.

6.2 Convective Plumes

When the primary loop started up, all the water was in liquid phase and had stratified with the higher temperature water lying above the cooler water in the primary loop. When the heating elements were turned on the experiment did not respond instantaneously with a flow rate. Instead after some time plumes of different density water were noticed rising and sinking in the stratified and stationary water at the riser section. The difference in density refracted the light making it possible to see the plume formations and movements through the windows of the experiment.

It was observed that as the experiment heated up the discernible plume/stratified interface moved up the riser slowly, continuously mixing as it proceeded up the riser. In the wake of the distinguishable plume/stratified interface, all the way to the bottom of the riser, was a column of plumes varying in size and mixing/interacting with one another, filling the entire diameter of the riser. Within this column the higher-temperature plumes could be seen moving upwards. The upwards movement of the plumes decreased in intensity as the plumes moved away from their source in the reactor. The observed plumes were hotter than the surrounding fluid because as the plume moved up and passed over a thermocouple probe tip the temperature reading increased noticeably. Similarly, once the heat exchanger was removing heat (but in the opposite direction) the lower temperature plumes moved downwards with the

movement intensity increasing as it neared the evaporator section of the secondary loop.

The plume/stratified interface would move all the way up the riser into the steam drum. As the primary loop heated up, the convective mixing plumes were not as visible as during start up. However, when the heat exchanger activated, the low temperature water was clearly visible as plumes falling off the evaporator section and mixing with the then more discernible hot plumes exiting from the top of the riser.

As the tests progressed, and during boiling, the plumes were still visible. The point of flashing and path of the bubbles was found to coincide with the hot plume as it progressed up the riser. When tracking a plume, the plumes were noticed to be narrow in cross-sectional area at times as the plume elongated. This narrowing sometimes coincided with the presence of a bubble below the narrowing. The bubble would not continue to rise due to buoyancy as it reached the narrowing. Instead, the bubble would collapse and 'flash' through the narrowing of the hot plume and forming again above the narrowing. The movement happened extremely quickly, seemingly not driven by buoyancy forces, but rather by the bubble flashing itself to above the narrowing. The bubbled can be described as tunnelling through the narrowing to the hotter bulk of the plume above.

6.3 Boiling and Flashing From Surface of Heating Elements

The primary loop was initially designed to use three, 3 kW, domestic geyser heating elements to heat the water in the reactor section. The geyser heating elements performed poorly as their heat flux was too high, resulting in nucleated boiling and flashing on the surface of the elements. Figure 6.3 (a) is a picture of the geyser element where bubbles from nucleated boiling are coming off the surface of the heating element; the subsequent bubble column can be seen. It was found that the small bubbles from the nucleated boiling would not collapse as they progressed up the riser section.

Although in Figure 6.3 (a) it seems that the nucleated boiling is not that excessive, as the temperature of the entire loop reached operational point water would start flashing aggressively off the elements. The flashing in the reactor was observed to be so energetic at times that flashing would start in the reactor or at the bottom of the riser only. This aggressive flashing from the elements was unacceptable as it made large steam bubbles that did not collapse but travelled up the riser, effectively negating the reason for having a riser in the first place; no bubbles should form in the coolant flowing through the reactor.

To combat the flashing and nucleation, new elements with a lower surface heat flux were installed, as mentioned in section 5.2. It was observed that the new elements did not help with the nucleated boiling as anticipated but rather provided a larger surface area for nucleation to take place, thus aggravating the premature nucleation problem. The new elements with the lower heat flux

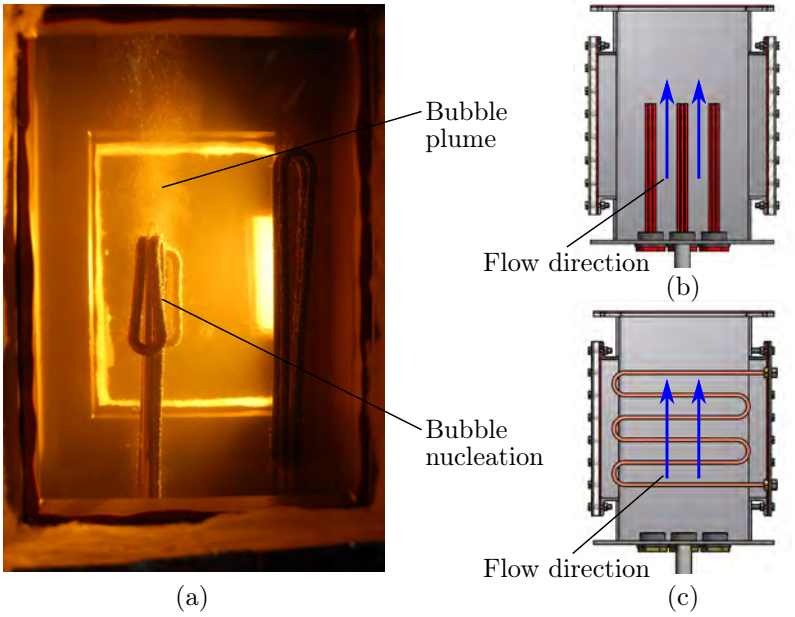

Figure 6.3: (a) Picture of nucleated boiling taking place on initially inserted 3 kW domestic heating elements; (b) CAD section of initially inserted elements showing vertical orientation with flow; (c) New heating elements showing horizontal orientation across flow

did, more importantly, significantly suppress large bubble formation at the elements. Unlike the geyser elements, seen in Figure 6.3 (b), the new heating elements, seen in Figure 6.3 (c), were horizontal with the flow crossing over them, this orientation was observed to have a disruptive effect on the flow over the element. In comparison to the geyser elements, where the hot water rose along the elements heating surface, the better mixed flow over the new elements, along with the lower heat flux, resulted in less large bubble formation at the elements, with bubbles observed to be no bigger than a 6 mm diameter sphere.

6.4 Steam Space Establishment

Figure 6.4 shows consecutive photos looking into the steam drum from the back at an angle. In each of the photos in Figure 6.4 the protrusion of the riser tube is visible in the steam drum with the base of the frame of the closest window at the bottom of each frame. In Figure 6.4: frame (1) shows the steam drum completely filled with liquid water; frame (2) shows a relatively small bubble plume, just before it strikes the top of the steam drum, from the onset of flashing within the riser; frame (3) shows the start of the establishment of the steam space in the steam drum with the white line indicating the vapour-liquid interface; frame (4) shows the uneven nature of the vapour-liquid surface interface at an interface height similar to that in frame (3); frames (5) and (6) show the progressive expansion of the steam space as seen by the decreasing

height of the vapour-liquid interface; frame (7) shows the water liquid-vapour interface approximately in line with the riser section's outlet; frame (8) shows the final expanded steam space expanded to below the riser exit but above the window frame's bottom.

The flow phenomena surrounding the outside of the secondary loop heat pipe heat exchanger evaporator section was of particular importance for the modelling of the outside thermal resistances. Observations such as those reflected in Figure 6.4 led to the flow surrounding the evaporator section to be classified into three distinct regimes, firstly a liquid regime (frame (1)), secondly a two-phase regime (frames (2) to (6)) and thirdly a condensing heat transfer regime (frames (7) & (8)). It must be noted that when flashing in the riser was aggressive enough water was often sprayed up onto the secondary loop's evaporator section. Thus, the changeover between the two-phase and gas regimes is when the splashing of the evaporator by flashing was minimal. The change between the liquid and two-phase regimes is when steam bubbles

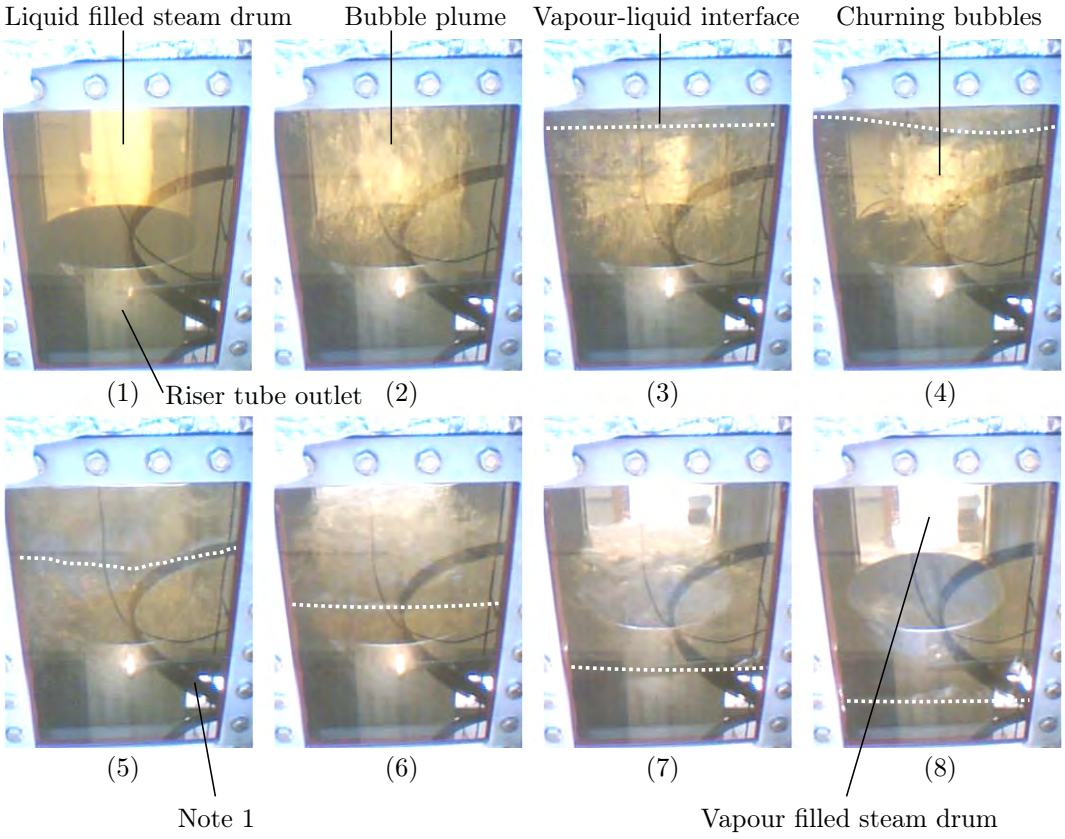

Figure 6.4: Consecutive selected photos showing the establishment of a steam space in the steam drum with dotted white line indicating the vapour-liquid interface on the closest window [Note 1: Reflection of safety straps of vertical ladder and window in every frame]

become present near the evaporator section.

The churning nature of the two-phase flow behaviour in the steam space is seen by a change in the vapour-liquid interface as highlighted by the dotted line in frame (4) when compared to frame (3). For large plumes, as found in frame (5) of Figure 6.4, it was found that the vapour-liquid interface could change shape and height considerably with the vapour-liquid interface approximated by the white dotted line in this case.

The establishment of a steam space was easily achieved. However, keeping the steam space at a constant level when the expansion line was open proved to be highly difficult. Keeping a steam space at a specific level required the energy in from the electrical elements, $\dot{Q}_{ele}$, to be balanced by the losses, $\dot{Q}_{loss}$, and the energy extracted by the secondary loop, $\dot{Q}_{HP}$.

Keeping the steam space at a constant level was further complicated by the thermal inertia of the primary loop. Furthermore, with the valve to the expansion line open, as soon as the steam space contracted the cooler water drawn into the primary loop from the expansion line would reduce/stop the boiling in the riser section. Once the boiling had stopped or decreased the steam space would collapse further, due to not enough steam created to replace the steam that is condensed by the secondary loop heat exchanger, drawing in more cold water from the expansion line. The process would continue until the steam space had collapsed completely as not enough energy could be added by the heating elements to boil, the now, lower temperature water. To eliminate this problem it was necessary to establish the steam space and close the valve between the expansion line and the primary loop, resulting in a so called *heat pipe* mode of operation; *heat pipe* mode implying that the primary loop was operated with a steam space and a fixed amount of water similar to a thermosyphon-type heat pipe which is typically half-filled with liquid while the remaining volume is filled with its vapour.

If the steam space was expanded too rapidly the hot water ejected from the primary loop would enter the expansion line, see Figure 3.1, and boiling would take place in the expansion line. As the steam space expanded and contracted the water ejected from the primary loop was mixed with the water from the expansion tank, heating it up. Thus, if the steam space was expanded and contracted a number of times the water in the expansion tank and line would become hot enough and start boiling.

6.5 Geysering Above the Riser In the Steam Space

Figure 6.5 shows consecutive photos looking into the steam drum allowing the entire edge of the riser tube outlet to be seen. The frames in Figure 6.5 showed the geysering phenomena that took place during tests when the liquid/steam interface was below the lip of the riser outlet. The photos in Figure 6.5 in the given frame order were taken in rapid succession.

In Figure 6.5: frames (1), (2), and (3) show the bubbling liquid level in the riser rising; frames (4) and (5) show the liquid pouring over the riser edge into

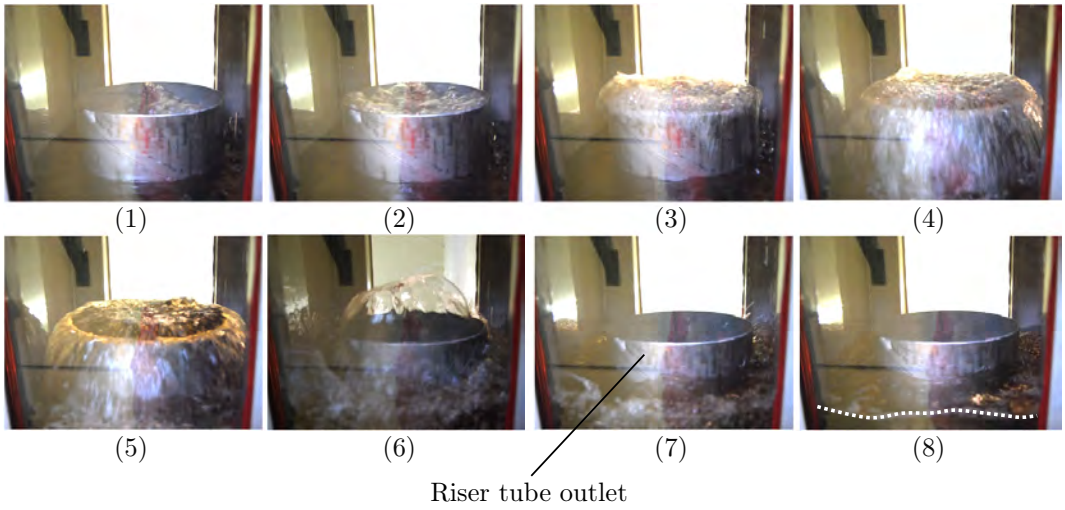

Figure 6.5: Effect of geysering in steam drum when water level is below riser lip with photos taken at consecutive times

the steam drum; frame (6) shows the bubble-slug's departure from the riser outlet with a thin film of liquid surrounding the vapour bubble clearly visible; frames (7) and (8) show the calming of the steam drums water pool and its new water level post-geysering shown with a white dotted line.

The rising of the liquid level in the riser section, in Figure 6.5 frames (1), (2) and (3), was due to a bubble-pump type of action created by the periodic arriving of bubbles, that originated due to flashing in the riser. The speed and ferocity at which the liquid water would geyser out of the riser was quite remarkable. The more aggressive the flashing in the riser was, the greater the resulting geysering or splashing of the water-vapour mixture within the steam drum vapour space. When the steam space was allowed to expand it was found that there came a point where geysering could not take place any longer.

It was observed that the condensate that collected on the wall of the evaporator section of the secondary loop did indeed run down the tube to the internal manifold, as seen in Figure 5.4, where it dropped off into the steam drum, missing the riser, as intended by the design. This condensate run off resulted in a cooler steam drum water pool. During the design process it was decided that the riser section would extrude into the steam drum somewhat to prevent water from the steam drum flowing back into the riser. As seen in Figure 6.5 the riser protrusion did indeed prevent the flow of the steam drum liquid back into the riser, forcing the liquid through the down-comer.

When the liquid level in the steam drum was very close to the base of the steam drum and corresponding with aggressive flashing/geysering in the riser, water was seen to be pushed out from the entrance of the down-comer and back into the steam drum. This reverse flow from the down-comer was particularly apparent when the experiment was operated in heat pipe mode.

The down-comer was made of glass and the entrainment of vapour bubbles in the steam drum liquid into the down-comer was never observed.

7 Results

This chapter firstly deals with the results from testing the experimental set-up, as discussed in Chapter 5, which was built to meet objectives 1 and 4 of the research. Secondly, the chapter explains how the constants required for the theoretical model of the secondary heat exchanger loop, as developed in Chapter 4 to meet objective 5, were obtained through semi-empirical means using the experimental results, thus completing objective 6. Finally, the validity of the theoretical model and simulation of the secondary loop and the primary loop is investigated and compared to experimental results, completing objective 7.

7.1 Experimental Results

The experimental results of both the primary and secondary loops are presented in this section. The section deals with the heat extracted by the secondary loop, it then discusses the flow rate response of the primary loop. The section then briefly mentions a few points relating the primary loop temperature response which is elaborated on in Section 7.4. The activation temperature of the heat pipe of the secondary loop is discussed and explained with the section concluding with an energy balance of the experimental set-up.

As mentioned in Chapter 6 a total of twenty-seven tests were performed on the primary loop. The testing was broken up into three sequential batches. Batch one consisted of 14 tests performed with the flow rate measured at 0.1 Hz with different sized restrictions of diameter, 25 mm, 50 mm and no restriction (160 mm) at the inlet for the riser section above the reactor. Test batch two consisted of 4 tests performed after a recalibration of all measurement equipment and a new pressure transducer used to measure flow rate at a frequency of 10 Hz. Final test batch three consisted of 9 tests where both the primary loop and secondary loop were tested.

For the objectives of this thesis only the last batch of nine tests' results are discussed as they consist of both the primary and secondary loops. Tests 1–3 of the third batch utilised both heat pipe loops that were built to form the secondary loop while the subsequent tests, tests 4–9, only used one of the secondary loop's heat pipe loops.

7.1.1 Heat extraction by the secondary loop

Both heat pipes built forming the secondary loop were charged with methanol and tested for tests numbered 1–3. Different combinations of parallel and series flow of the two separate condenser were tested. It was found that the use of only one heat pipe heat exchanger was sufficient to extract heat from the primary loop. Heat pipe 2 was chosen as its final dimensions more closely represented the design, particularly in the angles of orientation of the condenser, when compared with heat pipe 1. The liquid charge from heat pipe 1 was removed

for subsequent tests with only heat pipe 2 used in tests 4–9.

7.1.2 Flow rate response of experiment

Figures 7.1, 7.2 and 7.3 show graphs of the flow rate response of the primary loop as measured by the orifice flow meter at different time intervals for tests 6, 5 and 9 respectively. It can be seen from the graphs (a) that the flow rate response was noticeably different for test 6, where the expansion line valve was open with a constant cooling water flow rate, compared to both test 5 and test 9, where the primary loop was run without cooling until *heat pipe* mode was entered.

Graphs (b) (in Figures 7.1, 7.2 and 7.3) show a similar start up transient for all three tests. This start up transient was present in all the tests with there being zero flow rate at the beginning, then as the fluid in the primary loop warmed up it would start circulating. The start up transient was similar as no heat transfer was taking place despite the cooling water of the secondary loop heat exchanger running in test 6 when compared to both test 5 and test 9 where the cooling water was not flowing. The only noticeable difference seen in graphs (b), when comparing test 6 to both test 5 and test 9, is that the flow rate of test 6 levels out at a lower value. This lower flow rate value is attributed to the lower power input of ±7.7 kW for test 6 compared to ±8.3 kW in tests 5 and 9. The power input was found to be the main influencing factor on this start up transient effecting both when the flow rate speed started to increase as well as the speed once the flow rate had been established and flattened out. The difference in starting point and flattening out of the flow rate can be seen in Figure 7.4 which shows the start up transient for different power inputs, with a stepwise power input from $\dot{Q}_{ele}$=0 s at t<0 s to $\dot{Q}_{ele}$ at t=0 s.

The establishment of the vapour space in the steam drum takes place when entering *heat pipe* mode. The flow rate, as water is expanded out of the primary loop and into the expansion line, can be seen in graph (c) of Figures 7.2 and 7.3 by the flow rate becoming negative. The difference in magnitude of the negative flow between graphs (c) of Figures 7.2 and 7.3 results from a larger vapour space allowed to be formed in test 9. In test 5 the water steam interface was ±12 cm while in test 9 it was ±36 cm below the lip of the riser in the steam drum. No heat is extracted by the secondary loop heat exchanger (no cooling water in condenser) until the expansion line valve is closed and *heat pipe* mode is entered.

The larger steam space created in test 9 prevented the carry over of liquid from the riser into the steam space from geysering. The lack of carry over in test 9 resulted in the oscillation of flow around zero, seen in Figure 7.3 for $t > 140$ min. In test 5, where the size of the steam space allows for carry over, the flow oscillates around a flow rate of ±10 l/min as seen in Figure 7.2 for $t > 150$ min.

In other tests it was found that the level of the steam/water interface had an effect on the mean of the oscillations of the flow rate when the loop was run

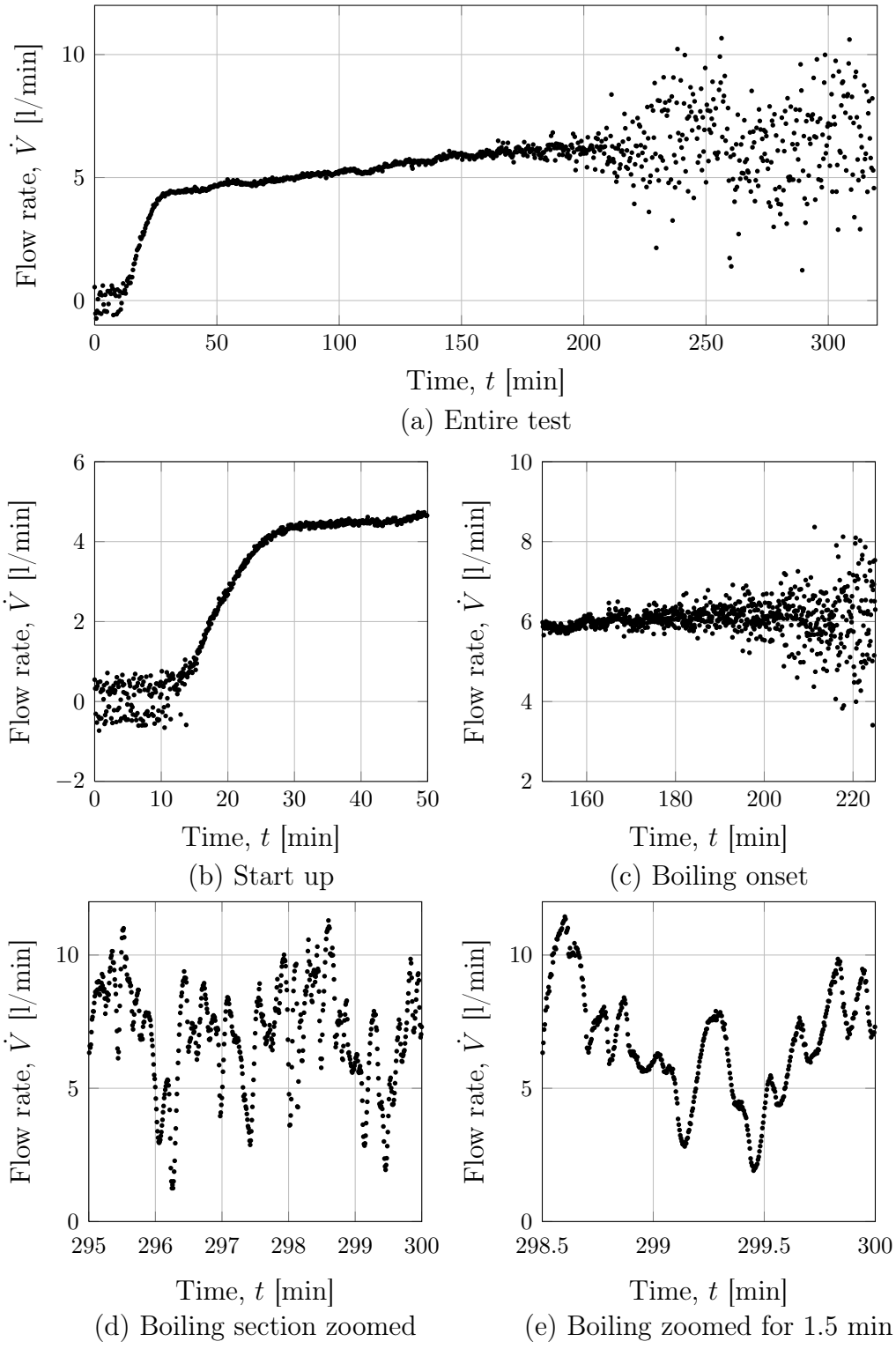

Figure 7.1: Volumetric flow rate as a function of time and at different time intervals for test 6 with expansion line valve open.

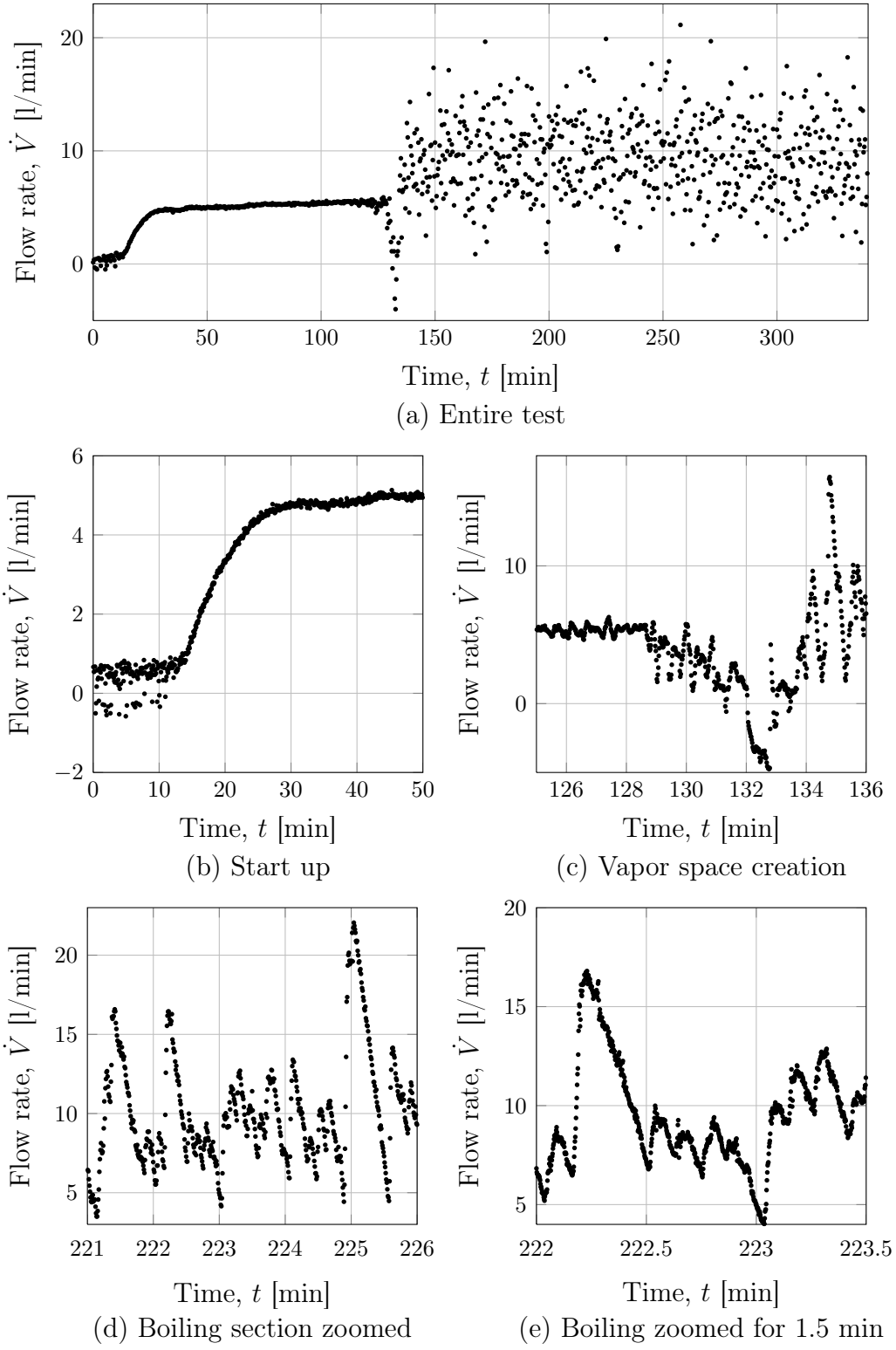

Figure 7.2: Volumetric flow rate as a function of time and at different time intervals for test 5 with, from $t > 132.8$ min, the primary loop run in *heat pipe* mode with carry over of liquid from the riser section into steam drum permitted.

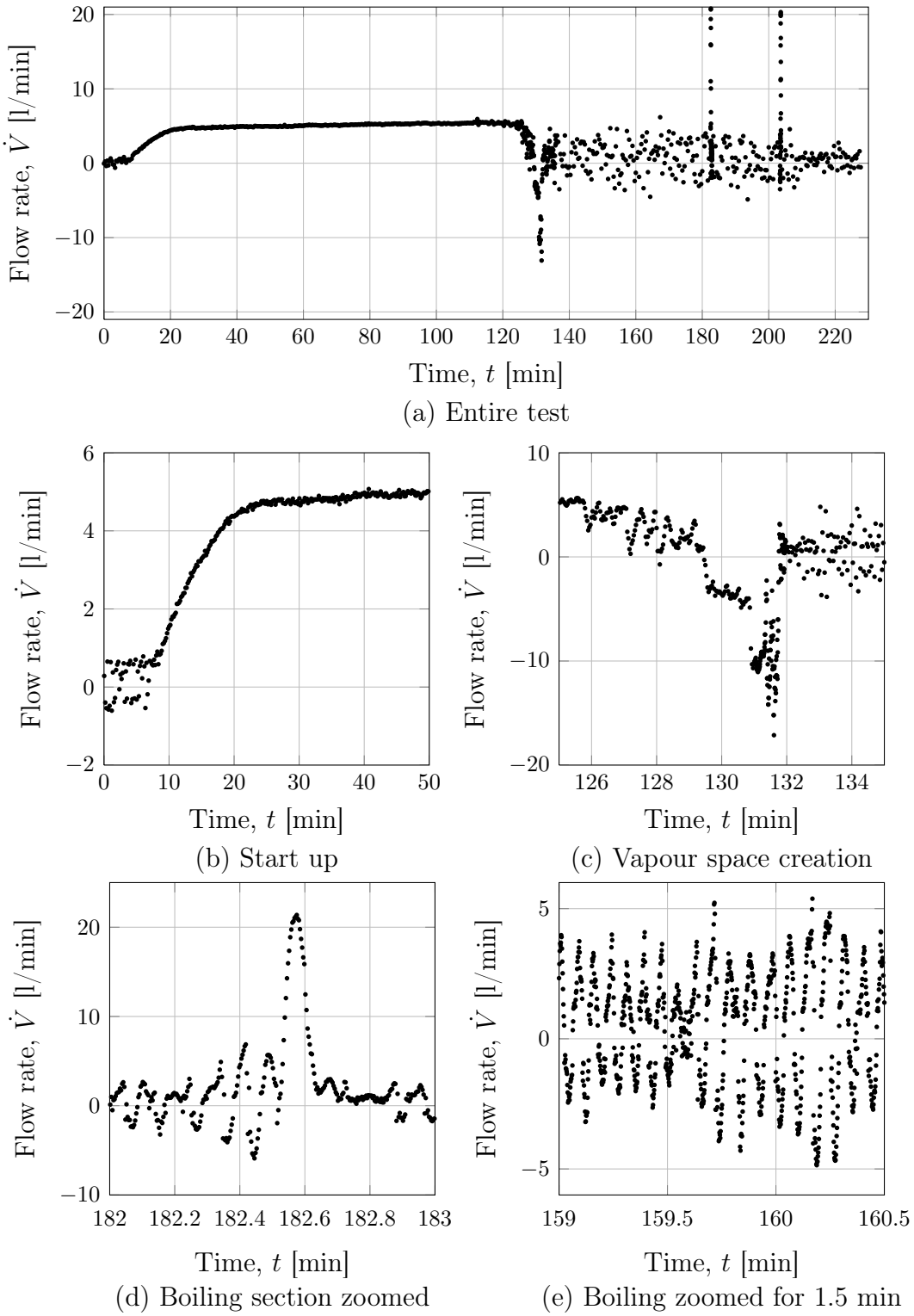

Figure 7.3: Volumetric flow rate as a function of time and at different time intervals for test 9 with, from $t > 131.8$ min, the primary loop run in *heat pipe* mode set in such a way that no carry over of liquid from the riser section into the steam drum could occur.

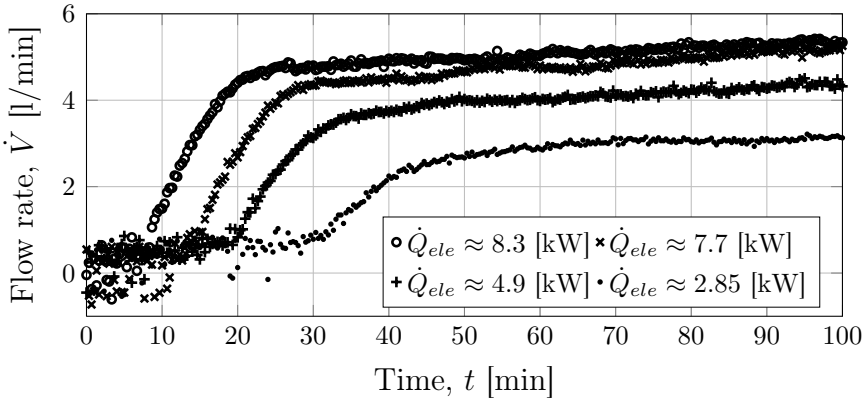

Figure 7.4: Graph shows the volumetric flow rate start-up transient for different power inputs for tests 6–9

in heat pipe mode. It was found that if one increased the steam space from above the riser lip, as found at the end of test 6, the flow would oscillate around the same average value until the steam/water interface reached the riser lip. As the steam/water interface passed the riser lip the oscillating flow rate's mean value would increase while the riser lip prevented more liquid carry over from falling back into the riser. The increase in the mean value of oscillations would continue until no further carry over fell back into the riser with the oscillating mean value reaching a maximum and now dependent on the aggressiveness of the flashing in the riser section. The mean oscillation flow rate value would decrease with an increase in steam/water interface distance below the riser lip, until no carry over took place.

In test 9 there were two cases where the flashing was incredibly aggressive with a bubble being formed that filled the entire riser cross-section. These two flashing events are visible in Figure 7.3 at $t = 182.6$ & 204 min with spikes in the flow rate as carry over from the riser as well as liquid being forced through the down-comer ended in the steam drum. Despite the aggressive nature of the flashing, the effect on the flow rate is different for test 9 when compared to flashing in test 5. The flashing in the riser and the effect on flow rate for test 5 is visible in Figure 7.2 (d) at $t = 225$ min. Although only one instance of aggressive flashing is shown in Figure 7.2 (d), similar flashing incidents continued for the duration of the *heat pipe* mode of test 5.

As can be seen in Figure 7.2 (d) at $t = 225$ min there is a sharp rise in the flow rate with a linear decrease thereafter. This pattern is prevalent throughout the *heat pipe* mode of test 6 even with smaller spikes as seen in graph (e) of Figure 7.2 having a similar shape (a sharp rise with gradual decrease) and can be interpreted as the water being carried over into the steam drum, initiating the spike, then draining into the riser through the down-comer from the steam drum. The pattern of boiling in test 5, test 6 and test 9 is noticeably different from one another. In Figure 7.2 (e) the spikes in boiling are sharp and have a jagged-like appearance whereas in Figure 7.1 (e) the oscillations are more

rounded at turning points. Figure 7.3 (e) shows very steep, sharp oscillations around zero happening at a much higher frequency when compared to test 5 and test 6. The amplitude of the oscillations of test 9 results, seen in Figure 7.3 (e), is most likely exaggerated by the method of measurement as discussed in Appendix D.

The one very noticeable difference between running the primary loop with the expansion line valve open is that the onset of boiling is a gradual one, as seen by the ever greater dispersion of results, from $t > 160$ min, in graphs (a) and (c) of Figure 7.1. The dispersion becomes greater, reaching a peak just after $t = 250$ min where it contracts and thereafter diverges again. The contraction at $t = 258$ min corresponds with a dip in the reactor inlet temperature of ± 60 °C. This sudden drop in temperature is attributed to a collapse in the steam space and subsequent inflow of cooler water from the expansion line. The effect of the collapse of the steam space was noticed in all the tests where the expansion line valve was open. None of the operation conditions were altered in the case of the collapse in test 6 with the collapse seemingly provoked by ever greater oscillations of the steam space size due to boiling/flashing, resulting in an oscillation that was just too great.

In test 6 just after $t = 50$ min a small bump in the flattened volumetric flow rate start up transient is visible in Figure 7.1 (a). This bump corresponds to the kick in of the secondary heat pipe and its subsequent transferring of heat. It was found that the flow rate in the primary loop increases when heat is extracted from it compared to when heat is not extracted. This is expected as the driving buoyancy terms would have more disproportionate temperatures (as the down-comer is drawing in the water cooled by the heat exchanger), and in turn densities, in the riser section when compared to the down-comer thus increasing the flow rate.

7.1.3 Primary and secondary loop temperature response of experiment

At start up of the primary loop the temperature distribution was typical of stratified water with higher temperature readings the higher up from the base. The thermocouple probes' values showed subtle variations in temperature as plumes of water passed the measuring tip. These subtle variations were most apparent at the exit of the reactor at start up, taking place before a flow rate was established.

The temperature of the system would rise until it reached its operation point. The temperature of the operation point was determined by the internal pressure, dependent on the height of the level in the expansion tank or when in *heat pipe* mode the saturation temperature of the steam drum (in turn dependent on heat in-putted and extracted to the primary loop). When the steam space collapsed it corresponded with a large drop in temperature of the reactor inlet water flowing in from the expansion line.

7.1.4 Secondary heat exchanger activation temperature

In Figure 7.5 (a), for tests 4 through to 9, the internal temperature measured by channel 16 (see Appendix C), $T_{HP2,in}$, in the vapour distribution manifold of heat pipe 2 of the secondary heat pipe loop heat exchanger is plotted against the temperature measured at the top of the steam drum, T_{eo}, which is the temperature surrounding the evaporator of the secondary loop. $T_{HP2,in}$ had a similar temperature response for the different tests, with a sharp rise for the temperature range $55 < T_{eo} < 62$℃, as is seen in Figure 7.5 (a). This phenomena is referred to as the activation/kick-in of the heat pipe as the internal temperature of the secondary loop condenser is now sufficiently high enough to start transferring heat.

The onset of heat transfer by the secondary loop heat exchanger is shown in Figure 7.5 (b) for Tests 6 and 7. Cooling water was run through the condenser of the heat pipe from the beginning of the test, however, heat transfer only begun when $T_{eo} > 60$ °C. This onset of heat transfer corresponds well with the activation of the heat pipe at $T_{eo} \approx 60$ °C in both graphs (a) and (b) of Figure 7.5. Due to the repetition of this activation phenomena it was decided that for theoretical modelling purposes, the heat pipe only started to transfer heat once $T_{eo} > 60$ °C.

7.1.5 Energy account

In Appendix A the theoretical heat loss, $\dot{Q}_{loss}$, for the primary loop is discussed and a simple equation relating the temperature difference, $\Delta T = T_{reactor} - T_{amb}$, to the heat losses is found. Where $T_{reactor}$ and T_{amb} are the temperatures at the reactor exit in the riser and that of the ambient air respectively. A cool down heat loss calibration of the experimental set-up would not give a representative measurement of the heat losses as the water in the primary loop

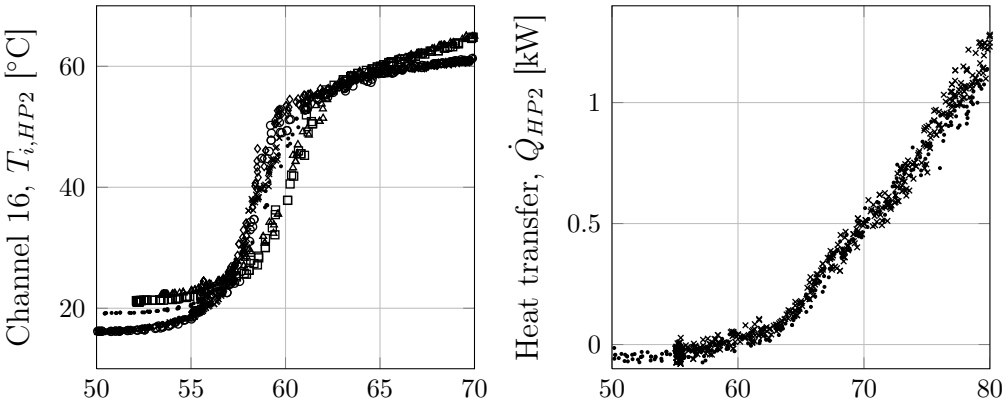

(a) Tests 4-9 results (b) Test 6 & 7 $\dot{Q}_{HP2}$

Figure 7.5: Activation of secondary heat pipe loop heat transfer (a) showing the increase in internal temperature for tests 4 to 9 and (b) heat transferred by the heat exchanger versus the temperature from the top of the steam drum

would stratify with no flow rate present. Thus, the equation derived from the theoretical model to model the heat losses was used. The discrepancy of an energy balance of the primary loop is

$$\dot{Q}_{bal} = \dot{Q}_{ele} - \dot{Q}_{HP} - \dot{Q}_{loss} \qquad [\text{W}] \tag{7.1}$$

where $\dot{Q}_{ele}$ is the energy input from the heating elements in the reactor and $\dot{Q}_{HP}$ is the heat extracted by the secondary loop. A complication found with the experimental set-up was that the energy retained by the water as well as the energy contained in the water that was expanded into the expansion line could not be calculated accurately from the experimental results. Operating the experimental set-up in steady state, as discussed in section 6.4, was only achievable when the primary loop was run in so-called *heat pipe* mode. *Heat pipe* mode also ensured that no water was leaving the primary loop and thus the loop could reach a state of relative equilibrium.

An energy balance was performed from data selected from time ranges in the *heat pipe* mode of operation, once the experimental set-up had reached relative equilibrium. Eight separate test ranges from three different tests' data were used to perform the energy balance. The results of the energy balance are seen in Figure 7.6 with a mean error of 909.5 W and a standard deviation, σ, of 197 W. The unaccounted for energy, $\dot{Q}_{bal}$, is approximately 10% and $\dot{Q}_{loss}$ is approximately 5% of the total power input, $\dot{Q}_{ele}$, on average. As the energy balance was performed on the experimental set-up running in *heat pipe* mode the results fall into a narrow range of temperature difference, ΔT, as seen in Figure 7.6.

Additionally, the error due to a maximum expected error of 0.5°C (see Appendix D) in the measurement of the temperature difference (which had an average value of 13.2 °C and $\sigma = 2.09$ °C) of the cooling water used to calculate $\dot{Q}_{HP}$, gives a mean error of ±275 W with a $\sigma = 46$ W for the $\dot{Q}_{HP}$ data used to calculate $\dot{Q}_{bal}$. Noting that the mean value of $\dot{Q}_{HP} = 7.054$ kW with a

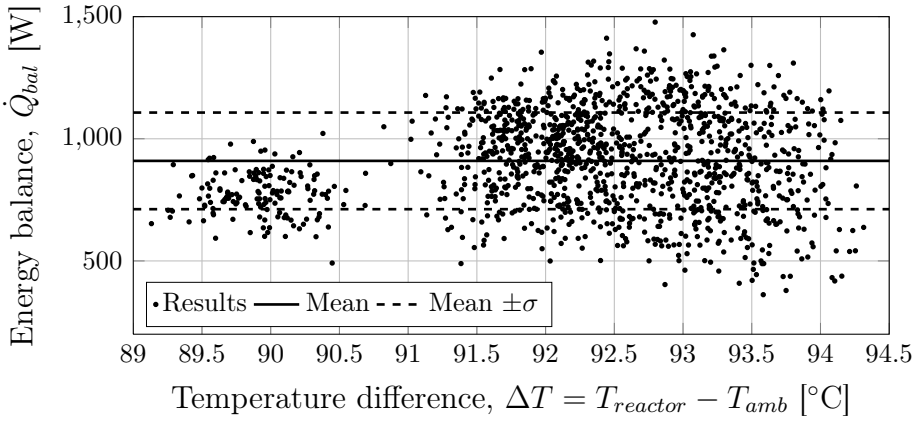

Figure 7.6: Energy balance of experimental set-up showing results, the mean value and 1 standard deviation from the mean

$\sigma = 162$ W, the average worst case combination gives $(275+46)/(7054-162) = 0.046$. This means that the error due to thermocouples could be up to 5% of $\dot{Q}_{HP}$ used in the energy balance. The thermocouple error can either be beneficial or detrimental to the energy balance, however, as it is expected to be random with no specific bias. The error is reduced when averaged for a number of data points as done to calculate $\dot{Q}_{bal}$.

7.2 Secondary Heat Exchanger Loop - Semi-Empirical Characterisation

This section will discuss how the constants required for the thermal resistance theoretical model of the secondary loop heat exchanger were acquired using the experimental results. The determined constants are also compared with the experimental results in order to check the validity of the values obtained. An uncertainty/error propagation analysis was performed in Appendix C.3 for the results used to characterise the secondary loop heat exchanger. The major sections under consideration in the order they are dealt with are the internal and external resistances of the evaporator section and the external water side resistance of the condenser section. For the effectiveness-NTU approach to provide initial values for the theoretical model the heat transfer coefficient $(UA)_c$ is required. The process of finding $(UA)_c$ and function used to represent it is discussed in Appendix F.

7.2.1 Internal resistance of the evaporator section

In order to characterise the thermal resistance of the evaporator's internal boiling linear regression was performed using the experimental results. Equation 4.17 was regressed to find the constants for equation 4.16. The surface temperature of the internal wall of the evaporator was not practical to measure. Thus, it was decided to find $C_1 = ln(C_{sf})$ and $C_2 = n$ using $T_s = T_{eiw}$ calculated from $T_{eiw} = T_{eo} - \dot{Q}_e(R_{eo} + R_{ew})$. T_{eo} was measured by thermocouple channel 4 as shown in Figure C.1. The heat entering the evaporator could not be calculated from the experimental results and was approximated as the heat extracted by the cooling water. The approximation of $\dot{Q}_e = \dot{Q}_c$ implies that losses to the environment by the secondary loop heat exchanger were negligible. The resistance of the wall, R_{ew}, was expected to be minor and was calculated using equation 4.7 where the wall thickness is $\delta_{ew} = 0.7$ mm, $k = 401$ W/(m^{2}K) and the external surface area of the evaporator is $A_e = 110.451 \times 10^{-3}$ m^2.

Using all test results from when the evaporator was condensing on the outside ensures that R_{eo} was also at a minimum and was calculated using equation 4.8 where $D_c = 0.015$ m. Setting $T_{sat} = T_i$ and the heat flux $\dot{q}''_{ei} = \dot{Q}_c/A_e$ and with $\dot{Q}_c$, T_i and T_{eo} all coming from the experimental results allowed Y to be calculated from equation 4.18. Noting that $X_1 = ln(Pr_l)$ where the Prandtl number is evaluated at the internal temperature T_i.

The results of the linear regression of C_{sf} and n can be found in Table 7.1. The values found for C_{sf} and n when compared to the work of Pioro (1998) do

not differ excessively. The surface, on which boiling takes place, preparation also influences the values of C_{sf} and n. Faghri (1995) states that experimental heat transfer coefficients are significantly different than those given by classical Nusselt analysis. Taking into account the expected difference compared to classical Nusselt analysis and that the internal surface state in the secondary loop's evaporator being unknown, further justifies the results as well as the method used to get the results.

Table 7.1: Results of linear regression for Rohsenow n and C_{sf} values for equation 4.16

Value	Model	Methanol/Brass	Ethanol/Copper
n	$2.6967245\,^{+1.63\%}_{-1.44\%}$	1.7	2.3
C_{sf}	$1.5573\text{E-}03\,^{+4.36\%}_{-5.08\%}$	0.0026	0.00079
R^2	0.419884	Values from Pioro (1998)	

% error calculated in Appendix C.3

Using the input data for the linear regression under the typical operating conditions the new predicted values are plotted against the experimental values in Figure 7.7. It can be seen in Figure 7.7 that the majority of predictions are well-bounded by the ±30% accuracy limits. Çengel *et al.* (2011) states that the error of using the Rohsenow equation can be ±100%. Furthermore, as the secondary loop is a closed two-phase thermosyphon and involves a boiling process, significant uncertainties arise in the repeatability and predictability when calculating the overall heat transport (Faghri, 1995).

7.2.2 External resistance of the evaporator section

As explained in section 4.1 the evaporator was modelled for three different operational regimes, namely; condensing, liquid and two-phase regimes. In

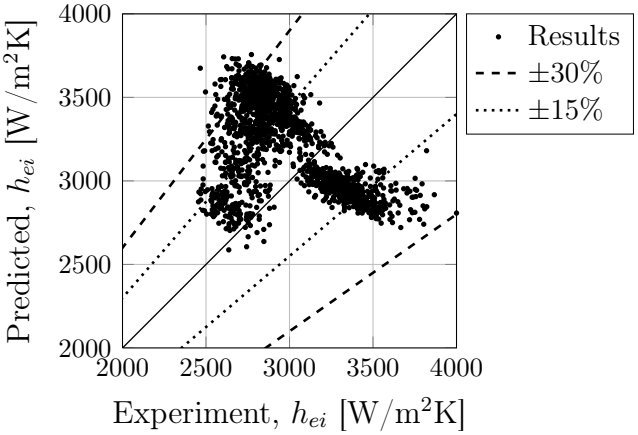

Figure 7.7: Linear regression results for Rohsenow equation showing experimental results plotted against predicted results and accuracy bounds

the condensing regime the external resistance was modelled using equation 4.9. Equation 4.9 was then used along with the wall resistance, R_{ew}, as the known resistances to determine the unknown resistance R_{ei} using experimental results which in turn was used to find C_{sf} and n in equation 4.16. For the liquid regime, equation 4.20 was used as the known resistance, along with the wall resistance, to find the correlating factors C and n from the test results for equation 4.10.

A shortcoming found with this method was that, due to the heat pipe start up delay characteristic, the resistance predicted using equation 4.20, R_{ei}, was too large for the experimentally determined T_i, T_{eo} and $\dot{Q}$. With the predicted value of R_{ei} being too large it implied that equation 4.16 was not valid and would then make the Matlab®-script, used to calculate $R_{eo,l}$, try to make $R_{eo,l}$ negative which is unrealistic. This is due to the fact that the Matlab®-script would calculate $R_{eo,l}$ through an iterative process. Thus, the Matlab®-script was written so that it would remove the non-applicable data from the set if $R_{eo,l}$ was calculated to be negative.

For the liquid regime, equation 4.10 was used with the Rayleigh number as defined by equation 4.11 with D=0.015 m and all fluid properties evaluated at the film temperature. The results of the linear regression, using the script-reduced liquid regime experimental data set, when used in combination with equation 4.20, were $n = -0.6652115$ and $C = 2.1680E + 06$ with a $R^2 = 0.951142$. A comparison of the outside heat transfer coefficient, h_{eo}, for script-reduced liquid regime experimental data set and predicted results can be seen in Figure 7.8.

The value found for C, as well as the overall heat transfer coefficient used to find C, are unreasonably high for a liquid to wall natural convection heat transfer process. This is most likely due to the internal thermal resistance, R_{ei}, being overestimated by equation 4.20, implying it is not valid for the liquid regime. This inaccuracy is then in turn compensated for by the large values for C found from the regression. Thus, the model can be seen as acceptable, however, only for the specific configuration as found in the applicable experimental operating regimes. The liquid regime is also not the operational point of the secondary loop heat exchanger and its unique geometry and location further complicate its external thermal resistance analysis.

Both equations 4.8 and 4.10, from which $R_{eo,l}$ and $R_{eo,g}$ are determined, are mainly based on the thermo-physical properties of the fluid surrounding the evaporator. During the two-phase regime the expansion or contraction of the steam space required the expansion line to be open. The water level in the expansion tank varied only slightly at the start of each test. The pressure is thus relatively constant from test to test as the system was exposed to a similar pressure head through the open expansion valve. With a constant pressure and a boiling process the bulk temperature of the fluid surrounding the evaporator was the saturation temperature. The bulk temperature, T_{eo} was used in the calculation of thermo-physical properties. This similar and

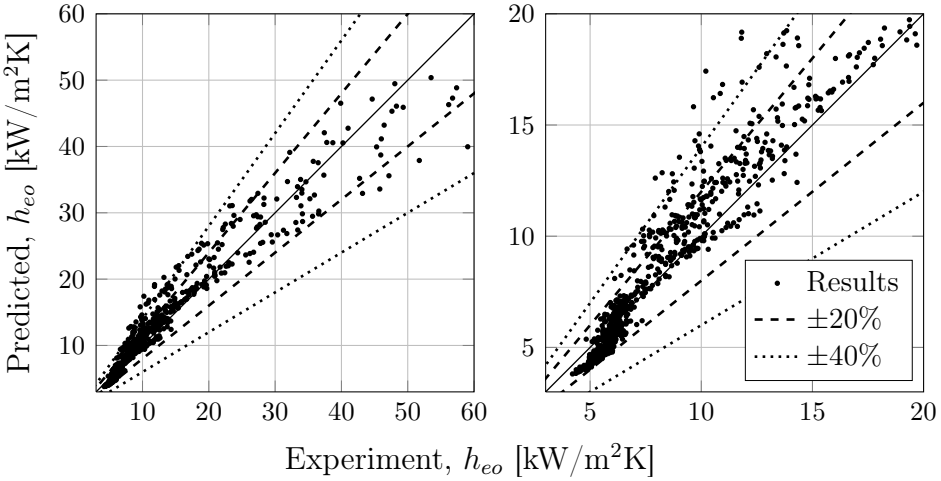

Figure 7.8: Results for equation 4.12, $h_{eo,l}$, showing experimental results plotted against predicted results and accuracy bounds

constant T_{eo} resulted in relatively constant values for $R_{eo,l}$ and $R_{eo,g}$.

When the secondary loop evaporator's outside was exposed to a two-phase operating regime, equation 4.14 was used to determine the thermal resistance $R_{eo,2\phi}$. $F_{2\phi}$ was varied between zero and one. $F_{2\phi}$=0.3 was found so that the majority of the predicted results would fall within the 20% error band as seen in Figure 7.9(a). As $R_{eo,l}$ and $R_{eo,g}$ give relatively constant values for the two-phase regime, it implies that even though the experimental results change the prediction from the model remains the same. This is as both $R_{eo,l}$ and $R_{eo,g}$ do not take into account the flow conditions on the outside of the evaporator. Despite this, the entire thermal resistance model is able to predict the majority

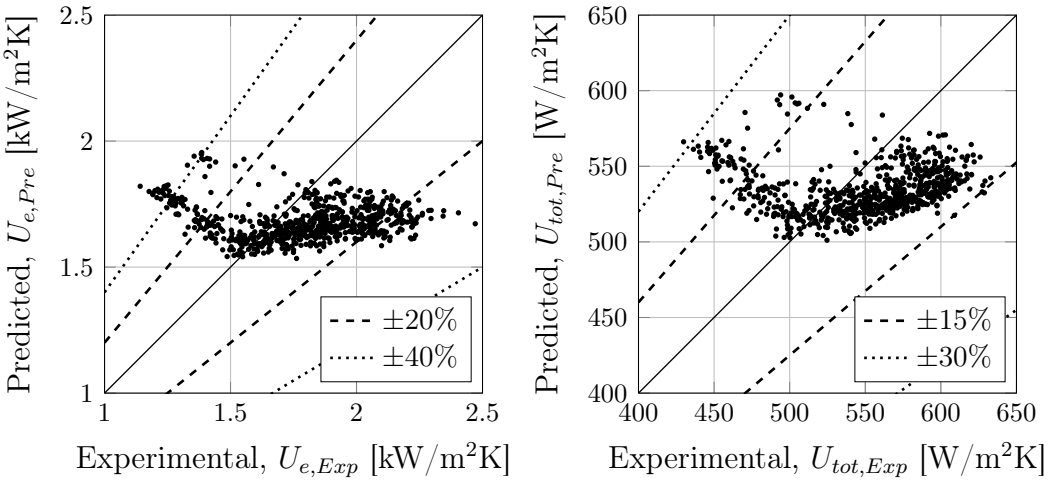

(a) Evaporator U (b) Overall U

Figure 7.9: Results for equation 4.14 with $F_{2\phi} = 0.3$, showing experimental results plotted against predicted results and accuracy bounds

of the experimental results within ±15% accuracy as seen in Figure 7.9(b). As the flow conditions surrounding the evaporator were random and transient, due to boiling in the two-phase stage, it was decided that this simplification would suffice as no applicable theory was found in literature.

7.2.3 External waterside Nusselt number for the condenser section

To find the external resistance of the condenser, R_{co}, a similar approach was employed to the finding of constants for equation 4.16. The approach was similar as T_{cow} was not practical to measure and, additionally, would increase along the flow path as the cooling water warmed. R_{ci} based on the h_{ci} from equation 4.27 was used along with R_{cw} and experimental results from the condensing regime to find the external Nusselt number $Nu_{co,exp}$. The condensing regime was used as this would define the typical operational point of the system.

$Nu_{co,exp}$ was calculated with D_h=0.01411 m, A_c=0.1319 m^2 and A_{ch}= 9.6×10^{-4} m^2. The ranges for the experimental results used in the regression were: $67.97 < T_i < 85.44$ °C; $14.76 < T_{cw,in} < 16.40$ °C; $0.1021 < \dot{m} < 0.167$ kg/s and $4.67 < \dot{Q} < 7.8466$ kW. $Nu_{co,exp}$ was then used for the linear regression of equations 4.29 and 4.31 giving the results shown in Table 7.2. With a R^2=0.76 the inaccuracies were too great for Nusselt number prediction. Multiple combinations utilising other variables were thus attempted and it was found that the inlet and outlet temperatures of the water had a considerable effect on the accuracy of the prediction. To account for these effects an adjusting factor of $(Pr_{cw,in} - Pr_{cw,out})$ was combined with equation 4.31 giving

$$Nu_{cyl} = CRe^m Pr^n (Pr/Pr_s)^k (Pr_{cw,in} - Pr_{cw,out})^l \tag{7.2}$$

where $Pr_{cw,in}$ and $Pr_{cw,out}$ are the Prandtl numbers of the cooling water entering and exiting the heat exchanger respectively. As can be seen in Table 7.2, the additional factor resulted in a very good prediction of the Nusselt number as reflected by R^2=0.9999. The constants' values from the regression for equation 7.2 are found in Table 7.3.

Table 7.2: Different models for Nu_{cyl} and corresponding R^2 values

Equation - Nu_{cyl}	**Equation no.**	**R^2**
$CRe^m Pr^n$	4.29	0.6491
$CRe^m Pr^n (Pr/Pr_s)^k$	4.31	0.7667
$CRe^m Pr^n (Pr/Pr_s)^k (Pr_{cw,in} - Pr_{cw,out})^l$	7.2	0.9999

7.3 Secondary Heat Exchanger Loop - Theoretical Results

To establish the validity of the secondary heat exchanger loop's theoretical model it was compared to the experimental results using inputs for $T_{cw,in}$, T_{eo} and $\dot{m}_{cw}$ as measured from the corresponding experimental results. The different operating regimes of the secondary loop are each examined separately and changes are made to the model if required.

Table 7.3: Resulting constants from linear regression for equation 7.2

Variable	Value	Variable	Value
C	0.016799966	n	0.198962404
m	1.005863021	k	-1.555610960
l	0.983949614		

7.3.1 Initial theoretical model results

The secondary loop has three different evaporator external states of operation (the liquid, two-phase and condensing), thus a similar comparison was performed for all three different regimes. The comparisons consisted first of the heat transfer coefficients, then the internal temperature T_i and cooling water exit temperature $T_{cw,out}$ and thirdly the overall heat transferred. The resulting comparisons for the two-phase regime and condensing regimes can be seen in Figures 7.10 and 7.11 respectively.

The theoretical model performed unsatisfactorily for the liquid regime operating condition, as the predicted values had deviations of up to 100% when compared to the experimental results. In comparison, Figures 7.10 and 7.11 show a good similarity between the predicted values and experimental results. The model performs better for the condensation regime than the two-phase regime which was to be expected due to simple approximation of $R_{eo,2\phi}$ in equation 4.14.

7.3.2 Revised theoretical model of liquid regime

The theoretical model predicted the liquid regime experimental results unsatisfactorily by virtue of the predicted results' deviations of up to 100% of the experimentally determined values. This poor prediction is due to a number of factors from the equations to the correlations not being correct or appropriate for the unique operation condition. Tan and Liu (1990) achieved good correlations to experimental data using the effectiveness-NTU approach and an experimentally determined overall heat transfer coefficient. The effectiveness-NTU approach is still undesirable for the purposes of sensitivity analysis on the theoretical model (as it cannot be used in this specific application to find T_i) however the effectiveness-NTU approach was decided to be used solely for the liquid regime using an experimentally calculated total overall heat transfer coefficient. A sensitivity analysis was still able to be done for the operating case (condensing regime) as predictions using a iteratively solved thermal resistance method were sufficiently accurate, as seen in Figure 7.11.

The start-up of the secondary heat pipe is a complex phenomena with the working fluid moving through different stages of boiling before reaching the operating condition where equation 4.16 is applicable. Although it is complex it followed the same basic trend each time. For the purpose of the computer theoretical simulation it was decided to use the effectiveness-NTU approach to predict this trend in a piecewise fashion similarly to equation F.2. The overall

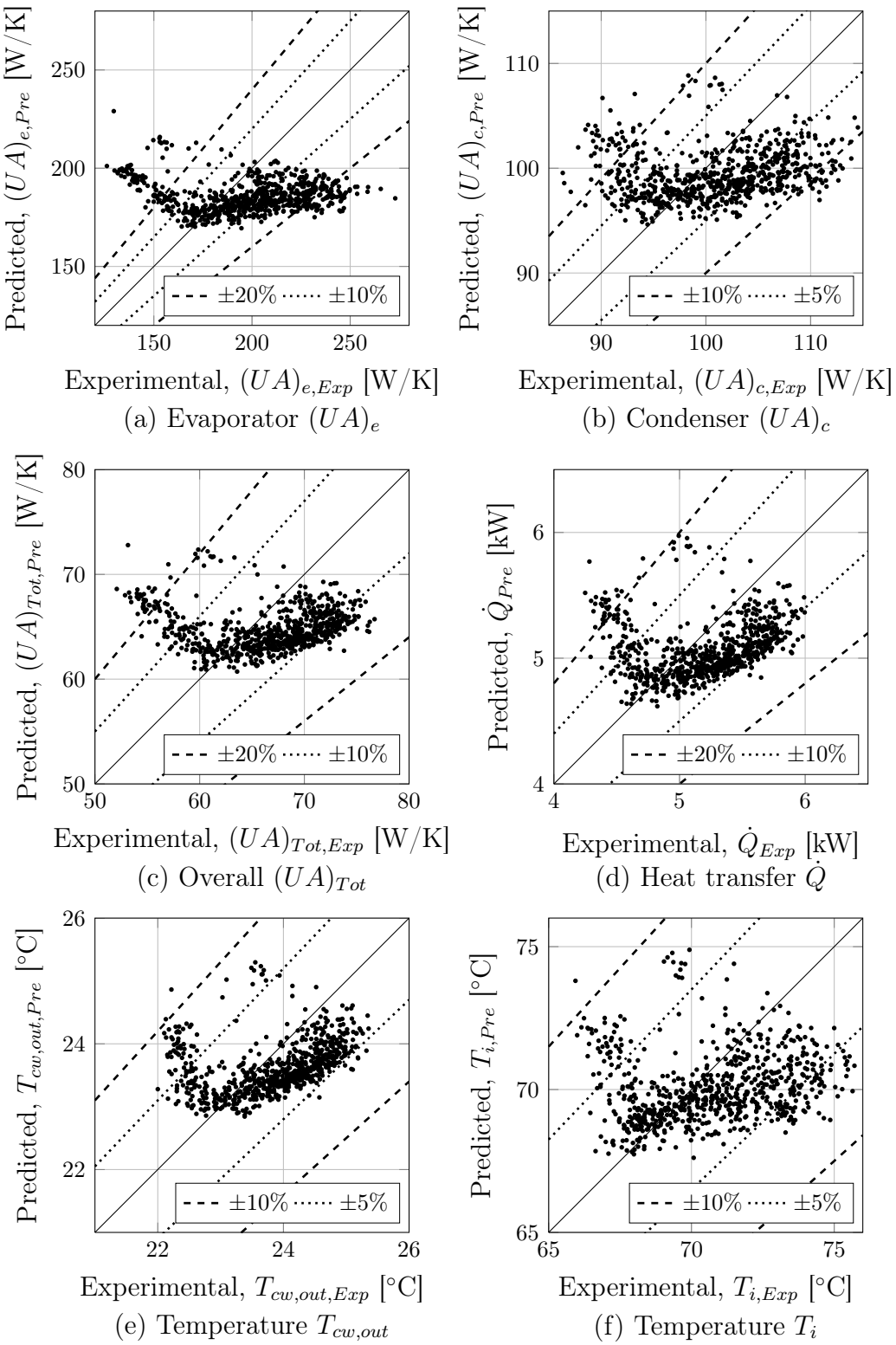

Figure 7.10: Results from theoretical model operating in the two-phase regime compared with experimental results

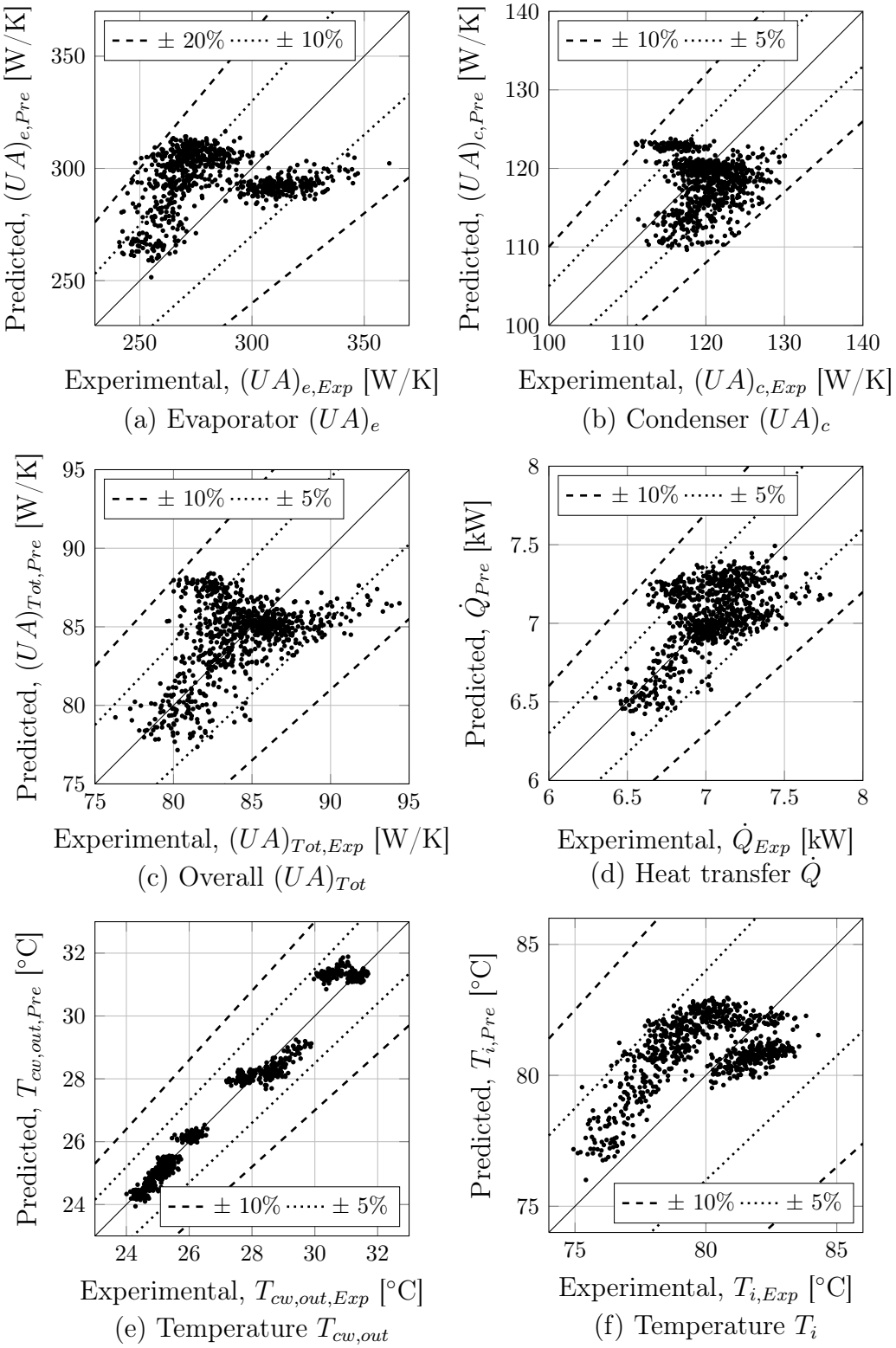

Figure 7.11: Results from theoretical model operating in the condensing regime compared with experimental results

heat transfer coefficient for the entire heat pipe $(UA)_{Tot,l}$ was predicted using the temperature difference between the evaporator outside and the cooling water stream

$$\Delta T_{HP} = T_{eo} - \overline{T}_{cw} \tag{7.3}$$

The value of ΔT_{HP}, with experimentally determined $(UA)_{Tot,l}$, was then used to find a correlation for $(UA)_{Tot,l}$ giving the piecewise function dependent on ΔT_{HP}

$$(UA)_{Tot,l} = f(\Delta T_{HP}) = \begin{cases} 1.034\Delta T_{HP} - 47.55 & \text{if } 46 \leq \Delta T_{HP} < 66 \\ 3.74\Delta T_{HP} - 226.3 & \text{if } 66 \leq \Delta T_{HP} < 73 \\ 1.464\Delta T_{HP} - 62.91 & \text{if } \Delta T_{HP} \geq 73 \\ 0 & \text{if } \Delta T_{HP} < 46 \end{cases} \tag{7.4}$$

The components of the piecewise function can be seen overlaid on the experimental results in Figure 7.12. The results of using the revised model compared with the experimental results showed much better correlation than the thermal resistance model as seen by the small errors of the predicted values in Figure 7.13. At very low heat rates, $\dot{Q}$<0.3 kW, the model's inaccuracy become slightly greater but only exceeding the 30% bound on a few occasions and becoming more prevalent as the $\dot{Q}$ tends to zero. The inaccuracies are expected at the lower heat transfer rates as losses, assumed to be negligible, as well as the effect of measurement errors of ΔT_{cw} have more of an influence on results. As explained in Appendix D, with a small ΔT_{cw} (as found with low heat transfer rates) the thermocouple reading error has a larger effect on the results. This is acceptable for the model as the total amount of energy is small and has little effect on the whole experiment with a heat input of typically more than 8 kW.

The departure from the 45° line found in the results is due to the change in the boiling/condensing conditions of the secondary loop during its activation and, in turn, the change in the piecewise function used, seen in the $T_{cw,out}$ graph at $T_{cw,out,exp}$=18° C and $T_{cw,out,exp}$=20° C in Figure 7.13. The changes in boiling/condensing conditions were not physically observable, taking place

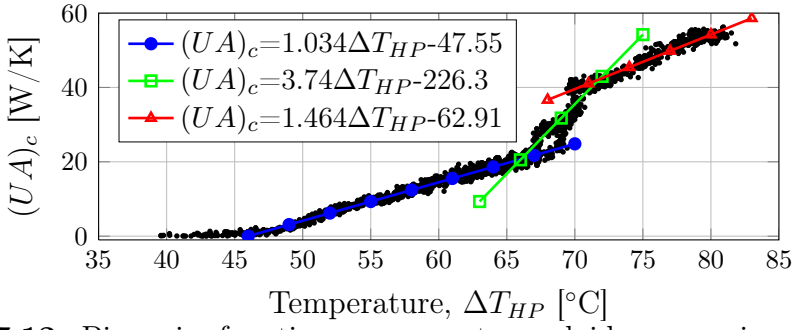

Figure 7.12: Piecewise function components overlaid on experimental results for the liquid regime

inside the heat pipe, thus it has not been speculated whether it was a boiling or condensing change that caused the sudden jump, as seen in Figure 7.12, between the range $65 < \Delta T_{HP} < 73°C$.

7.3.3 Sensitivity of secondary loop theoretical model

The results of sensitivity analysis performed using a basis chosen from test 9, $t = 200$ min, when the evaporator was operating in condensation mode in the steam drum, can be found in Appendix G. The sensitivity analysis was performed on select variables of the secondary loop's theoretical model. From the sensitivity analysis the fact that the evaporator section of the secondary loop's heat pipe was over-designed while the condenser is undersized and the model is sensitive to a change in T_{eo} is evident as noted in Appendix G.

7.4 Primary Loop Theoretical Model Results

The theoretical computer simulation of the primary loop, as presented in section 3.3, general results and operation are discussed in this section. The simulation is based on the equations of change as described in section 3.2. The equations are applied to control volumes of size Δz and the solution is found by predicting values using the equations of change to give vales at time step, Δt, in the future. The program was written for the primary loop with the expansion line open to attempt to simulate the start up transient from single phase through to boiling. The simulation ran for the primary loop in single phase, however, typically when phase change took place the simulation was stopped as it violated the Courant-Friedrichs-Lewy (CFL) condition, see Appendix B.3. The section also deals with the independence of the simulation to the control volume and time step sizes before concluding by discussing the general observations and insights of the primary loop's theoretical computer model.

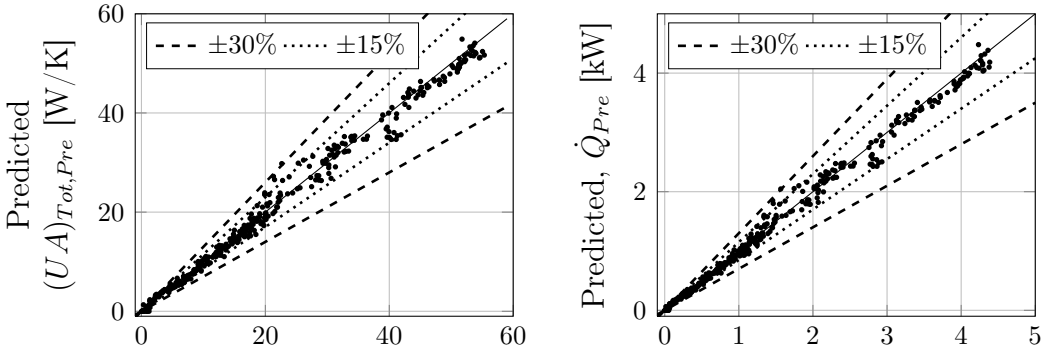

(a) Overall $(UA)_{Tot}$ (b) Heat transfer $\dot{Q}$

Figure 7.13: Results for revised theoretical model of secondary loop operating with the evaporator section's exterior in the liquid regime compared to experimental results

7.4.1 General results

A discussion of the results for specific basic test cases used to test the program of the primary loops theoretical model is presented in Appendix B.4. The specific basic test cases tested were: giving the primary loop a starting forward and reverse flow with no power input; starting from zero flow rate in the primary loop with heat input of 50%, 100% and, 150% of 7668.6 W distributed in the reactor and riser control volumes; starting from zero flow rate in the primary loop with heat input of (7668.6 W) distributed in the down-comer control volumes. The model performs as expected for the specific instance. The change in flows for the starting flow rates tended to zero as expected. The flow was in the positive direction and had higher and lower flow rates for the higher and lower heat inputs distributed in the reactor and riser test cases. For the heating of the down-comer the flow was in the negative direction and larger in magnitude, compared the test cases of heat into the larger reactor and riser control volumes, as anticipated.

The model did not however capture the two phase flow phenomena as the CFL conditions imposed on the simulation were violated due to the expansion of the fluid out of the control volumes during phase change. Thus, though the model was able to run for the single phase its inability to simulate two phase flow means the theoretical approached used is lacking. Furthermore, flow rate oscillations are present in the simulation results where heat was added to the control volumes. These flow rate oscillations were not present in the experimental results. The presence of the oscillations are attributed to the physical response of the theoretical model itself, and was found not to be a result of some numerical error.

7.4.2 Grid and time step independence

The formulation of the grid and its subsequent independence from the solution obtained, forms an essential part of all high-quality computational fluid dynamics studies (Versteeg and Malalasekera, 2007). In the previous works of Ruppersberg (2008), Senda (2012), Dobson (1993, 2012) and Sittmann (2011), which have a similar solution method to the one used to simulate the primary loop, no indication of investigation of grid or time step independence was found. A detailed discussion of the grid and time step independence is presented in Appendix B.5.

The results of the time step size independence investigation showed that the smaller the time step the smaller the flow oscillations became. Noticeable simulation response differences were found as the time step was reduced, however, the results did not converge. When a time step of 10 µs was used an unrealistic result was generated by the computer program. It was found that only the reactor's control volumes were increasing in temperature until they boiled, stopping the program as the expansion caused the Courant number to exceed 0.2.

The unrealistic response was attributed to small time steps reducing the

dominance of enthalpy changes due to convection in the energy equation. This created a situation where the oscillations in expansion and contraction coupled with errors from curve fitting of properties resulted in an energy loss which became dominant. This resulted eventually in a near steady state situation with energy unable to be transported out of the reactor. In other words the transfer of energy due to the flow was negated by errors in curve fits and a small time step allowed for these typically minor numerical errors to become dominant. These problems also highlight that the way expansion and contraction were incorporated requires further attention.

For grid size independence the simulations were run with $\Delta t = 0.01\,\text{s}$ and the maximum size of the control volume, Δz_{max}, was varied from 1.5 m to 40 mm as seen in Appendix B.5.2. It was found that the simulation diverged as Δz_{max} decreased with the oscillations in temperature and flow rate becoming increasingly larger. A phase shift was also observed, as Δz_{max} decreased, which is attributed to a delay in the start-up transient of the simulation. The delay in start-up transient is caused by the speed of energy transported around the loop becoming reduced as a smaller maximum control volume size is selected. Thus, the subsequent changes in buoyancy and resulting hydraulic feedback is more delayed.

The assumptions of well mixed control volumes and unidirectional flow does not agree well with the experimentally observed convective plumes discussed in Chapter 6.2. The smaller the control volumes the more mixing is reduced. With less mixing the resulting hydraulic feedback along with the unidirectional flow creates a situation where unrealistic higher temperature slugs of fluid are created by the simulation. The higher temperature slugs affect the flow rate creating a simulated form of density wave oscillations. The theoretical density wave oscillations are also observed to interact constructively or destructively with the oscillations of the primary loop's theoretical models hydraulic and thermal response.

Convergence of the simulation is not found for either grid or time step size but rather a relationship exists between the simulation results and the chosen time step or grid size. Thus choosing the right grid and time step size may lead to a representative theoretical result however, ideally the solution should be independent of both grid and time step size. From the investigation performed on grid and time step independence, it is evident that the choice of time step size, as well as grid size, is not trivial. The problem of the model not converging can indicate that the approach followed in the development of the code is lacking. Due to this lack of convergence, if representative results are outputted by the model the same model will not necessarily give representative results when applied to cases of differing geometries or situations.

7.4.3 General observations

The theoretical simulation of the primary loop suffered from a number of short comings. A major shortcoming of the theoretical models program is that when

phase change takes place, violation of the CFL criteria takes place and the program is stopped. This rendered the program unable to simulate the two phase flow. The phase change causes water to be forced around the system through the expansion routine. This becomes problematic particularly as the phase change takes place in the larger control volume of the reactor and riser first. The amount of volume displaced is typically far larger than the smaller control volumes thus violating the CFL criteria.

The problem of expansion violating the CFL criteria can stem from the assumption of the calculated hydrostatic pressure as the working pressure of the cell. Describing the system as a hydrostatic pressure problem implies the pressure of a cell remains relatively constant and only changes according to the level in the expansion tank. Assuming a constant pressure allows for unrestrained expansion of the fluid provided sufficient energy input into a control volume. This, however, is not representative of reality as the pressure feedback caused by the expansion and its flow out of the primary loop and into the expansion line also restricts the expansion. The pressure feedback should ideally function by, reducing the pressure thus slowing the contraction of fluid and increasing the pressure thus reducing expansion of fluid. The theoretical model has no means of calculating this pressure feedback and incorporating its effects on the expansion/contraction of fluid in the loop. To calculate the pressure feedback may require analysis of time steps small enough to capture sonic phenomena such as pressure waves which is impractical.

The assumption of a one dimensional model with unidirectional flow is not representative of the observed reality. Complex three dimensional flows were observed during experimentation, particularly at start up, in the form of so-called convection plumes. The well mixed homogeneous model thus only partially captures these effects when larger control volumes are used.

The constant volumetric flow rate assumption is also flawed particularly when phase change takes place. The constant flow rate in the loop does not take the movement of fluid due to expansion/contraction into account and thus requires an additional expansion or contraction routine to be applied in parallel. This implies that the basic theory or approach used is unable to handle expansion/contraction correctly and requires revisiting. The expansion and contraction routine is required to ensure mass and energy are conserved. The expansion and contraction routine/approach used is flawed because, for smaller time steps numerical errors result in it failing to conserve energy.

The model is able to simulate single phase operation although it doesn't represent reality. It is able to run as a single phase operation does not have large changes in densities and subsequently large changes in expansion and contraction which violate the criteria. The problem with the single phase operation is that the results are strongly influenced by both the grid and time step size chosen. The program does however perform as expected for simple single phase operating instances giving expected results. As the program has been developed from scratch, other theoretical models and approaches can be

implemented using the basic frame work of the Fortran computer code.

8 Discussion and Conclusion

The importance of inherent safety in nuclear power systems has been the focus of much research and discussion since the recent disaster at Fukushima in Japan. However, even before the disaster, research trends in the nuclear field were already tending towards designing for inherent safety. In light of this, and with the Republic of South Africa looking to expand its nuclear profile, it is imperative that the skills and expertise gained during the expansion program are not lost. With this background in mind, the proposed concept of an inherently safe novel nuclear power system, a possible Generation IV+ type technology, has been investigated. Because of the multitude of topics to investigate and the plethora of available literature the scope was thus narrowed to focus on the flash-tube type primary cooling loop and secondary thermosyphon heat pipe type heat exchanging loop, shown in Figure 1.1.

The literature survey conducted briefly explained where the concept fits in with the current standing of nuclear reactors and previous research undertaken relating to a flash-tube and natural circulating systems. Most small and medium sized reactors (SMRs) are designed to be inherently safe with some having similar features to the proposed concept. A table summary of fourteen of theses SMRs was presented (Table 2.1.1) showing the country of origin and distinguishing features of each system.

The workings of thermosyphon loops and heat pipes are briefly discussed. Bhattacharyya *et al.* (2012) presents a substantial review of the recent advances in two-phase natural circulation loops. From this, natural circulating loop instabilities are then discussed with focus on two-phase static and dynamic instabilities. It was found that numerous instabilities can affect natural circulating loops with some manifesting large changes and even chaotic oscillation in circulation flow rates. Ultimately two-phase natural circulation loops operation is strongly influenced by the dynamic interactions of flow variables and feedback effects which, in turn, makes them complex to analyse.

The different methods of modelling two-phase flow are also discussed. The homogeneous model was found to be an important basic model used to develop two-phase flow system codes. The homogeneous model can be used as a basis for developing other separated flow models with no interface exchange such as the *Lockhart-Martinelli* Model, *Martinelli-Nelson* model and drift flux model, to better capture the nature of two-phase flow.

8.1 Primary Loop

As is evident from the literature survey, the nature of two-phase flow is inherently complex and a theoretical model has no validity until it is compared with experimental results. A small scale experimental set-up of the primary loop was built to which the secondary loop was later added.

8.1.1 Experimental set-up

The size and working temperatures of the primary loop were limited due to space and safety constraints. A maximum internal temperature of approximately 117 ℃ was recorded. The primary loop was designed with windows which proved indispensable in understanding the inner workings of the primary loop. Numerous observations were made with the most applicable of them being: flashing in the riser section; convective plumes; boiling and flashing from surface of the heating elements; steam space establishment and geysering discussed with pictures presented where possible.

The valve to the expansion line could be opened or closed to run the experiment in, so called, *heat pipe* mode. Along with the *heat pipe* two other modes of operation were defined for the primary namely: single (liquid) phase operation where all the fluid in the primary loop was in liquid phase, and two-phase operation where the presence of both the liquid and vapour states were observed in the primary loop. *Heat pipe* mode could only be achieved by closing the valve (in the expansion line) in a two-phase operational state as the pressure in the system would remain at the saturation pressure of the vapour, unlike single phase operation where the incompressible fluid's expansion would damage the experimental set-up and present a substantial safety risk if the expansion valve was closed.

The measurement and positioning of thermocouples and the orifice flow meter was done with care and extensive calibration tests were performed on the instrumentation system. Care was taken in ensuring that all heat flows could be accounted for and an energy/heat transfer account was performed. The heat extracted discrepancy due to thermocouple measurement in a worst case scenario was ±350 W which as a percentage of the power input, typically greater than 7.5 kW, is $\pm 350/7500 \approx 4.6\,\%$ which was considered acceptable.

The internal workings of a two-phase flow flash-tube type system are not often reported but the summary as presented by Bhattacharyya *et al.* (2012) gave valuable insight on the observations made. The ability to see inside did not only help with the understanding of the phenomena of natural circulation but also helped greatly with the control of the experiment.

The control of the experiment proved to be challenging, particularly as the water temperature in the expansion line and tank/pressuriser was much lower than the water temperature in the primary loop. The lower temperature water flowing back into the primary loop section, due to contraction/collapse of vapour, from the expansion line would stop the boiling in the primary loop. Furthermore, the amount of heat extracted by the secondary loop was difficult to control. The sensitivity of the size of the steam space to the secondary loops heat extraction rate resulted in establishing a constant size steam space proving to be difficult. It was observed that the steam space would collapse rapidly, if a little too much heat was removed. This would in turn stop the boiling process as lower temperature water was drawn in from the expansion line. The transient behaviour of the boiling and slow response to power input

increases, due to the thermal inertia of the water, also compounded control problems.

The observation windows allowed for the problems of the heating element power density to be identified and addressed. The window gaskets, it was observed, provided nucleation sites from which boiling/flashing could take place. Boiling in the primary loop was highly transient and aggressive geysering was observed which shook the entire apparatus. A link was made between the flow rate response of the system and the level of the water/steam interface in the steam drum. Understanding of the flow rate response of the system was also enhanced due to the windows. The results obtained from the orifice flow meter, though inaccurate around near zero flow rates, provided good resolution of the flow transients and was able to capture the transients during two-phase flow operation.

The flow rate response of the primary loop for different power inputs was well captured by the orifice flow meter. The start-up data can be used to validate the results of a theoretical model simulation of the primary loop. The start-up of the primary loop and subsequent plume formation which was observed was useful in understanding inner workings of the primary loop with the plumes transporting energy and mixing the flow. The experiment provided invaluable insight into the workings of two-phase flow as well as single phase natural circulation systems.

8.1.2 Theoretical model

A simple homogeneous model of the primary loop was developed based on equations derived from the conservation of mass, momentum and energy principles found in section 3.2. A computer program was written in Fortran 90 to simulate the primary loop using the developed algorithm and the homogeneous model. The program incorporated a number of features such as axial conduction, specifiable control volume sizes, a complex heat loss model for heat losses to the environment, dynamic time stepping and the ability to import and use test results for the initialisation of properties of the primary loop. Furthermore, a scheme was developed to handle the expansion and contraction mass within the control volumes, moving it into the expansion line in an attempt to preserve the conservation of mass within the system. Although the computer program may have incorporated less important phenomena, such as axial conduction, it was written with the purpose to be developed further, providing the base framework on which further research could be based.

When the primary loop theoretical model encountered the onset of two-phase flow, the expansion/contraction resulted in the Courant-Friedrichs-Lewy (CFL) condition being violated, which triggered the stopping of the program - this is in contrast to Ruppersberg's (2008) and Sittmann's (2011) loops. The violation of the CFL condition is caused by the rapid formation and collapse of the vapour phase and the large size differences between control volumes. The sizes of the primary loops control volumes varied greatly compared to relatively

constant sizes used by Ruppersberg (2008) and Sittmann (2011). The large differences between the vapour and fluid densities aggravated the problem with expansion and contraction as a small mass phase change resulted in a large volumetric change.

The assumption of a constant hydrostatic pressure also compounded problems as the pressure feedback of resulting expansions and contractions was not communicated within the model. This effectively resulted in a case where expansion and contraction was dependent solely on the hydrostatic pressure and energy contained by the mass in the control volume. The developed expansion scheme may also contribute to the problem as the direction of expansion is singular and dependent on flow rate instead of the path of least friction.

The program was tested for specific basic case test scenarios to which the expected outcome could be logically deduced without need for simulation. These basic test case included: giving the primary loop a starting forward and reverse flow with no power input; starting from zero flow rate in the primary loop with heat input of 50 %, 100 % and 150 % of 7668.6 W distributed in the reactor and riser control volumes; starting from zero flow rate in the primary loop with heat input of (7668.6 W) distributed in the down-comer control volumes. The theoretical simulation's general response for these situations was as anticipated. Oscillations in the flow rates were observed for the simulated single phase operation and attributed to the response of the theoretical model.

The primary loop's theoretical model was compared to experimental results, investigating the effect of both time step and control volume size. It was found that the results varied greatly, not necessarily tending towards a more representative result the smaller the time step or control volume size chosen. This alluded to a more fundamental problem with the solution algorithm/method. The assumption of one dimensional model with a unidirectional flow is not representative of the experimentally observed reality. The constant volumetric flow assumption and its implementation, not considering the effects of expansion and contraction, is also noted to be flawed particularly when phase change takes place.

Although the theoretical model ultimately failed in representatively simulating the primary loop the basic framework of the Fortran computer code has been developed. This dynamic time stepping computer program complete with property, heat transfer and friction functions as well as discretized geometric model of the experimental set-up can be used as a basis for further research and implementation of alternative solution algorithms and models.

8.2 Secondary Loop

The secondary heat exchanger, consisting of two heat pipe loops, was built and connected to the primary loop once the tests on the primary loop on its own was completed. The theoretical model for the secondary loop was developed and compared using the experimental test results.

8.2.1 Experimental set-up

The tests conducted on the primary and secondary loop experimental set-up, as a unit, provided the results that were used for the comparison and development of the theoretical thermal-hydraulic model of the secondary heat exchanger and the primary loop. From experimental observations made, three different states of operation were found for the secondary loop's evaporator's exterior, namely; liquid, condensing and two-phase regimes, which complicated the theoretical model. A limiting factor of testing the secondary loop on the primary loop was that the primary loop's working temperature remained relatively constant during two-phase operation. The secondary loop could only be tested at the saturation temperature of the fluid in the primary loop during two-phase and condensing regimes. The data and correlation obtained is thus for a limited temperature range.

Only one of the two heat pipes from the secondary loop was required to transfer sufficient heat from the primary loop. The heat pipe with the best construction, closest matching the design, was selected to extract the heat. The start-up transient of the secondary loop was investigated. The onset of heat transfer was found to occur at temperatures greater than 60 °C, for the evaporator's exterior.

8.2.2 Theoretical model

A thermal resistance model approach was chosen in order to theoretically model the secondary loop heat exchanger. It provided a means of working out the internal temperatures of the heat pipe loop. The internal thermal resistance of the secondary loop was assumed to be negligent. This implied that the internal temperature of the evaporator and condenser were the same. The thermal inertia of the working fluid was not considered.

The geometry of the heat exchanger was unique, with a multi-pass cooling water stream and single pass but multi-tube condenser and manifold supplied inclined multi-tube evaporator, located at the top of steam drum. This unique physical configuration made it difficult to find applicable theory to use in modelling the thermal resistances. This is as the physical configurations of the evaporator and condenser are unique situations and orientations. Thus, values required for the heat transfer coefficients were found semi-empirically using experimental results.

Standard forms of heat transfer equations found in literature were used and in some cases required further modification such as the external Nusselt number for the cooling water side of the condenser. This approach, though functional, is limited in applicability to the operational points from which data was used to derive the models, as is the case in many heat transfer applications.

The correlation of the external waterside Nusselt number for the condenser section of the secondary loop worked well. The incorporation of the inlet and exit Prandtl numbers with the general proposed form of the Nusselt number for cross flow over tube banks gave an extremely good prediction of the exper-

imentally obtained Nusselt numbers. An acceptable regression was obtained with the R-squared value of 0.9999.

The chosen thermal resistances used in the model failed to model the operation of the heat exchanger for the evaporator's exterior operating in the liquid regime. The simple natural convection thermal resistance assumed for the evaporator's exterior along with the experimentally correlated internal thermal resistances were not effective in representing the liquid regime response. Thus, the liquid regime operation was modelled using the effectiveness-NTU approach. A linear piecewise function dependent on the temperature difference between the fluid surrounding the evaporators exterior and the average cooling water temperature was developed to approximate the overall heat transfer coefficient for the entire heat pipe. The model for the liquid regime showed good correlation to experimental results except for low heat transfer rates, particularly those below 300 W. This is expected as thermocouple measurement error is expected to be up to ± 350 W in the worst case scenario. The model for the liquid regime was incorporated into the theoretical model of the primary loop.

A program was written to simulate the secondary loop, utilising the theoretical thermal resistance model developed, which was solved iteratively by checking for an energy balance. The program required only three inputs, the inlet temperature of the cooling water, the temperature of the fluid surrounding the evaporator and the mass flow rate of the cooling water supplied to the condenser. The computer program solution algorithm sometimes led to divergent values depending on assumed initial values. This was attributed to the sensitivity of the model's response, particularly when one thermal resistance in the model was not dominant. Thus, the program utilized approximations from the effectiveness-NTU approach, from Appendix F, for initial values. The secondary loop's theoretical model's results, when compared with experimental results, correlated well with the condensing regime, however, not as well for the two-phase regime. The simplistic approach used ignored the effect of extremely complex flow regimes surrounding the evaporator during two phase flow conditions. With the chaotic flow of effectively constant in temperature vapour bubbles and liquid during all the experimental tests the poor performance of the two-phase regime model is expected.

A sensitivity analysis was performed on the secondary loops theoretical model. The findings of the analysis was that the evaporator's section was oversized while the condenser section was undersized. The secondary loop's theoretical model's sensitivity to the external temperature of the evaporator is also evident. This suggests that the model's individual correlated thermal resistances are only applicable for the limited range from which the correlations were performed. Further testing with a wider range of external temperatures is required to develop a robust and representative model of the secondary loop for a multitude of working conditions.

The secondary loop's theoretical model, developed in this thesis, is limited in its range of application. The limitation stems from the set of results,

with which the semi-empirical characterisation was done, coming from tests with relatively equal saturation temperatures and pressures. Subsequently the model should not be used for prediction of performance outside the experimentally tested range. A more fundamental understanding of boiling/condensation dependencies on surface and fluid combinations, internal pressures and heat fluxes will help in obtaining a better understanding of two-phase phenomena found inside the secondary loop.

8.3 Closing Statement

Theoretical and experimental models of the primary and secondary loops were developed/built, tested and compared. As with the investigation of any new concept, the first step has been taken and many lessons have been learned. The goal and objective of an inherently safe nuclear power system warrant the continuation and further research of the concept. Suggestions for the path forward in researching the concept and building on the work presented in this thesis is discussed in the next chapter, Chapter 9.

9 Recommendations

Recommendations are made pertaining to the continuation of the work done so far. Because the concept being investigated is new, many mistakes had to be corrected by trial and error and many unforeseen difficulties, that were not possible to anticipate at the outset, presented themselves. This research could possibly assist others, who are further researching the concept in question, in avoiding similar pitfalls. The recommendations made here have been subdivided according to the respective sections to which they are applicable.

9.1 Experimental Set-Up

The following recommendations, with respect to the experimental set-up, are made:

- The glass tubes, making up the down-comer, should be replaced with more robust tubes (stainless steel) and stronger mechanical seals should be used in order to lower the risk of one of the down-comer tubes or connections failing and endangering the operator.
- The geometry of the experimental set-up should be revisited, particularly the shape of the riser. The shape can possibly be revised to represent the conical *adiabatic* diffuser as referred to by Yadigaroglu and Zeller (1994). Thereby reducing the effect of the relatively fast flashing of the dense liquid into a less dense vapour.
- Accurate scaling of the system must be done in order to establish similarity relations between prototype and model for further understanding of the full size concept. This will most likely require a full redesign of the experimental apparatus such that it can handle much higher temperatures and pressures.
- The size and design of the steam drum and riser portion which protrudes into the steam drum, can be investigated with the goal of a possible reduction in oscillations of flow.
- A heat source more representative of the nuclear core, in terms of frictional pressure drop and heating element's power flux density, should be investigated with the primary goal of reducing bubble formation in the reactor and sub cooled boiling.
- Notwithstanding the above recommendations the tertiary natural circulating air cooled heat exchanger can be connected to the secondary loop to investigate the thermal response of the entire system.
- Differing methods of measuring flow rate should be used in parallel with the orifice flow meter allowing for comparison of the accuracy of the flow measurement results. Ideally non/minimally invasive methods such as electromagnetic, ultrasonic and Coriolis flow meters should be incorporated.
- Additional flow meters should be placed such that the flow rates of the expansion line and down-comer can be measured. This is done so that the effect of expansion and subsequent mass transport in and out of the primary

loop can be recorded. These flow rates will provide valuable data to which theoretical simulations can be validated as well as provide insight into the mass transfer within the system.

- The flow of water into and out of the expansion line had an unexpectedly large effect on the system. The following revisions are thus suggested:
  + The expansion tank's design should be a closed system with a specifiable internal pressure.
  + The expansion tank and line should be well insulated to minimize heat losses.
  + The temperature profile along and thermal response of the expansion line and tank should be measured.
  + Differing expansion line connections to the primary loop should be investigated.
- A pressurizer with the ability to control the pressure of the system will help the control of the system. The problem had is to design a passive system requiring no sensors and electromechanical feedback control. Furthermore, the pressurizer, with its own heat input, could be designed to have dual uses. It could be used as the pressurizer of the primary loop or operate as a steam drum to which the secondary loop could be attached. The secondary loop's heat transfer capabilities could then be measured with much greater accuracy and over a larger range of temperatures. The steam drum could also be used as the preliminary heat source for the secondary loop for the testing of the tertiary air heat exchanging loop before its attachment to the primary loop.
- The secondary loop should be retested under different conditions to those found during experimentation for a better characterisation of its performance. Testing of the secondary loop using the primary loop made it difficult to quantify the energy extracted by the secondary loop's evaporator and limited the temperature range to which the evaporator was exposed. It is recommended that the secondary loop be attached to a liquid/vapour heat source where the internal temperature can be controlled. This would provide a platform from which a number of variables can be investigated, such as:
  + the amount of liquid charge
  + angle of condenser tube
  + external temperature of the evaporator
  + a larger range of mass flow rates and heat exchanging rates.

  It will also allow for a better energy balance and an overall, more accurate correlation to be performed possibly using discussed forms of the equations.

9.2 Modelling of Secondary Loop

It is recommended for future work that although the evaporator operates in three heating regimes (liquid, two-phase and condensation (vapour-only)) the condensation regime should be the focus of further research. The fact that the liquid and two-phase regimes are very specific to the evaporator's configuration

in the loop, further work on this will most likely be limited in its application.

Furthermore it is recommended that:

- The characteristic behaviour of the secondary loop should be investigated and possibly be modelled by attempting to model the physical internal workings of the secondary loop, instead of utilising a simple thermal resistance model. By doing this the nature of the heat pipe's thermal-physical response can be better captured, which is critical if implemented in nuclear power systems.
- The semi-empirically calculated thermal resistances could be found for a larger range of working conditions. This will result in more robust and representative equations and computer simulation.

9.3 Modelling of Primary Loop

As the failure of the developed model of the primary loop's ability to handle two-phase flow is evident as discussed in section 7.4, the following recommendations are made:

- Conduct a thorough literature review of techniques used to model two-phase flow for more complex two-phase flow models, compared to the homogeneous model. Identify how commercial codes deal with two-phase flow for further possible insight.
- Do not use the simplifying assumption of a solely hydrostatic pressure problem. The dynamic effects and resulting pressure feedback of expansion and contraction of the vapour should be incorporated.
- Do not assume a constant volumetric flow rate.
- Using the framework code developed in this thesis, as a base, implement the separated flow model and see if it captures the two-phase phenomena.
- Incorporate the transient effects of the neutronics of the system by coupling the thermal-hydraulic simulation to a neutronics model.
- Investigate and create an algorithm independent of time step and control volume size.
- Investigate a model able to incorporate the expansion of fluid and its movement into and out of the expansion line, utilising the path of least frictional resistance dividing the flow proportionally between the two paths.
- Experimentally investigate plume formation and its effects in both single phase and two-phase flow states. This can possibly also be done with the aid of commercial CFD giving the ability to quantify the mixing and entrainment effects.
- Investigate capability of commercial computational thermo-fluid dynamic software packages to simulate the presented problem.

List of References

Aritomi, M., Chian, J.H., Nakahashi, T., Wataru, M. and Mori, M. (1992). Fundamental study on thermo-hydraulics during start-up in natural circulation boiling water reactors, (i). *Journal of Nuclear Science and Technology*, vol. 29, no. 7, pp. 631–641.

Aritomi, M., Chiang, J.H. and Mori, M. (1993). Geysering in parallel boiling channels. *Nuclear Engineering and Design*, vol. 141, no. 1-2, pp. 111 – 121. ISSN 0029-5493.

ASME (2003). *Measurement of fluid flow using small bore precision orifice meters*. New York : American Society of Mechanical Engineers, New York.

Batty, J. and Folkman, S. (1983). *Food engineering fundamentals*. Wiley. ISBN 9780471056942.

Bhattacharyya, S., Basu, D.N. and Das, P.K. (2012). Two-phase natural circulation loops: A review of the recent advances. *Heat Transfer Engineering*, vol. 33, no. 4-5, pp. 461–482.

Boure, J., Bergles, A. and Tong, L. (1973). Review of two-phase flow instability. *Nuclear Engineering and Design*, vol. 25, no. 2, pp. 165 – 192. ISSN 0029-5493.

Çengel, Y. and Cimbala, J. (2006). *Fluid Mechanics: Fundamentals and Applications, Si Version*. McGraw-Hill series in mechanical engineering. McGraw-Hill Higher Education. ISBN 9780071257640.

Çengel, Y., Ghajar, A. and Kanoğlu, M. (2011). *Heat and Mass Transfer: Fundamentals and Applications*. McGraw Hill Higher Education. ISBN 9780071311120.

Chiang, J.-H., Aritomi, M., Inoue, R. and Mori, M. (1994). Thermo-hydraulics during start-up in natural circulation boiling water reactors. *Nuclear Engineering and Design*, vol. 146, no. 1-3, pp. 241–252. ISSN 0029-5493.

Clausse, A. and Lahey Jr, R.T. (1991). The analysis of periodic and strange attractors during density-wave oscillations in boiling flows. *Chaos, Solitons & Fractals*, vol. 1, no. 2, pp. 167–178.

Courant, R., Friedrichs, K. and Lewy, H. (1928). Über die partiellen differenzengleichungen der mathematischen physik. *Mathematische Annalen*, vol. 100, pp. 32–74.

Dobson, R. (1993). Transient response of a closed loop thermosyphon. *R&D Jornal*, vol. 9.

Dobson, R. (2012). Relative thermal performance of supercritical CO_2, H_2O, N_2, and He charged closed-loop thermosyphon-type heat pipes. *Heat Pipe Science and Technology, An International Journal*, vol. 3, no. 2-4, pp. 169–185. ISSN 2151-7975.

Faghri, A. (1995). *Heat Pipe Science and Technology*. Mechanical Engineering. Taylor & Francis Group. ISBN 9781560323839.

Fukuda, K. and Kobori, T. (1979). Classification of two-phase flow instability by density wave oscillation model. *Journal of Nuclear Science and Technology*, vol. 16, no. 2, pp. 95–108.

Furutera, M. (1986). Validity of homogeneous flow model for instability analysis. *Nuclear Engineering and Design*, vol. 95, no. 0, pp. 65 – 77. ISSN 0029-5493.

Furuya, M., Inada, F. and van der Hagen, T. (2005). Flashing-induced density wave oscillations in a natural circulation BWR-mechanism of instability and stability map. *Nuclear Engineering and Design*, vol. 235, no. 15, pp. 1557 – 1569. ISSN 0029-5493.

Generation IV International Forum and U.S. DOE Nuclear Energy Research Advisory Committee (2002 December). A technology roadmap for generation IV nuclear energy systems. Tech. Rep., U.S. DOE Nuclear Energy Research Advisory Committee; The Generation IV International Forum.

HOLTEC International (2013 November). Smr-featured technology & design: Safe & secure. Website: Accessed on [2013.11.17].
Available at: `http://www.smrllc.com/safety.html`

IAEA (2012 September). Status of small and medium sized reactor design: A supplement to the IAEA advanced reactor information systems (ARIS). Supplement, International Atomic Energy Agency.

IAEA Director General (2013 July). Nuclear technology review 2013. Annual Report 57, International Atomic Energy Agency.

Kew, P. and Reay, D. (2006). *Heat Pipes, Fifth Edition: Theory, Design and Applications*. Butterworth-Heinemann. ISBN 0750667540.

King, C. (1964). *Nuclear Power Systems: An Introductory Text*. Macmillan.

Knovel (2006). *Knovel Steam Tables*. Electronic. Electronic tables: Accessed on [2012.03.06].
Available at: `http://app.knovel.com/hotlink/toc/id:kpKST00001/knovel-steam-tables`

Lee, J., Rhi, S., Kim, C. and Lee, Y. (2003). Use of two-phase loop thermosyphons for thermoelectric refrigeration: experiment and analysis. *Applied Thermal Engineering*, vol. 23, no. 9, pp. 1167 – 1176. ISSN 1359-4311.

Levy, S. (1999). *Two-phase flow in complex systems*. Wiley & Sons.

Manera, A., Prasser, H.-M., Lucas, D. and van der Hagen, T. (2006). Three-dimensional flow pattern visualization and bubble size distributions in stationary and transient upward flashing flow. *International Journal of Multiphase Flow*, vol. 32, no. 8, pp. 996 – 1016. ISSN 0301-9322.

Nayak, A., Vijayan, P., Jain, V., Saha, D. and Sinha, R. (2003). Study on the flow-pattern-transition instability in a natural circulation heavy water moderated boiling light water cooled reactor. *Nuclear Engineering and Design*, vol. 225, no. 2-3, pp. 159 – 172. ISSN 0029-5493.

Paniagua, J., Rohatgi, U. and Prasad, V. (1999). Modeling of thermal hydraulic instabilities in single heated channel loop during startup transients. *Nuclear Engineering and Design*, vol. 193, no. 1-2, pp. 207 – 226. ISSN 0029-5493.

Papini, D. and Cammi, A. (2010). Modelling of heat transfer phenomena for vertical and horizontal configurations of in-pool condensers and comparison with experimental findings. *Science and Technology of Nuclear Installations*, vol. 2010.

Pioro, I. (1998). Experimental evaluation of constants for the Rohsenow pool boiling correlation. *International Journal of Heat and Mass Transfer*, vol. 42, no. 11, pp. 2003 – 2013. ISSN 0017-9310.

Pioro, L. and Pioro, I. (1997). *Industrial Two-phase Thermosyphons*. Begell House. ISBN 9781567000641.

Republic of South Africa Department of Energy (2010 October). Integrated resource plan for electricity. Draft Report Revision 2, Republic of South Africa Department of Energy.

Reyes, J.J. (2005 November). Natural circulation in water cooled nuclear power plants, annex 6: Governing equations in two-phase fluid natural circulation flows. Tech. Rep. IAEA-TECDOC-1474, International Atomic Energy Agency, Vienna, Austria.

Ruppersberg, J. (2008 March). *Transient modelling of a loop thermosyphon. MSc Thesis*, University of Stellenbosch, Stellenbosch.

Senda, F. (2012 March). *Aspects of waste heat recovery and utilisation (WHR&U) in pebble bed modular reactor (PBMR) technology. MSc Thesis*, University of Stellenbosch, Stellenbosch.

Sittmann, I. (2011 March). *Inside-pipe heat transfer coefficient characterisation of a one third height scale model of a natural circulation loop suitable for a reactor cavity cooling system of the pebble bed modular reactor. MSc Thesis*, University of Stellenbosch, Stellenbosch.

STL (2011). The th-100 power plant. Steenkampskraal Thorium Limited (STL), Website: Accessed on [2014.03.22].
Available at: `http://www.thorium100.com/stl_oct_2012_011.htm`

Tan, J. and Liu, C. (1990). Predicting the performance of a heat-pipe heat exchanger, using the effectiveness-{NTU} method. *International Journal of Heat and Fluid Flow*, vol. 11, no. 4, pp. 376 – 379. ISSN 0142-727X.

Tanihira, I. and Shimazu, Y. (2007). Small PWR using coated particle fuel of thorium and plutonium. *Journal of Nuclear Science and Technology*, vol. 44, no. 8, pp. 1045–1051.

Vasiliev, L.L. (2005). Heat pipes in modern heat exchangers. *Applied Thermal Engineering*, vol. 25, no. 1, pp. 1 – 19. ISSN 1359-4311.

Vecsey, G. and Doroszlai, P. (1988). Geyser, a simple, new heating reactor of high inherent safety. *Nuclear Engineering and Design*, vol. 109, no. 1-2, pp. 141–145. ISSN 0029-5493.

Versteeg, H. and Malalasekera, W. (2007). *An Introduction to Computational Fluid Dynamics: The Finite Volume Method*. Pearson Education Limited. ISBN 9780131274983.

Verwey, A. (2010 March). *Modelling of a passive reactor cavity cooling cystem (RCCS) for a nuclear reactor core subject to environmental changes and the optimisation of the RCCS radiation heat shield. MSc Thesis*, University of Stellenbosch, Stellenbosch.

Wahl, C. (2012 October). Flashtube-type natural circulation cooling system for a nuclear reactor. *Final-Year Project*, Stellenbosch University, Stellenbosch.

Whalley, P. (1987). *Boiling, Condensation, and Gas-Liquid Flow*. Clarendon Press Oxford.

Wissler, E.H., Isbin, H.S. and Amundson, N.R. (1956). Oscillatory behaviour of a two-phase natural-circulation loop. *AIChE Journal*, vol. 2, no. 2, pp. 157–162. ISSN 1547-5905.

Yadigaroglu, G. and Zeller, M. (1994). Fluid-to-fluid scaling for a gravity- and flashing-driven natural circulation loop. *Nuclear Engineering and Design*, vol. 151, no. 1, pp. 49 – 64. ISSN 0029-5493.

Appendices

A. Theoretical Heat Loss Model for the Primary Loop and Experimental Set-Up

This appendix deals with the formulation of the theoretical thermal resistance model for the primary loop's heat losses to the environment. The model was implemented in Fortran 90 to be used by the theoretical model of the primary loop as outlined in Chapter 3. The heat loss model was also used to quantify the heat loss from the experimental set-up when operated. These values for the experimental set-up were then used when performing an energy balance on the system and conclusions were drawn about the validity of the heat loss theoretical model. The process of this heat loss characterisation for the experimental set-up is also discussed in this appendix.

The heat losses for the system were calculated using simple thermal resistance models, as shown in Figure A.1, applied to control volumes as mentioned in Chapter 3. The thermal inertia, of the insulation and metal, was ignored. This was done as using an explicit solution method would require the mesh Fourier number to be smaller than $\tau < 0.5$ (Çengel *et al.*, 2011). This in turn would either result in incredibly small time steps or unrealistically sized control volumes.

A.1 Assumptions

Due to the complexity of the physical shape of the experiment as well as the heat transfer phenomena taking place, a number of simplifying assumptions were required in order to model the heat losses of the primary loop. The heat loss model chosen has the following simplifying assumptions:

- All the heat losses are transferred to the air surrounding the experiment.
- The driving heat transfer forces at the boundaries are through convection only.
- Conduction is limited to the solid walls and insulation.
- All control volumes' thermal resistances, and thus heat losses, can be described by a diagram in Figure A.1.
- All areas can be approximated as a flat plate or a tube, thus all irregularities are ignored such as flanges.
- The flow is assumed to be fully developed.
- The heat transfer due to radiation is negligible.
- Effect of windows on thermal resistance is ignored.
- The thermal resistance from the water to the top of the steam drum and bottom of the reactor is not dominating and is approximated as zero.

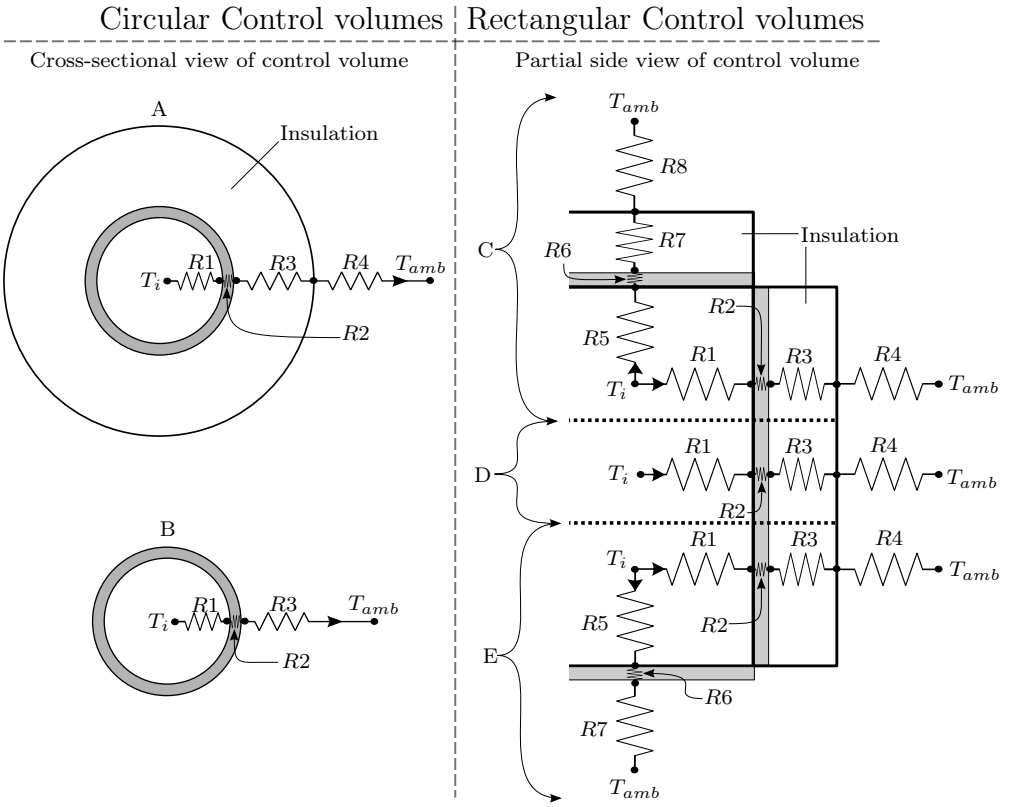

Figure A.1: Thermal resistance diagrams for circular and rectangular shaped cross-sectional control volumes for heat flow between the fluid at T_i and the environment at T_{amb}

A.2 Applicable Theory

All convection heat transfer coefficients, h, are calculated from their respective Nusselt number through

$$h = \frac{Nuk}{L_c} \tag{A.1}$$

where L_c is a characteristic length in the case of tubes $L_c = D_h$ and k thermal conductivity of the fluid at the film temperature. The thermal resistance can then be calculated using

$$R = \frac{1}{hA_s} \tag{A.2}$$

where A_s is the area where the heat transfer coefficient is acting. The overall thermal resistance for heat flow paths A, B and D in Figure A.1 is found using

$$R_{tot} = \sum_{i=1}^{n} R_i \tag{A.3}$$

but for heat flow paths C and E

$$R_{tot} = \left(\frac{1}{\sum_{i=1}^{4} R_i} + \frac{1}{\sum_{i=5}^{n} R_i} \right)^{-1} \tag{A.4}$$

When the overall thermal resistance, R_{tot}, is calculated the heat transfer is then simply

$$\dot{Q}_{out} = \frac{T_i - T_{amb}}{R_{tot}} \tag{A.5}$$

with T_i and T_{amb} denoting the internal temperature of the control volume and the ambient temperature in the lab respectively as seen in Figure A.1.

A.2.1 Internal Nusselt numbers and heat transfer coefficients

The internal Nusselt numbers, using Çengel *et al.* (2011), were calculated for laminar fully developed flow in tubes ($Re \leq 2300$),

$$Nu = 3.66 \tag{A.6}$$

and for turbulent flow using Gnielinki's equation, found in Çengel *et al.* (2011),

$$Nu = \frac{(f/8)(Re - 1000)Pr}{1 + 12.7(f/8)^{0.5}(Pr^{2/3} - 1)} \tag{A.7}$$

where $3 \times 10^3 Re \leq 5 \times 10^6$, $0.5 \leq Pr \leq 2000$ and $f = (0.790ln(Re) - 1.64)^{-2}$.

A.2.2 External Nusselt numbers

The outer surfaces of the experiment were exposed to the still air in the laboratory. With no forced convection, only natural convection was used to model the external surface heat transfer coefficient. The majority of equations use the Rayleigh Number defined as

$$Ra_L = \frac{g\beta(T_s - T_\infty)L_c^3}{(\mu/\rho)^2} Pr \tag{A.8}$$

The following external Nusselt numbers, used in equation A.1 to find h_{out}, for the different geometries and orientations where used, coming from Çengel *et al.* (2011):

- Vertical flat plate or cylinder where L_c is the vertical length

$$Nu = \left\{ 0.825 + \frac{0.387 Ra_L^{1/6}}{\left[1 + (0.492/Pr)^{9/16}\right]^{8/27}} \right\}^2 \tag{A.9}$$

- Horizontal cylinder where $L_c = D$

$$Nu = \left\{ 0.6 + \frac{0.387 Ra_L^{1/6}}{\left[1 + (0.559/Pr)^{9/16}\right]^{8/27}} \right\}^2 \tag{A.10}$$

- Horizontal flat plate with lower heat transfer surface where $L_c = A_s/\wp$

$$Nu = 0.27Ra_L^{1/4} \tag{A.11}$$

- Horizontal flat plate with upper heat transfer surface where $L_c = A_s/\wp$ if $Ra_L < 10^7$

$$Nu = 0.54Ra_L^{1/4} \tag{A.12}$$

else

$$Nu = 0.15Ra_L^{1/3} \tag{A.13}$$

A.2.3 Wall conduction heat transfer resistances

The basic steady heat conduction formulas of

$$R_w = \frac{\delta_w}{kA} \tag{A.14}$$

for steady heat conduction through a flat wall of thickness δ_w, and

$$R_{cyl} = \frac{ln(r_2/r_1)}{2\pi Lk} \tag{A.15}$$

for conduction through a tube wall, where r_1 and r_2 are the inside and outside radius's of the tube respectively and L is the length of the tube, were used to model the thermal resistance of the insulation and walls of the experiment.

A.3 Zone Thermal Resistances Implementation

With the variation in shape as well as the insulation of the experimental set-up it was found easiest to deal with the thermal resistances according to their respective zones, as shown in Figure 3.4. The thermal resistances models used for the control volumes are all found in Figure A.1. The choice of model is stated for each zone section with the applicable equation/heat transfer coefficient used to find each resistance.

For vertical external surfaces the average surface temperature was calculated and used to calculate the average external heat transfer coefficient, h_{out}, using the entire length for L_c. The average heat transfer coefficient was then used in the calculation of the thermal resistances.

The average heat transfer coefficient for the external sides, h_{out}, is calculated using equation A.9 or equation A.10 for each respective vertical and horizontal section flat wall or tube. The thermal resistance model of the zones, as seen in Figure 3.4, is broken up as follows:

- Zone 1.1 - Model: E Figure A.1
- Zone 1.2/1.3 - Model: D Figure A.1
- Zone 2.1 - Model: A Figure A.1
- Zone 2.2 - Model: No heat transfer, $\dot{Q}_{out}$=0 [W]
- Zone 3.1 - Model: C Figure A.1
- Zone 3.2 - Model: D Figure A.1

- Zone 4.1 - Model: A Figure A.1
  Vertical orientation with glass tube and insulation
- Zone 4.2/4.4 - Model: B Figure A.1
  Horizontal orientation with glass tube
- Zone 4.3 - Model: B Figure A.1
  Vertical orientation with glass tube
- Zone 4.5/4.8 - Model: B Figure A.1
  Vertical orientation with stainless steel tube
- Zone 4.6/4.7 - Model: B Figure A.1
  Horizontal orientation with stainless steel tube
- Zone 5.1/5.3 - Model: B Figure A.1
  Horizontal orientation with rubber tube
- Zone 5.2 - Model: B Figure A.1
  Vertical orientation with rubber tube
- Zone 5.4 - Model: B Figure A.1
  Vertical orientation with plastic tank

where the thermal resistances are: $R1$-internal forced convection with Nusselt number from equation A.6 or A.7; $R2$ and $R6$-resistance of the wall or tube using equation A.14 or equation A.15 respectively; $R3$-resistance of insulation, equation A.14, or in the case of no insulation external natural convection to air found using h_{out}; $R4$-external natural convection to air found using h_{out} and appropriate external Nusselt number; $R5$-simplified as zero thermal resistance by assumption; $R7$- in model E is external natural convection to air found using Nusselt number from equation A.11 while in model C it is resistance of insulation, equation A.14; $R8$-external natural convection to air found using Nusselt number from equations A.12 or A.13.

A.4 Experimental Set-Up Heat Loss Theoretical Characterisation

The theoretical heat loss model of the primary loop was used to characterise the heat losses from the experimental set-up. Six different test runs, tests 4-9 of test batch 3, were used giving 9810 different data points to use as inputs for the Fortran 90 program that solved for the theoretical heat loss. The theoretical model was only used to calculate the heat loss of the primary loop, Zones 1-4, and not that of the expansion line, zone 5, as no data was available for zone 5.

The Fortran 90 program took the values from the experimental results and overlaid it on the theoretical model. The temperatures were simply linearly interpolated between control volumes corresponding to the thermocouple probe positions. Thus all the temperatures were approximated around the loop. The velocity of the fluid in the loop is required to calculate the internal heat transfer coefficients, thus, the flow rate as measured at the orifice plate was also given to the theoretical model.

The program then went about solving the thermal resistance diagrams for

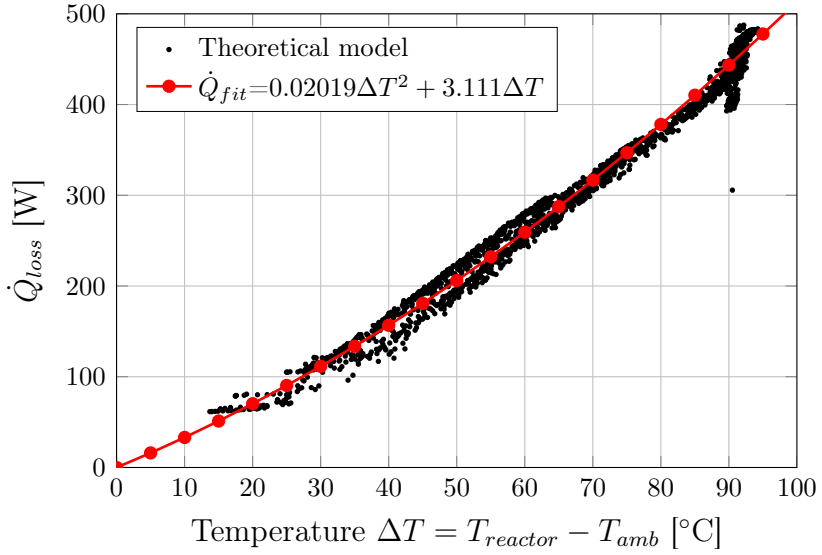

Figure A.2: Theoretical heat loss model results showing $\dot{Q}_{loss}$ calculated using experimental results from tests 4-9 of test batch 3 as inputs, with overlaid curve fit used in post-processing purposes

the different control volumes and the heat transfer, $\dot{Q}_{loss}$. The program iterated until the $\dot{Q}_{loss}$ value remained the same. The program would then move onto the next data point with every 5th data point result shown in Figure A.2.

The results' post-processing of the experimental data took place in Matlab® while the theoretical model ran in Fortran 90. A simple way of calculating the heat loss using any experimental point, without any iteration in Matlab® was required. The temperature difference between temperature measured by the thermocouple probe at the reactors exit, $T_{reactor}$, and the ambient temperature, T_{amb}, showed a near linear relationship to the heat loss predicted by the theoretical heat loss model. Thus, a curve fit of the data using a quadratic polynomial, which was forced through [0,0], gave

$$\dot{Q}_{loss} = 0.02019\Delta T^2 + 3.111\Delta T \tag{A.16}$$

where ΔT=$T_{reactor} - T_{amb}$ with $T_{reactor}$. Figure A.2 shows this curve fit overlaid on the results. Equation A.16 was then used in Matlab® during the post-processing of results and to perform an energy balance on the system.

B. Primary Loop Solution Algorithms, Functions, Subroutines and Results

The primary loop's solution algorithms, functions, subroutines and results are discussed in this appendix. Firstly the thermophysical property functions are briefly discussed giving the references used for the property fits. Secondly, the expansion procedure implemented and thirdly the *time loop* subroutine used for the primary loop's solution algorithm are discussed. The expansion procedure's objective is to help ensure the conservation of mass within the primary loop. The *time loop* subroutine explains the steps used by the primary loop's solution algorithm to solve the primary loop. The *primary loop contents* and the *Expansion line contents* subroutines, used by the *time loop* subroutine, give the detailed steps and executions of the conservation of mass, momentum and energy equations. Fourthly, the general operation and response of the program to specific instances with predictable outcomes is presented. Lastly the grid and time step size of the primary loop computer program are investigated.

B.1 Thermophysical Properties

The thermophysical property functions or constants of the materials and fluids used in the simulation of the primary loop were also used for the secondary loop. When properties were required to be curve fitted they were declared as functions. Each function in the written code was accompanied, in comments, by: the functions input and outputs units; the model's statistical data in the form of the sum of the squared errors (SSE), R-square and root-mean-square error; and the functions range of applicability.

As XSteam, mentioned in Appendix C.2, was not available for Fortran 90 the properties of water were extracted from Knovel steam tables, (Knovel, 2006) or from Çengel *et al.* (2011) to which the curve fits were applied. The property functions of air were curve-fitted from property tables of air found in Çengel *et al.* (2011). The property functions of methanol were curve-fitted from property tables of methanol found in Pioro and Pioro (1997). The thermal conductivity of all materials used in the experiment were taken from Çengel *et al.* (2011), except that of the insulation which was provided by the supplier.

B.2 Expansion/Contraction of Fluid In the Loop

The flow rate of the fluid in the loop is calculated using equation 3.20. However, the flow in or out of the expansion line is based on the expansion and contraction of the fluid in the loop. The expansion and contraction of the loop also effects the mass and energy conservations but its effect in the momentum equation is assumed to be negligible.

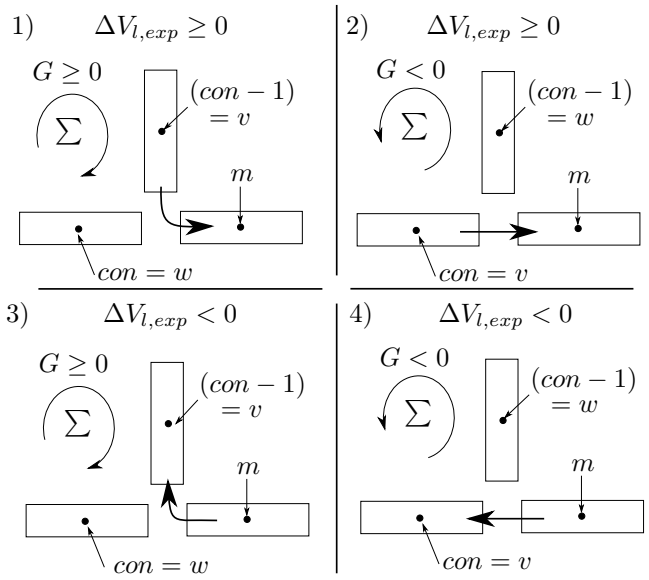

Figure B.1: Flow of mass and energy to and from the expansion line under different conditions

The expansion/contraction of the fluid in a control volume is defined as

$$\Delta V_i^{t+\Delta t} = \frac{m_i^{t+\Delta t,old}}{\rho_i^{t+\Delta t}} - V_i \qquad [\mathrm{m}^3] \tag{B.1}$$

where $m_i^{t+\Delta t,old}$ is the mass for the new time step calculated by equation B.3 and $\rho_i^{t+\Delta t}$ is the new density calculated from the new temperature which in turn is calculated from the new enthalpy from equation 3.26. In other words, the new density, $\rho_i^{t+\Delta t}$, effectively dictates the amount of mass allowed in the control volume $m_i^{t+\Delta t,new} = \rho_i^{t+\Delta t} V_i$ and thus the expanded amount of mass out of the control volume is $\Delta m_{exp} = m_i^{t+\Delta t,old} - m_i^{t+\Delta t,new}$ which has a volume of $\Delta V_i^{t+\Delta t}$. The direction of expansion is positive for expansion out of a control volume.

The volume of the loop is fixed and thus the amount of fluid entering/leaving the expansion line due to expansion/contraction of the loop is the sum of all ΔV_i's around the loop,

$$\Delta V_{exp}^{t+\Delta t} = \sum_{w}^{v} \left(\frac{m_i^{t+\Delta t,old}}{\rho_i^{t+\Delta t}} - V_i \right) \qquad [\mathrm{m}^3] \tag{B.2}$$

this in turn has an effect on the level of the expansion tank. The level of the expansion tank is tracked from which the working pressure of the primary loop is determined at the beginning of each time step. The ΔV_i causes mass to pass over the boundary of the control volume. This is handled by incrementally adding/subtracting this volume of expansion or contraction as a flow of mass,

with its energy, across the control volume boundaries. This is done from a starting control volume w, in the direction of the flow in the loop, incrementally adding/subtracting additional terms to both the mass conservation, 3.10, and energy conservation, 3.26, equations until reaching the end of the loop at control volume v. Control volumes' w and v positions, as shown in Figure B.1, are selected to be either control volume con or $con-1$ which are the two control volumes closest to the expansion line as shown in Figure 3.4. Control volumes' w and v positions are determined by the direction of volumetric flow rate G, thus also determining the direction of summing of expansion, as shown in Figure B.1.

Thus, if $\sum_{k=w}^{i-1} \Delta V_k^t \geq 0$ then

$$m_{i,in'}^t = \left(|\sum_{k=w}^{i-1} \Delta V_k^t|\right)\rho_{k-1}^t$$

where $in' = k-1$, else

$$m_{i,in'}^t = -\left(|\sum_{k=w}^{i-1} \Delta V_k^t|\right)\rho_k^t$$

where $in' = k$, and if $\sum_{k=w}^{i} \Delta V_k^t \geq 0$ then

$$m_{i,out'}^t = \left(|\sum_{k=w}^{i} \Delta V_k^t|\right)\rho_k^t$$

where $out' = k$, else

$$m_{i,out'}^t = -\left(|\sum_{k=w}^{i} \Delta V_k^t|\right)\rho_{k+1}^t$$

where $out' = k+1$.

Taking the above mass flows and making adjustments for them in equations 3.10 and 3.26 for the next time step gives

$$m_i^{t+\Delta t,old} = m_i^t + \Delta t\Big[\big(|G^t|[\rho_{in}^t - \rho_{out}^t]\big)\Big] + \big(m_{i,in'}^t - m_{i,out'}^t\big) \quad \text{[kg]} \quad \text{(B.3)}$$

and

$$h_i^{t+\Delta t} = \Big[(mh)_i^t + \Delta t\big((\dot{m}h)_{in}^t - (\dot{m}h)_{out}^t + \dot{Q}_{in}^t - \dot{Q}_{out}^t\big) + (mh)_{i,in'}^t - (mh)_{i,out'}^t\Big] / \Big[m_i^{t+\Delta t,old}\Big] \quad \text{[J/kg]} \quad \text{(B.4)}$$

The control volume just after the connection control volume, m, in the direction of the flow, is seen as w. Thus, w is con when $G \geq 0$ and $(con-1)$ when $G < 0$ with the summing direction for the incremental adding/subtracting going in the direction of G as shown in Figure B.1. This implies that

$$m_{w,in'}^t = 0$$

In Figure B.1 the flow of mass and energy due to expansion and contraction is shown, implying that if $\Delta V^t_{l,exp} < 0$ then for the connection control volumes

$$m^t_{v,out'} = -\left(|\sum_{k=w}^{v} \Delta V^t_k|\right)\rho^t_m$$

where $v, out' = m$.

B.3 Time Loop Subroutine

The time loop subroutine, as executed in the primary routine, consists of five steps as seen in Figure B.2. The Time loop subroutine begins with a speed check of the fluid flowing in the loop. Thereafter, the program executes the primary loop contents and then expansion line contents subroutines. Once all the properties for the expansion line and loop have been calculated the pressure of the system is recalculated using the pressure calculation subroutine, a concept that is explained in section 3.3.2. Once all the properties of the control volumes have been calculated the current starting values are replaced by the new values providing the next time steps starting values.

With the use of the discrete time-wise integration using and explicit integration scheme the spatial coordinates of the problem, namely time and control volume size, must adhere to the Courant-Friedrichs-Lewy (CFL) condition. The condition named after its authors who describe it in their 1928 paper (Courant *et al.*, 1928). This is necessary for the stability of the time marching scheme. For the one-dimensional upwind differencing case the CFL condition has the following form

$$C = \frac{v\Delta t}{\Delta x} \leq C_{max} \tag{B.5}$$

where C is the Courant number, a dimensionless number, v is the velocity, Δt and Δx are the length of time step and the control volume respectively. The value of C_{max} for an explicit solver is $C_{max} = 1$ for the one dimensional case using upwind differencing. The CFL stability criteria relates the length of time step and lengths of each spacial coordinate and the maximum speed with which information can travel in the physical space. It in essence ensures

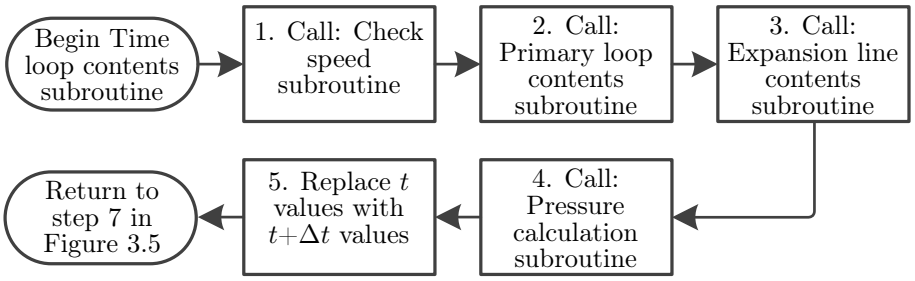

Figure B.2: Time loop subroutine executions steps

that in one time step information cannot pass right through and effectively skip a control volume.

The check speed subroutine, step 1 in Figure B.2, ensures that the time step is of adequate length that a fluid particle cannot travel more than a selected percentage of the control volume's length, Δz, as seen in Figure 3.1 (a), thus ensuring the CFL criteria is met. The percentage of length a particle could travel through a control volume was arbitrarily and conservatively selected to be 20% which equates to a $C_{max} = 0.2$. If the velocity in a control volume was too great for the selected time step the time step was reduced and if the smallest allowed time step still resulted in $C_{max} > 0.2$ program would be terminated. The check speed subroutine allowed for a variable time step within the program and thus a larger time step could be selected at the beginning reducing the time required to run the simulation.

B.3.1 Primary loop contents subroutine

The primary loop contents subroutine calculated the properties of the control volumes in the loop. The steps in the subroutine are as follows:

1. **Check flow direction**
   The initial logic is the flow direction sign ensuring the right *in* and *out* values are used. The absolute values of any property or value are used to ensure that a negative flow does not have an effect on the structure of the conservation equations as laid out in section 3.2. Thus, with reference to Figure 3.4, if $G \geq 0$ then

$$in = i - 1$$

$$out = i$$

$$in_j = e$$

$$K_L = K_{L,forward}$$

   else

$$in = i + 1$$

$$out = i$$

$$in_e = j$$

$$K_L = K_{L,reverse}$$

   in words one can interpret the above as: If the flow is in the direction of the numbering of the control volumes values "in" is $(i - 1)$, if it is in the opposite direction then "in" is $i + 1$. The "out" in the equations is always the i^{th} control volumes value. $K_{L,forward/reverse}$ in the above was the minor friction loss coefficient vector that held the different minor loss coefficients for the different zones of the primary loop. This step also enforced the direction of expansion as explained in section B.2.

2. **Calculate mass flow rate in loop**

$$\dot{m}_i^{t+\Delta t} = \rho_i^t \ |G^t| \tag{B.6}$$

3. **Calculate new mass**
   Calculate the mass of all the control volumes using equation B.3. This mass is referred to as the "*old*" new time step's mass, $m_i^{t+\Delta t,old}$, and is used in the calculation of the new enthalpy and expansion of the loop.
4. **Calculate thermal resistances**
   The dynamic viscosity, using equation 3.7 when $x_i > 0$, and the Reynolds number of each control volume is calculated. These values are then used in the calculation of the thermal resistances following the model outlined in Appendix A.
5. **Calculate heat transfer rate in and out of each control volume**
   The heat transfer rate from the control volume to the environment is then calculated using equation 3.30. Additionally the heat transfer for the effected control volumes that have heat added and removed in zones 1.2 and 3.1 is calculated and taken into account. The new surface temperatures for the next time step's external heat transfer coefficients is also calculated.
6. **Calculate new enthalpy**
   Calculate the new enthalpy of the control volumes using equation B.4.
7. **Check if fluid is boiling or not**
   Situation 1 - *Liquid phase* $(x = 0)$

$$h_i^{t+\Delta t} \leq h_{f@P_i}$$

   Situation 2 - *Two phase flow* $(0 < x < 1)$

$$h_{f@P_i} < h_i^{t+\Delta t} < h_{g@P_i}$$

8. **Calculate new temperature, density, thermal conductivity and mass**
   Situation 1 - *Liquid phase* $(x_i = 0)$

$$\begin{aligned} T_i^{t+\Delta t} &= f(h_i, P)^{t+\Delta t} \approx f(h_i)^{t+\Delta t} \\ \rho_i^{t+\Delta t} &= f(h_i, P)^{t+\Delta t} \approx \rho_{l,sat@T_i^{t+\Delta t}} \\ k_i^{t+\Delta t} &= f(h_i, P)^{t+\Delta t} \approx k_{l,sat@T_i^{t+\Delta t}} \\ m_i^{t+\Delta t,new} &= \rho_i^{t+\Delta t} V_i \end{aligned}$$

   Situation 2 - *Two phase flow* $(0 < x_i < 1)$

$$T_i^{t+\Delta t} = T_{sat@P_i}$$

   Calculate mass fraction, x_i

$$x_i^{t+\Delta t} = \frac{h_i^{t+\Delta t} - h_{l@T_i^{t+\Delta t}}}{h_{g@T_i^{t+\Delta t}} - h_{l@T_i^{t+\Delta t}}}$$

thus the void fraction becomes:

$$\alpha_i = \left(1 + \frac{1-x_i^{t+\Delta t}}{x_i^{t+\Delta t}} \frac{\rho_{g,sat@T_i^{t+\Delta t}}}{\rho_{l,sat@T_i^{t+\Delta t}}} SR\right)^{-1}$$
$$\rho_i^{t+\Delta t} = \alpha_i \rho_{g,sat@T_i^{t+\Delta t}} + (1-\alpha_i)\rho_{l,sat@T_i^{t+\Delta t}}$$
$$k_i^{t+\Delta t} = \alpha_i k_{g,sat@T_i^{t+\Delta t}} + (1-\alpha_i)k_{l,sat@T_i^{t+\Delta t}}$$
$$m_i^{t+\Delta t,new} = \rho_i^{t+\Delta t} V_i$$

but if $\rho_i^{t+\Delta t} < 20$ then $\rho_i^{t+\Delta t} = 20$.

9. **Calculate the expansion/contraction of the loop**
   Calculate the expansion and contraction of the loop control volumes using equation B.1 and for the entire loop using equation B.2.
10. **Calculate the new volumetric flow rate**
    Calculate the sum of the momentum flux difference using equation 3.17, the sum of the friction terms using equation 3.18, the sum of the buoyancy terms using equation 3.19 and then the new volumetric flow rate using equation 3.20 with the direction of the flow specifying the signs if $G \geq 0$ then

$$G^{t+\Delta t} = \frac{\sum_j^e \rho_i^t}{\sum_j^e \rho_i^{t+\Delta t}} G^t + \Delta t \frac{M-F+B}{\sum_j^e (\rho_i^{t+\Delta t}) \sum_j^e (\Delta z_i / A_{x,i})}$$

else

$$G^{t+\Delta t} = \frac{\sum_j^e \rho_i^t}{\sum_j^e \rho_i^{t+\Delta t}} G^t + \Delta t \frac{-M+F+B}{\sum_j^e (\rho_i^{t+\Delta t}) \sum_j^e (\Delta z_i / A_{x,i})}$$

B.3.2 Expansion line contents subroutine

The expansion line contents subroutine involved all the steps relating to the expansion line and expansion tank, zone 5 in Figure 3.4. The level of the expansion tank had a direct influence on the pressure of the system. As stated in section 3.3.5 the expansion line and tank were treated as a single control volume. The following steps, with subscripts of values as defined in Figure 3.4, were completed to calculate the properties of zone 5:

1. **Calculate volume flow into the expansion line**
   Using the expansion/contraction of the loop, equation B.2, the flow rate in/out of zone 5 was calculated as

$$G_{exp} = \Delta V_{exp} / \Delta t$$

2. **Calculate new mass of zone 5**
   The new mass of zone 5 is calculated using the summation equation 3.10 for the entire zone 5 such that if $G_{exp} \geq 0$

$$m_{tot}^{t+\Delta t} = \sum_{i=m}^{n} m_i^t + \Delta t(|G_{exp}| \rho_{con}^{t+\Delta t})$$

else

$$m_{tot}^{t+\Delta t} = \sum_{i=m}^{n} m_i^t - \Delta t(|G_{exp}|\rho_m^t)$$

3. **Calculate thermal resistances**
   The dynamic viscosity and the Reynolds number of each control volume is calculated. These values are then used in the calculation of the thermal resistances following the model outlined in Appendix A.
4. **Calculate heat transfer rate in and out of each control volumes**
   Calculate the heat transfer rate from the control volume to the environment using equation 3.30.
5. **Calculate new enthalpy**
   Calculate the new enthalpy of the control volumes using a modified single control volume form of equation 3.20.
   if $G_{exp} \geq 0$

$$h_{tot}^{t+\Delta t} = \frac{\sum_{i=m}^{n}(mh)_i^t + \Delta t(|G_{exp}|(\rho h)_{con}^{t+\Delta t} - \sum_{i=m}^{n}\dot{Q}_{i,out})}{m_{orig} - \sum_{i=j}^{e} m_i^{t+\Delta t}}$$

   else

$$h_{tot}^{t+\Delta t} = \frac{\sum_{i=m}^{n}(mh)_i^t + \Delta t(-|G_{exp}|(\rho h)_m^t - \sum_{i=m}^{n}\dot{Q}_{i,out})}{m_{orig} - \sum_{i=j}^{e} m_i^{t+\Delta t}}$$

6. **Calculate new temperature, density and mass**
   The new temperature, density and mass of all the control volumes in zone 5 are based on the average new enthalpy h_{tot} thus

$$T_i^{t+\Delta t} = f(h_{tot}, P)^{t+\Delta t} \approx f(h_{tot})^{t+\Delta t}$$
$$\rho_i^{t+\Delta t} = f(h_i, P)^{t+\Delta t} \approx \rho_{l,sat@T_i^{t+\Delta t}}$$
$$m_i^{t+\Delta t} = \rho_i^{t+\Delta t} V_i$$

   however the mass and volume of the expansion tank, n, are calculated using equations 3.31 and 3.32 from which the height, Δz_n, is calculated.

B.4 Program General Results and Operation

The program to solve the primary loop model used all variables declared as double precision to increase accuracy. The bulk speed caused by the flow rate and expansion were used to change the time step to keep the Courant number below 0.2. If the Courant number was found to exceed 0.2 the time step was reduced by factor ten. Thus the CFL condition was always satisfied and if for the smallest allowed time step the Courant number was still greater than 0.2 the simulation was stopped. The simulation could thus be stopped for too great expansion or too high flow rate. Other checks that stopped the program were checks on the density and temperature in the property functions ensuring it remained in logical bounds. The constraints on Courant number were found to stop the simulation in all instances, this happening typically at the onset of boiling.

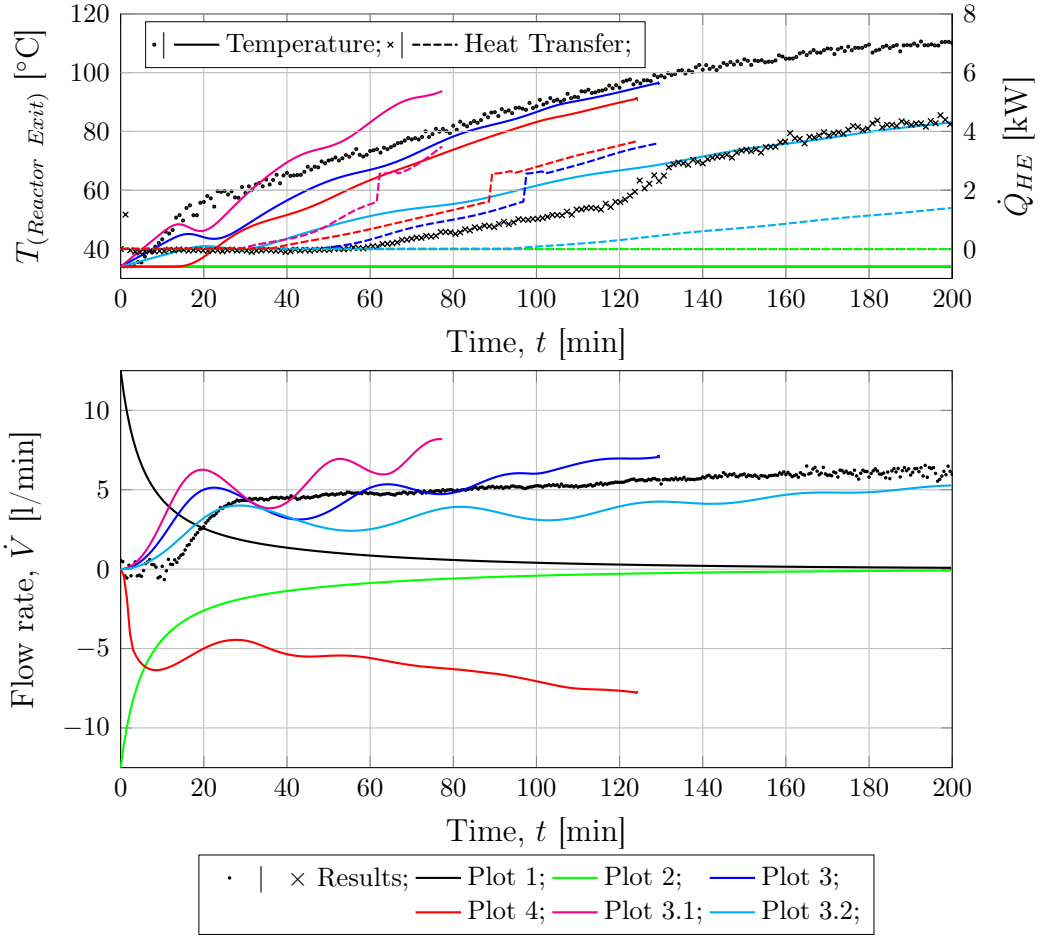

Figure B.3: Temperature, heat extracted by secondary loop and flow rates simulation results for: Plot 1 - no heat input with starting flow-rate, $\dot{V}$ =12.5 l/min; Plot 2 - no heat input with starting flow-rate $\dot{V}$ =−12.5 l/min; Plot 3 - heat input 7668.6 W distributed in reactor and riser; Plot 3.1 - heat input increased by 50% of Plot 3; Plot 3.2-heat input decreased by 50% of Plot 3; Plot 4 - heat input 7668.6 W distributed in down-comer zones 5.1-5.5. The results are overlaid on test 6 results.

Unless otherwise specified the starting flow rate was zero, the selected grid and starting time step sizes were $\Delta z = 125$ mm and $\Delta t = 0.01$ s. Figure B.3 shows the response for typical situations to show that the basic operation of the program gives expected results. These results are overlaid on test 6 experimental results but the simulations were all stopped prematurely as the imposed CFL condition was violated. For all the situations a constant starting temperature of 34 ℃ is allocated to each cell such that temperature/density gradients do not affect the hydraulic response.

The response of the loop to a forward and reverse starting flow rate is shown in Figure B.3 by Plots 1 and 2. For Plot 1 and 2 there was no heat transfer to the surroundings and the heat input was set to zero. As expected the flow

rate tends towards zero with a curve indicative of effect of the squared velocity term in the shear stress term, τ. No heat transfer or temperature change was present in the results.

Plot 3, in Figure B.3, show the model's response for a heat input of 7668.6 W. The heat was distributed evenly according to the volume of the cells in the reactor and riser section, zones 1 and 2 in Figure 3.4. Thus as expected the one sided power input results in a positive flow rate however oscillations are present which are not found in the experimental results. Plot 3.1 and 3.2 have the same solution set-up as Plot 3, except for 50% more and less power input respectively. The resulting flow rates result in higher and lower flow rates, temperatures and heat transfer rates for the equivalent time compared to Plot 3. This is as anticipated but interestingly the oscillations are also more and less exaggerated for more or less power input. These start-up oscillations are not present in the experimental results, however are present in Dobson's 1993 experimental work.

Plot 4 shifts the heat input of 7668.6 W to the opposing leg of the primary loop. The down-comer is smaller in cross-sectional area and thus also in cell volume size. The higher absolute velocity of the reverse flow for Plot 4, as shown in Figure B.3, is expected. This is as the smaller control volume with less mass absorbing the equivalent power results in a higher temperature. The higher temperature in turn results in larger density differences and ultimately a larger buoyancy driving force and higher flow rate. The higher buoyancy force also results in a faster start up flow rate transient as seen by the initial peak in flow rate happening at ± 10 min for Plot 2 compared to that of ± 20 min as in the case of Plot 3. The earlier onset in heat transfer is also expected due to the higher temperatures.

The simulation of the primary loop's basic functions are thus as anticipated thus verifying its results and functioning somewhat. The unexpected largeness in amplitude of the oscillations and inability to capture the phase transition are points of concern as discussed in 7.4.3.

B.5 Grid and Time Step Independence

Typically as $\Delta t \to 0$ and $\Delta z \to 0$ the solution should converge. The program was written in such a way that the number of control volumes in a zone could be determined by specifying a maximum control volume size, Δz_{max}. Thus, the number of control volumes in a zone were $n = l_{zone}/\Delta z_{max}$ rounded up to the next whole number, except in the case of zone 3.1, the heat exchanger as seen in Figure 3.4, which was always restricted to one control volume. The length of the time step, Δt, could be specified to remain fixed or be dynamically changed according to the CFL criterion set. The program was run until the effects of boiling caused unrealistic values or violation of CFL value of $C_i > 0.2$ was found.

The time step and grid size independence investigations were performed with a constant power input of 7668.6 W in the reactor cells, zone 1.2. This

power input is average value from experimental test no. 6. A constant starting temperature of 34 °C for all control volumes was selected. This was done so that starting temperature profiles within the loop would not influence the investigation's results. The results of the investigation are shown in Figures B.4 and B.5 overlaid on the experimental results of test 6.

B.5.1 Time step independence

Figure B.4 shows the effects of varying Δt from 0.1 s to 10 µs with $\Delta z_{max} =$ 125 mm. For $\Delta t = 0.1$ s the flow rate increases and temperature following a similar path to that of $\Delta t = 1$ ms and 10 ms but the simulation is stopped by the Courant number exceeding 0.2 due to the flow rate. For $\Delta t = 1$ ms and 10 ms the responses are initially, $t = 0 \rightarrow 24$ min, the same however $\Delta t = 10$ ms has a larger oscillation in flow rate. The larger oscillation for $\Delta t = 10$ ms results a lower flow, compared to $\Delta t = 1$ ms, which allows more time for the fluid to heat up in the reactor. The fluid heats up until it boils in the reactor which triggers the CFL criteria stop due to excessive expansion caused by phase change. The peak in flow rate coincides with a trough in temperature at $t \approx 30$ min.

The first oscillation for $\Delta t = 1$ ms is noticeably smaller than that of $\Delta t =$ 10 ms. The lower magnitude of the oscillation and consistently higher flow rate

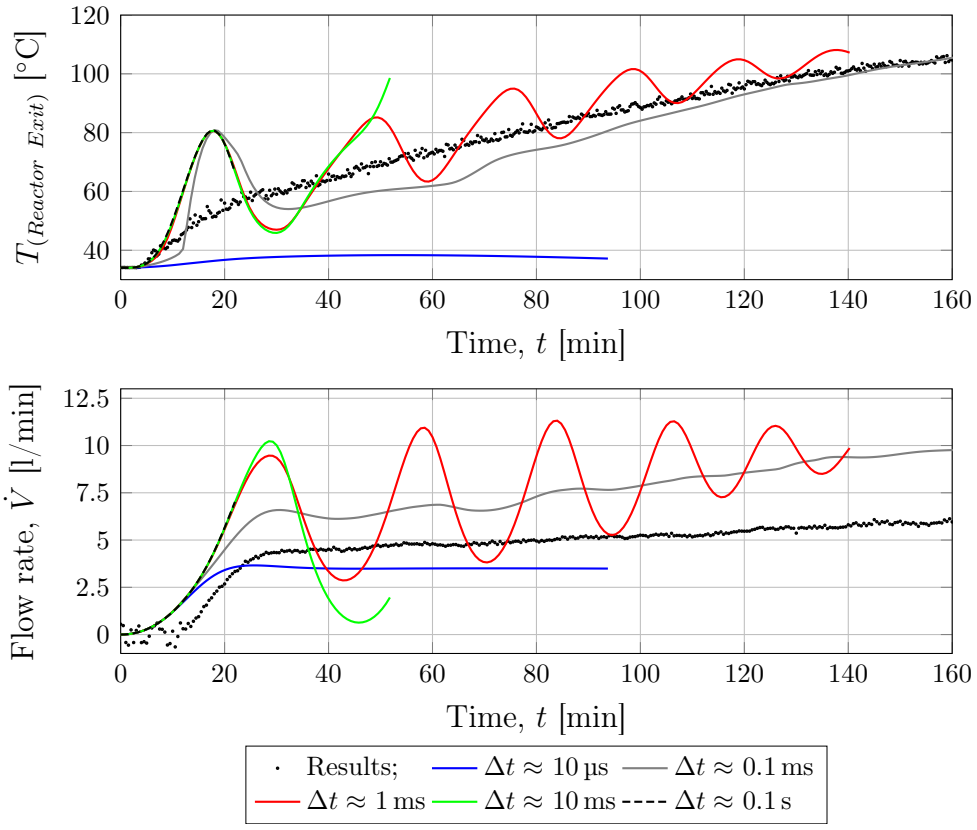

Figure B.4: Computer program simulation results using $\Delta z_{max} \approx 125$ mm different time steps overlaid on experimental test 6 results.

prevent the early onset of boiling as noticed in $\Delta t = 10\,\text{ms}$. The simulation was only stopped at $t \approx 140\,\text{min}$ due to expansion caused by phase change violating CFL criterion.

The response for $\Delta t = 0.1\,\text{ms}$ is considerably different to the larger time step responses. The flow rate does not peak as excessively and the initial increase in temperature begins later with a noticeably steeper gradient. After the first peak in temperature there are no further noticeable oscillations in temperature profile with only small oscillations in flow rate. The flow rate is considerably larger when compared to test 6 results. For $\Delta t = 0.1\,\text{ms}$ it is as if some destructive interference has taken place to reduce/dampen the oscillations. The temperature of the reactor exit is noticeably lower for $t = 30 \rightarrow 140\,\text{min}$ compared to test 6 results.

The smaller time step it seems helps dampen the oscillations with no oscillations in the flow rate results for $\Delta t = 10\,\mu\text{s}$. The flat temperature response for $\Delta t = 10\,\mu\text{s}$ is not representative of reality or comparable with other simulation results. With a power input one expects the temperature of the system to increase. These findings prompted an investigation into the operation of the program. The error was attributed to the expansion and contraction routine and cure fitting errors becoming dominant for the smaller time steps. It was found that only the reactors control volumes were increasing in temperature until they boiled stopping the program due to the Courant number exceeding 0.2 due to expansion.

A small time step reduces the dominance of enthalpy change due to mass flowing in and out of a control volume in the energy equation. In equation B.4 a small time step in combination with low flow rates, as typically found in the system, resulted in little change cause by enthalpy entering and leaving the control volume, even for substantially different enthalpies. The change in enthalpy caused by expansion and contraction is independent of time step size. When mass is removed/added due to expansion/contraction it is only passed on during the next time step.

This delay in passing mass and its respective energy onwards during the current time step negated the need for a iterative scheme to solve for the mass and energy transfers due to expansion/contraction. An iterative scheme would be required as the cell's mass with its calculated density at the end of the time step would have to equal/fill the volume of the control volume. If not equal it would mean that mass and energy due to expansion and contraction would have crossed the cell's boundaries. However, which boundaries the mass crossed and how the expansion of other cells affected the current cell's properties is not known. To solve this, it is expected, would require some form of iterative scheme for each time step. The method, as explained in Appendix B.2, removed the need for this iterative scheme. The expansion and contraction could not be ignored because the difference in densities between the gas and liquid phases would result in large movement of mass between the control volumes and ultimately the expansion line and primary loop.

The draw back of the method as explained in Appendix B.2 with the delay in passing mass on was it allowed a scenario where oscillating expansion and contraction values manifested. This, in combination with the effect of the small time step and errors in curve fitting, resulted in expansion and contraction enthalpy changes becoming dominant which oscillated from positive to negative for each time step. This created a situation where energy was lost. This resulted eventually in a near steady state situation with energy unable to be transported out of the reactor. In other words the transfer of energy due to the flow was negated by errors in curve fits and a small time step allowed for numerical errors to become dominant. These problems also highlight that the way expansion and contraction were incorporated requires attention as discussed in 7.4.3.

B.5.2 Grid size independence

Figure B.5 shows the effects of varying Δz_{max} from 1.5 m to 40 mm with a $\Delta t = 0.01$ s. The results of the simulation diverge as Δz_{max} decreases with the oscillations in temperature and flow rate becoming greater. The peak of the flow oscillations tend to be constant from $\Delta z_{max} = 125$ mm up until

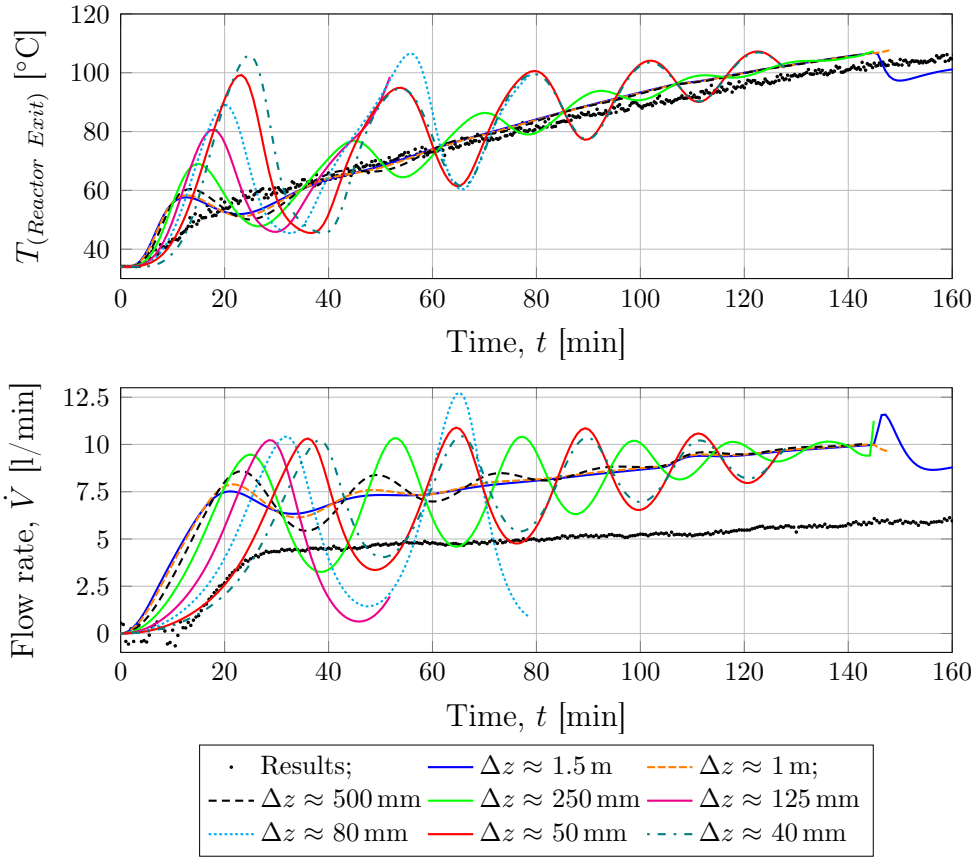

Figure B.5: Computer program simulation results using different maximum control volume lengths and a time step of $\Delta t = 0.01$ s. For each Δz the corresponding maximum Courant number for a flow rate of 15 l/min is given.

$\Delta z_{max} = 40\,\text{mm}$ however the phase shifts. The phase shift is seen by the peaks of the oscillations being more delayed the smaller the control volume size. The smaller the control volumes, the larger the delay in the start up transient and heat transportation in the loop.

The phase shift is caused by this delay in the start up transient of the primary loop's flow. The delay is caused by energy only moving from one control volume to the next control volume in a single time step. Thus the more control volumes (the smaller Δz_{max}) the longer it takes for energy to be transported from one point to the next using the same time step size. Alternatively the assumption of the homogeneous well mixed control volume means that for larger control volumes, the energy passed on in a single time step affects a larger amount of fluid compared to smaller control volumes. Thus energy is transported faster from one point to the other the larger the control volume is.

If energy is moved faster through the loop for the larger control volumes, the resulting hydraulic feed back due to density changes is also larger. This is as the density of a larger column, Δz, of water will change faster when compared to smaller control volumes. The buoyancy term in the moment equation 3.20, $g\rho_i \Delta z_i$, then ultimately results in a larger difference earlier for the larger control volumes resulting in an earlier establishment of flow rate.

The initial peak in temperature at the reactor exit is effectively constant as $\Delta z_{max} = 1.5\,\text{m} \rightarrow 500\,\text{mm}$. Thereafter the initial peak in temperature becomes ever greater caused by the lower flow rate of the delayed start up transient. These results give a clear indication that the effects of phenomena are being ignored that is exasperated by having smaller, and thus more, control volumes. The oscillations are notably smaller and more representative of actual results for the $\Delta z = 1.5$ m as the oscillations are dampened. The homogeneous model implies a well-mixed control volume. During experimentation observations of noticeable plumes in the larger sections (reactor, riser and steam drum) were made. These plumes were clearly distinguishable having a flow rate and temperature different to that of the bulk fluid as discussed in Chapter 6.2. The convective mixing of the plumes could possibly be isolated as one ignored phenomena as the plumes encouraged the mixing of the fluid.

The theory used to simulate the primary loop only allows for flow in one direction, thus, mixing over cell boundaries due to plumes, which is relatively independent of the bulk fluid flow, is not captured. It also makes sense that the error is enhanced by smaller control volumes which in turn, through the homogeneous definition of well-mixed, actually reduce the overall mixing in the loop.

The volumetric flow rate is assumed constant in the loop and dependent only on the momentum, friction and density differences of the cells around the loop. This, combined with the assumption that the flow rate is constant across the cross-sectional area and uni-directional, places constraints on the solution method. This results in a solution which is unrepresentative of the ob-

served and recorded reality. The assumptions of well mixed and uni-directional flow could be applicable in a case where the cross-sectional area is small thus restricting the development plume type buoyancy driven currents which are independent of bulk fluid motion.

The effect of the uni-directional constant volumetric flow rate assumption results in a situation where so called slugs of higher temperature water are created as mixing is prevented. The higher temperature slugs with differing densities create a hydraulic feed back in the buoyancy term of the momentum equation. The higher temperature slug moves into the riser section and lower density will result in a larger buoyancy force and yield a higher flow rate. This in turn results in less heating time for the water below it and thus aggravating the temperature difference between sections of the loop.

When the higher temperature slug passes into the down-comer its lower buoyancy will retard the flow rate producing another higher temperature slug in the reactor. This is believed to result in the oscillation of the flow rate as seen in Figure B.5 for the smaller Δz's with the peak in temperature at the reactor exit followed by a peak in the flow rate. A form of density wave oscillations are induced by the simulation method.

The choice of Δz and Δt seem to result in situations than can result in constructive or destructive instances of these self sustained density wave oscillations. This is seen in both Figure B.5 and more clearly in Figure B.4 for $\Delta z = 125\,\text{mm}$ and $\Delta t = 0.01\,\text{s}$, where, after the first trough in reactor exit temperature, the temperature has a positive slope until boiling begins in the reactor and the simulation is stopped.

The theoretical model seems to have its own own phase and frequency dependency on both time step and grid size. Its dependency on grid size is illustrated best, in Figure B.5, by the comparison between $\Delta z = 250\,\text{mm}$ and $\Delta z = 50\,\text{mm}$ with both differences in phase and frequency in the thermal hydraulic response. The differences in both phase and frequency is thought to stem predominantly from differing start-up transients.

The simulations with larger control volumes simulated a longer time period. This was due to the violation of the condition on the Courant number requiring larger flow or expansion/contraction rate. For $\Delta z = 1.5\,\text{m}$ boiling actually was achieved and the flow rate peaked and then dropped. The temperature response was similar to that observed during experimentation with cold water drawn in from the down-comer reducing the temperature entering and leaving the reactor.

C. Experiment Data Acquisition System, Post Processing and Error Propagation

This appendix deals with the data acquisition system of the experimental set-up as well as its error propagation. The probes as well as data acquisition units are discussed giving information such as positioning, sampling rates and serial numbers. The care taken in positioning the thermocouples used for the calculation of heat removal is highlighted. The post processing of the data is briefly discussed giving formulas used for calculation of input power and heat removal. The results and assumptions used for a direct error propagation analysis are given lastly.

C.1 Data Acquisition

An Agilent 34970A data acquisition/switch unit [SN: US37047554] and an Agilent 34901A 20 channel multiplexer [SN: MY41070892] were used for the temperature and voltage measurements. To measure the pressure difference over the orifice plate a Hottinger Baldwin Messtechnick, HBM, differential pressure transducer [Type: PD1, SN: 25022, ΔP 0.1 Bar $\triangleq$8 mV/V, PN: 50 Bar] was connected to a HBM QuantumX-MX840A [SN: 0009E50038A2] data logger. The data loggers were connected to a Lenovo Y570 laptop [SN:CB12817939, OS:Window 7 Professional SP1 64-bit], the QuantumX with an Ethernet cable and the Agilent were interconnected using a Agilent GPIB-USB connection cable [SN:MY50060822]. To configure the data loggers as well as record results, the respective software used for the QuantumX and the Agilent was; CatmanAP 3.3.1.44 [SN: 0EAFU051233100010, HBM] and BenchLink Data Logger 3 [Version 4.2]. Of the 20 channels available in the Agilent card, 14 were occupied by thermocouple probes and 3 by AC voltage measurements. An entire schematic of the data acquisition can be seen in Figure C.1.

The Agilent card's channel and respective measurement points are seen in Figure C.1. The Agilent card was located in slot 1 and the sample rate selected was 0.1 Hz. This rate was limited by the speed at which the Agilent card could sample, but it proved sufficient as the temperature and voltage did not change rapidly. The Agilent had no scaling on the readings allowing adjustment for calibration to take place during post-processing. Each electrical phase's voltage supplied to the heating elements was measured by the Agilent, using the channels 12, 13 and 14 which measured the RMS of the AC voltage supplied shown in Figure C.1 with the resistance of the corresponding elements being 18.75, 18.3 and 18.1 Ω respectively.

The specifics of the thermocouple probes can be found in Table C.1. The abbreviated names used for the thermocouple probes are as follows: Ch.1) Air temp; Ch.2) CW out; Ch.3) CW in; Ch.4) Steam space; Ch.5) Down-comer inlet; Ch.6) Reactor exit; Ch.7) Riser 1; Ch.8) Riser 2; Ch.9) Riser 3; Ch.10)

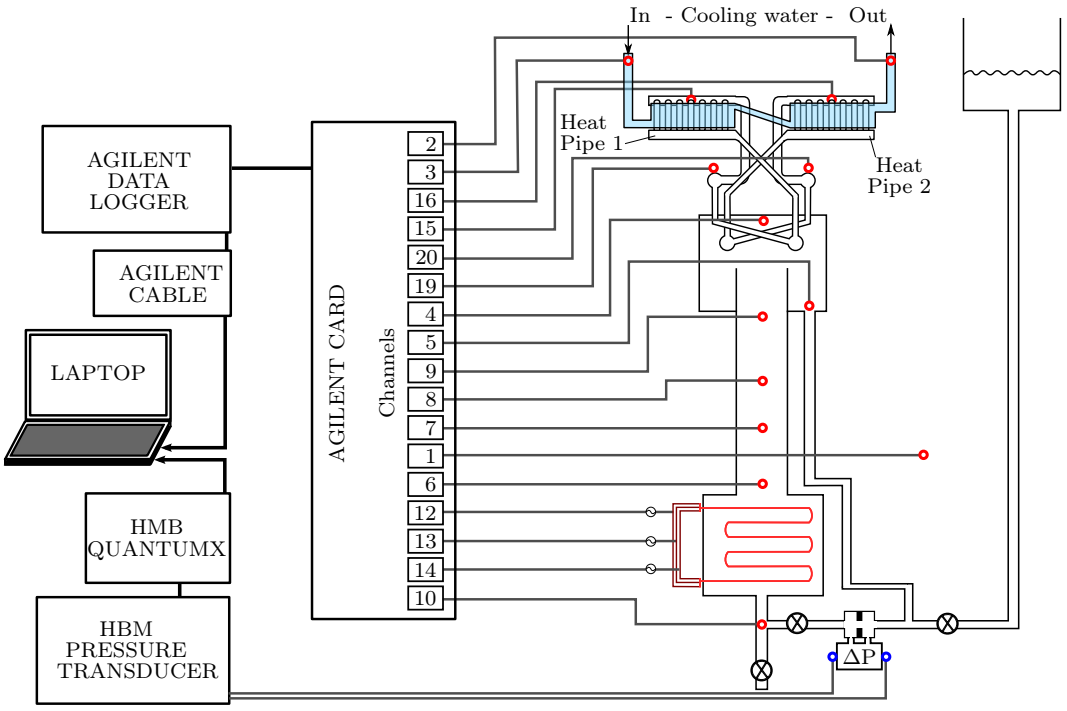

Figure C.1: Schematic of data acquisition system showing approximate measurement positions and data flow through equipment

Table C.1: Thermocouple probe specifics

Ch.	Type	Measurement point
1	T	Ambient air temperature 1.5 m from ground
2	J	Cooling water exit temperature
3	J	Cooling water entrance temperature
4	J	Steam space temperature between lid and tube bundle
5	J	20 mm above down-comer inlet
6	J	Centre of riser 40 mm above bottom flange/reactor exit
7	J	Centre of riser 1004 mm above bottom flange
8	J	Centre of riser 1004 mm below top flange
9	J	Centre of riser 40 mm below top flange
10	J	In T-piece below the reactor/Reactor inlet
15	J	Heat pipe 1: centre of vapour distribution manifold
16	J	Heat pipe 2: centre of vapour distribution manifold
19	T	Heat pipe 1: exterior surface of vapour collection manifold
20	T	Heat pipe 2: exterior surface of vapour collection manifold

Reactor inlet; Ch.15) HP1 inside; Ch.16) HP2 inside; Ch.19) HP1 outside and Ch.20) HP2 outside. The thermocouple probes selected were all ϕ1.6 mm except for the HP1 and HP2 outside thermocouple probes which were soldered thermocouple wires. ϕ1.6 mm probes were selected to have a small thermal inertia that would not affect the readings.

The intention of the HP1 and HP2 outside thermocouples was to verify the temperatures measured by the HP1 and HP2 inside thermocouple probes. The HP1 and HP2 outside thermocouples were affixed to the outside wall of the vapour collection manifold and well insulated with a number of layers of glass fibre wool for heat pipe one and two respectively. The outside thermocouples were only added after calibration of the other probes had taken place and were not calibrated.

The overall energy extracted from the system depended on the temperature difference between the thermocouple probes CW in and CW out, ΔT_{cw}. The importance of ΔT_{cw} meant that the positioning of the probes CW in and CW out was done with care. Firstly, each of the probes were selected to have sufficient length and be fully submerged in the cooling water stream so that conduction along the length of the probe would be minimised. Secondly, the probes were located where an air bubble could not collect around the measuring tip of the probe. The cooling water supply pipe was transparent so that it was certain that the thermocouple probe was not measuring the temperature of an air bubble. Thirdly, at the point of measurement the flow path of the water was narrowed with inserts to ensure a well-mixed reading. The three considerations resulting in representative temperature difference measurement are shown in Figure C.2. To further reduce the error, the flow rate of the cooling water during tests was such that a measurable ΔT_{cw} was present.

The pressure transducer measuring the pressure difference across the orifice was sampled at 10 Hz by the QuantumX. The signal outputted by the QuantumX was in mV and was purposely not filtered or scaled. The output from

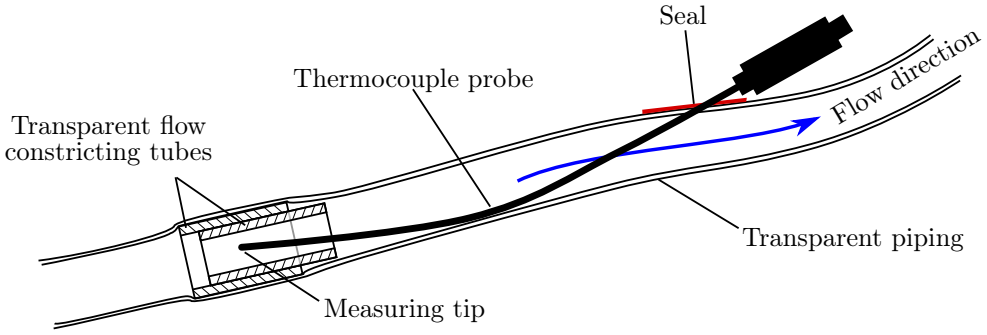

Figure C.2: Schematic of probe in cooling water line showing flow constrictions to increase mixing around measurement tip

the QuantumX was converted to a volumetric flow rate in the post processing of the results.

The mass flow rate of the cooling water was measured by recording the time taken to fill a bucket of water then weighing the bucket. The scale used to weigh the bucket was a SAM CTS-30 [30 kg×1 g, SN: HS20121507]. The readings were performed throughout the tests and recorded in the test log. The cooling water was measured from discharge into pipes that channelled the water to a point near the base of the experiment. A stopwatch was used to time the fill time of the bucket.

C.2 Data Post Processing

By only recording the raw data from the thermocouple probes and pressure transducer, it allowed one to use the test's data if the calibration was found to be inaccurate. Both the Agilent and the QuantumX outputted files were comma separated value files.

The data recorded by the operator in the form of the log book as well as the data captured by the Agilent and QuantumX was all processed using a script written in Matlab® encoding called *read_ data.m*. The execution m-files are specific for the different test batches, however, they do have the same functions but make use of differing input data.

The script *read_ data.m* accepted the three outputs of the test (the QuantumX, the Agilent and two forms of the log book) as inputs. The first versions of the log book contained the mass flow rate of the cooling and the second was a list of notable events. Each book also had the corresponding Agilent scan number as the reference time. The script firstly adjusted the temperatures as explained in section D.1. The script then calculated the flow rate through the orifice plate using the equation from the calibration in section D.3. The mass flow rate was then converted into the correct length vector with corresponding values by the script. The overall heat input was calculated using

$$P = V_1^2/R_1 + V_2^2/R_2 + V_3^2/R_3$$

where V_i represents the recorded voltage supplied to the heating element with resistance R_i. The script then combined the mass flow rate of the cooling water with the respective inlet and exit temperatures to obtain the heat extracted by the heat exchanger using

$$\dot{Q}_{HE} = \dot{m}(c_{p@T_{cw,out}} T_{cw,out} - c_{p@T_{cw,in}} T_{cw,in}) \tag{C.1}$$

Finally, the script outputted a data structure consisting of the adjusted temperature readings, the elapsed time for the Agilent and QuantumX readings, the flow rate through the orifice, the heat inputted and removed from the primary loop, an event log and the mass flow rate of the cooling water, to name the major outputs. Further scripts, such as *PlotsForExpResults.m*, were then written to interpret the data mainly through the use of graphs.

For the post-processing the thermophysical properties of water were acquired using XSteam. XSteam is based on the International Association for Properties of Water and Steam Industrial Formulation 1997 (IAPWS IF-97) and provides a full implementation of the standard giving very accurate steam and water properties in ranges from 0-1000 bar and 0-2000 °C. XSteam is freely available and operates as a Matlab® script. All other fluids or material properties used the same formulas/values as implemented in the Primary Loop's theoretical model, see Appendix B.1.

C.3 Experimental Calculation Error Propagation

A error propagation analysis of experimental error was performed on the calculated results used to characterise the secondary loop heat exchanger. The process of finding all heat transfer coefficients, thermal resistances and heat fluxes uses, directly or indirectly, the experimentally recorded mass flow rates and temperatures. A direct method is used by varying the inputs to study the effects of the worst combination of possible max biases on the experimentally determined results.

The basis of the error propagation analysis is a conservative error of ±310 W on overall heat transfer, due to thermocouple measurements and an error in mass flow rate of ±0.67 %, as noted in Appendix D.1 and D.2. An acceptable and conservative combined error in overall heat transfer of ±350 W is assumed from the combined thermocouple and flow rate error. When an average temperature, e.g. film temperature, is used to calculate a fluid property the effect of the ±0.25 ℃ in the value of the property is assumed negligible.

C.3.1 Error propagation effects on $h_{eo,l}$

Error propagation analysis was not completed on $h_{eo,l}$ for the Semi-empirical characterisation. The analysis was not done as the method of extracting $h_{eo,l,Exp}$ did not result in a usable model which characterised the liquid regime as noted in section 7.3.1. Furthermore, to perform the analysis is complicated by the fact that $h_{eo,l,exp}$ along with the unknown temperatures are calculated using a iterative process. Despite the use of the $h_{eo,l}$ model for the two-phase regime the approximation of $R_{eo,2\phi}$ using equation 4.14 is a large enough assumption to negate the usefulness of an error propagation analysis.

C.3.2 Error propagation effects on C_{sf} and n used in equation 4.16

In section 7.2.1 the inputs, $\dot{Q}_c$, T_i and T_{eo}, were used to obtain C_{sf} and n, used in equation 4.16, as well as the internal heat transfer coefficient $h_{ei,Exp}$ to which the results were ultimately compared. The possible errors in readings of ±350 W for $\dot{Q}_c$ and ±0.25 ℃ for both T_i and T_{eo} results in 26 possible combinations of worst case individual error.

The worst case results of each investigated combination and resulting worst cases of C_{sf} and n is shown in Table C.2. Table C.2, for each worst case, shows the variation used on the three experimental outputs, the percentage deviation from the zero case, and the corresponding values of C_{sf} and n. Each worst

case percentage of C_{sf} and n had its own unique error variation combination. C_{sf} and n both fluctuate with a change to the linear regressed input data set. The error is acceptable as both Çengel *et al.* (2011) and Faghri (1995) make mention of significant uncertainties when using the Rohsenow equation as mentioned in section 7.2.1.

Table C.2: Worst case error propagation results for C_{sf} and n

Case	C_{sf}-min	C_{sf}-max	n-min	n-max
$T_{i,Exp,err}$ [°C]	0.25	-0.25	-0.25	0.25
$T_{eo,Exp,err}$ [°C]	-0.25	0.25	0.25	-0.25
$\dot{Q}_{Exp,err}$ [W]	350	0	350	-350
% Error	-5.08%	4.36%	-1.44%	1.62%
C_{sf}	1.478E-03	1.625E-03	1.615E-03	1.492E-03
n	2.70895	2.67214	2.65793	2.74054

C.3.3 Error propagation effects on $h_{ei,Exp}$ and $h_{co,Exp}$

The effects of error propagation of the three experimental inputs required to obtain $h_{ei,Exp}$ and four inputs for $h_{co,Exp}$ required 26 and 80 different combinations of error to be investigated respectively. The condensing regime experimental results were used to find error propagation effects on $h_{ei,Exp}$ and $h_{co,Exp}$. The worst case experimental error combination's resulting error propagation is shown in Tables C.3 and C.4. The worst case errors in each case, -9.7% and 10.2% for $h_{ei,Exp}$ and -11.7% and 13% for $h_{co,Exp}$, are acceptable considering the investigative nature of the work.

Table C.3: Worst case error propagation results for $h_{ei,Exp}$

	Unit	$h_{ei,Exp}$-min	$h_{ei,Exp}$-max
$T_{i,Exp,err}$	°C	-0.25	0.25
$T_{eo,Exp,err}$	°C	0.25	-0.25
$\dot{Q}_{Exp,err}$	W	-350	350
$\overline{h}_{ei,Exp,err}$	W/m^2·K	-218.1	229.2
σ	W/m^2·K	24.5	26.7
Max $h_{ei,Exp,err}$	W/m^2·K	-287.3	304.9
Max Error	%	-9.7%	10.2%

C.3.4 Error propagation effects on overall heat transfer coefficients

Figures 7.10 and 7.11 show a comparison of the theoretical model's predicted results against the experimentally determined results. The unknown errors of the experimentally determined overall heat transfer coefficients, (UA), were determined directly by varying inputs to minimise and maximise the respective

Table C.4: Worst case error propagation results for $h_{co,Exp}$

	Unit	$h_{co,Exp}$-min	$h_{co,Exp}$-max
$\dot{Q}_{Exp,err}$	W	-350	350
$T_{i,Exp,err}$	℃	0.25	-0.25
$T_{cw,in,Exp,err}$	℃	-0.25	0.25
$T_{cw,out,Exp,err}$	℃	-0.25	0.25
$\overline{h}_{co,Exp,err}$	W/m^2·K	-137.9	153.9
σ	W/m^2·K	7.7	9.0
Max $h_{co,Exp,err}$	W/m^2·K	-161.4	181.8
Max Error	%	-11.73%	13.02%

forms of equation 4.21. The results are give in Table C.5 and similarly to the heat transfer coefficients vary by ±10%.

Table C.5: Error Propagation effects on Overall Heat transfer coefficients, (UA) used in Figures 7.10 and 7.11

		Two-phase Regime			Condensing Regime		
Value	Unit	Total	Cond.	Evap.	Total	Cond.	Evap.
		Lower Worst Case Error					
$\overline{(UA)}_{Err}$	W/K	-4.875	-7.714	-16.683	-4.671	-6.941	-19.498
σ_{Err}	W/K	0.093	0.276	1.924	0.082	0.126	1.834
$(UA)_{Err,max}$	%	-8.80%	-9.19%	-9.70%	-6.13%	-6.39%	-7.36%
		Upper Worst Case Error					
$\overline{(UA)}_{Err}$	W/K	4.938	7.866	17.332	4.727	7.061	20.308
σ_{Err}	W/K	4.892	0.287	2.055	0.084	0.130	1.972
$(UA)_{Err,max}$	%	8.90%	9.38%	10.04%	6.20%	6.50%	7.69%

D. Calibration Procedure and Results for Experimental Set-Up Instrumentation

This appendix deals with the calibration of the thermocouple probes and the orifice flow meter calibration. Both the method as well as the results of the calibration are discussed. The results of the calibration used the post-processing of the data from the experimental set-up.

D.1 Thermocouple Probe Calibration

The thermocouple probes were calibrated using an ISOTECH 4W platinum resistance thermometer (PRT) [model no.: 935-14-72, SN: 191069, Calibration Date 4/02/2013]. The PRT was read by a Hewlett Packard 34401A multimeter [SN: hp3146745396]. A FLUKE 9142 Field Metrology Well (FMW) [SN: B29291] was used as a temperature source with a custom internal heated aluminium billet allowing for eight thermocouple probes and the PRT to be exposed to the same temperature. The calibration set-point temperatures set on the FMW were; 25.68°C; 15°C; 0.01°C; 50°C; 75°C; 100°C; 115°C; 130°C; 150°C. A reading was taken once the system had reached a point of thermal equilibrium. A set of results consisted of two readings for channels 1, 2 and 3, and one reading for channels 4-10, 15 and 16. A set of results were obtained on three separate days forming the data used for the calibration.

For each thermocouple probe the following procedure was used to adjust the readings: The thermocouple probe error, Err, was defined as $Err = Ref - Read$ where Ref and $Read$ are the PRT and the thermocouple probe channel reading respectively. This error was then curve-fitted with respect the to PRT temperature giving

$$Err(x) = C_1 x^2 + C_2 x + C_3 \tag{D.1}$$

where x is the reading from the thermocouple probe. This allowed one to adjust the readings from the thermocouple probe channel giving the adjusted temperature as

$$Temp_{adj} = Read + Err(Read) \tag{D.2}$$

Table D.1 shows the resulting coefficients of the curve fitting procedure. Figures D.1 and D.2 show the plots of the original error, its curve fit and the adjusted result for each measurement channel.

As can be seen in Figure D.1 and D.2, the calibrated thermocouple values errors, Temp$_{adj}$ Err, fall well within a ±0.5°C band compared to the reference temperatures probe. Channel 1 in Figure D.1 has the greatest error of all the probes, however, it is used to measure the ambient air temperature and has sufficient accuracy for the required temperature range.

The calculation of the heat extracted by the secondary loop equation C.1 is reliant on the temperature difference of the inlet, $T_{cw,in}$, and outlet, $T_{cw,out}$,

water of the heat exchanger. $T_{cw,in}$ was measured by channel 2 and channel 3 measured $T_{cw,out}$ for all the tests, excluding tests 5-9 of batch three. The thermocouple probe connected to channel 3 broke at the end of test 4 in test batch three. The broken probe was replaced with the thermocouple probe measuring the internal temperature of heat pipe 1 which was no longer in use, channel 15. The error for each channel except channel 1, which measures the air temperature, fall within the ±0.25 bounds as seen in the respective calibration curves of Figures D.1 and D.2. The maximum error expected for equation C.1 is ±0.5 °C. The error is more significant the smaller the temperature difference and the higher the mass flow rate. In watts the error was calculated using

$$\dot{Q}_{error} = \dot{m}\frac{c_{p@cw,in} + c_{p@cw,out}}{2}0.5 \tag{D.3}$$

which is effectively independent of the size of the temperature difference. This maximum temperature difference error results in an error in $\dot{Q}_{HP}$ range from ±90 W up to ±350 W for the flow rates used during experimentation. The majority of tests result in $\dot{Q}_{HP}$ errors lying between ±280 W up to ±310 W. Thus, for heat transfer in-excesses of 3.1 kW the possible error percentage is bellow 10%.

Table D.1: Table of calibration curve fit coefficients

Channel	C_1	C_2	C_3
1	0.000000000	0.0150252	-0.129643
2	-5.49238E-05	0.0132632	0.038378
3	0.000000000	-0.0067750	0.492477
4	-7.02173E-05	0.0180666	-0.250207
5	-7.26163E-05	0.0184033	-0.346149
6	-7.83911E-05	0.0149923	-0.324308
7	-7.99521E-05	0.0191766	-0.406150
8	-7.36213E-05	0.0148965	-0.305448
9	-6.96052E-05	0.0124220	-0.113021
10	-7.87724E-05	0.0151744	-0.150537
15	-6.14323E-05	0.0099035	-0.003541
16	-6.13705E-05	0.0103100	0.079259

D.2 Cooling Water Mass Flow Rate Error

The error in the mass flow rate readings of the cooling water used for the heat exchanger characterisation is ±0.67 % with a standard deviation of 0.155 %. The error is calculated using the worst combination of the scale accuracy ±1 g and human error in the recorded time of ±0.25 s. The human error was minimised by not depending on reaction time of the measurer but rather using

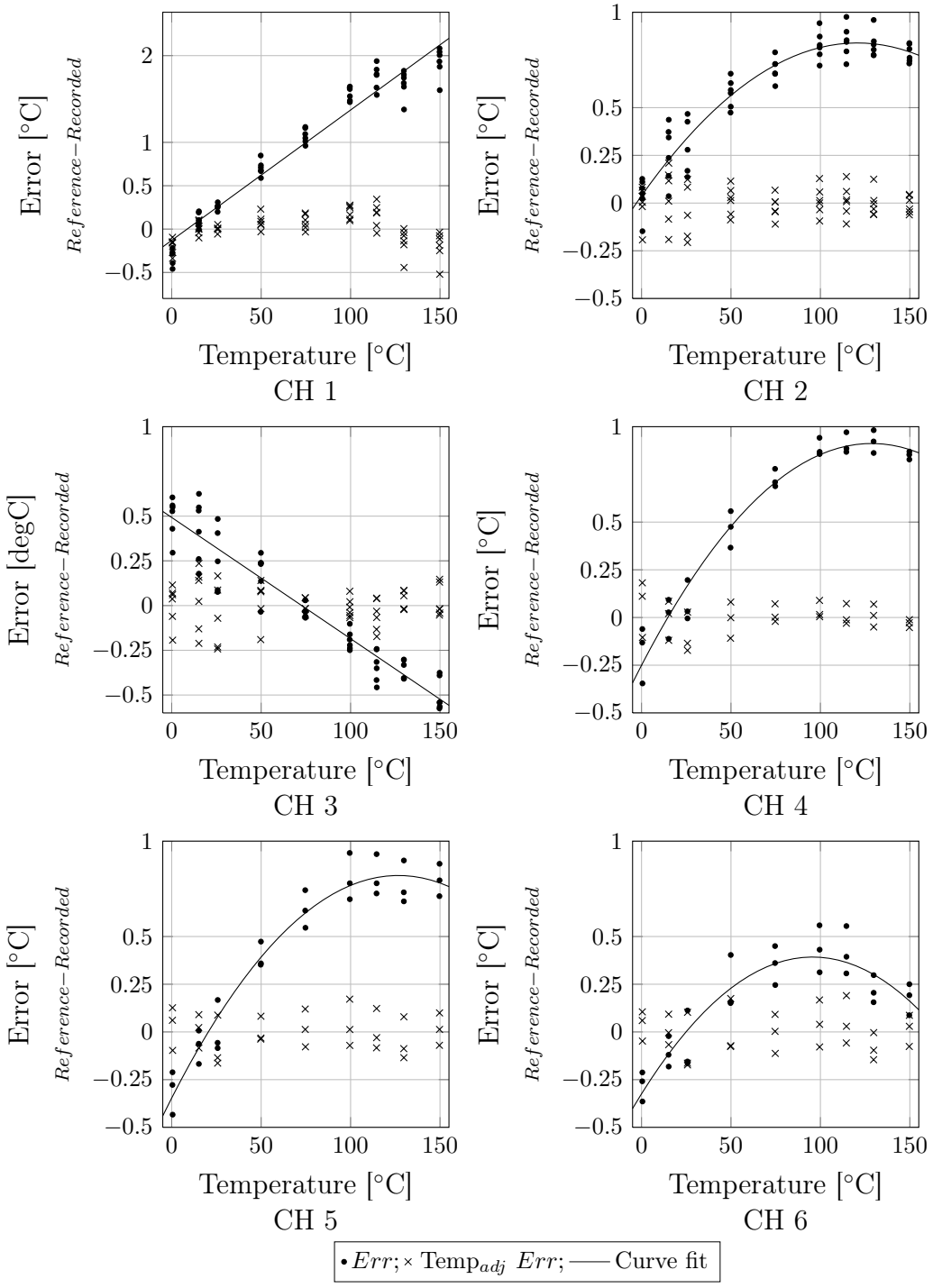

Figure D.1: Error, curve fit function and adjusted error of thermocouple probe readings channels 1-6

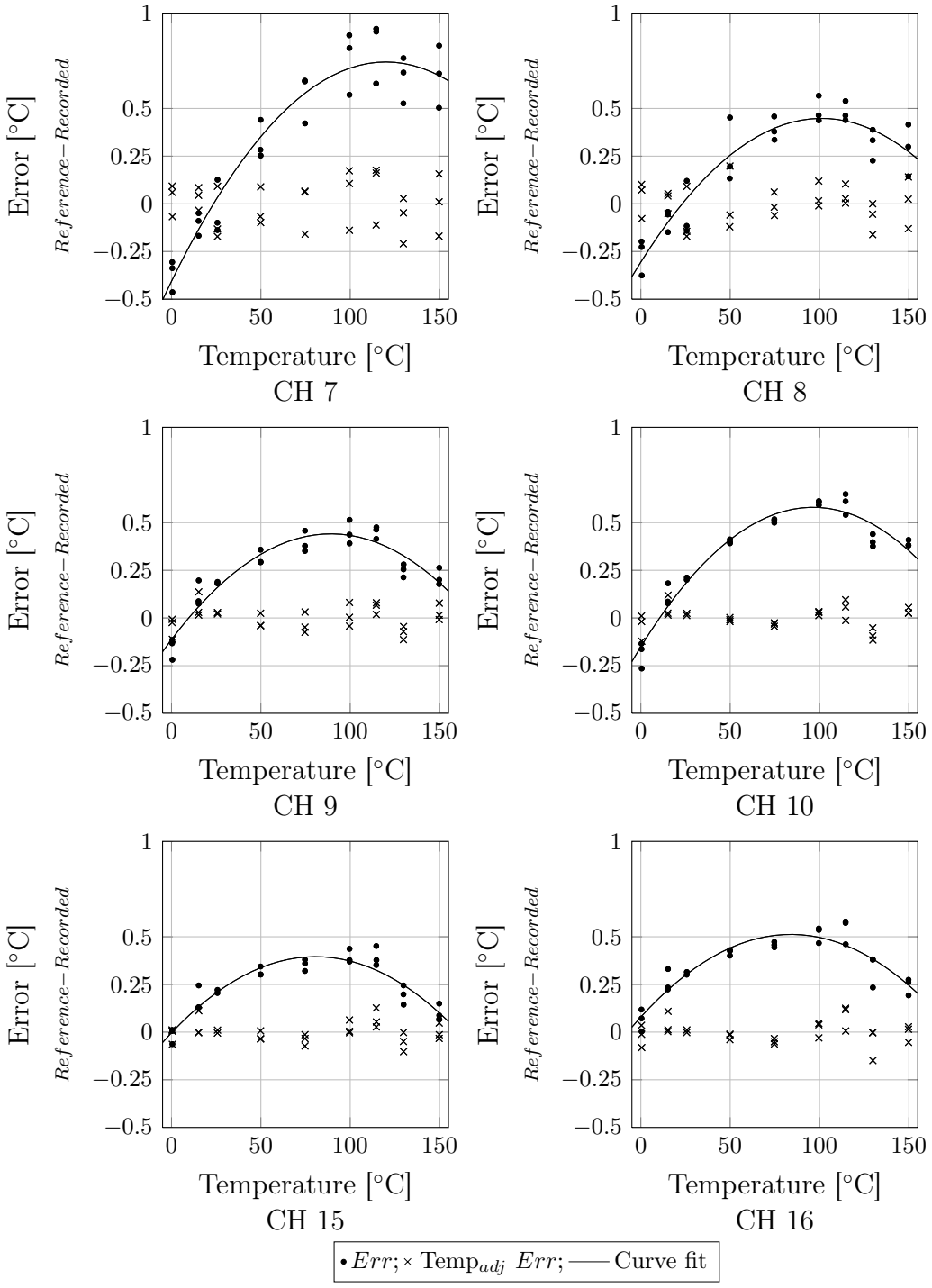

Figure D.2: Error, curve fit function and adjusted error of thermocouple probe readings channels 8-10;15;16

a pre-empted, coordinated and quick movement of the operator when measuring the mass flow rate. The movement consisted of passing the cooling water discharge over the bucket rim and depressing the stopwatch button simultaneously. Thus, the ±0.25 s used is assumed an adequate reflection of the introduced human error. Using equation C.1 the error in the heat transfer rate is proportional to this error in the mass flow rate. Thus for the maximum heat transfer rate of 7.84 kW, used in the heat pipe heat exchanger characterisation, and using the mean error of the flow rate the total error is 53 W.

D.3 Orifice Flow Meter Calibration

The calibration of the orifice flow plate was done using the test set up as shown in Figure D.3. The tests were performed at three different temperature ranges (75-79°C; 51-54°C and 27-29°C) to investigate the effect of temperature on results. Forward and reverse flow test-sets were performed for the different temperatures. Two sets were done for the 75-79°C range while only one set was done for the 51-54°C and 27-29°C ranges respectively. The temperatures that the tests were conducted at were limited to a maximum of 80 °C as this was the temperature limitation of the hot water system. The water temperature was assumed to be the mean of the inlet and outlet temperatures, each being measured by three separate thermocouple probes. It was found that the effects of temperature on the measurements was insignificant and all data points obtained were then used to generate a calibration curve.

Each test-set data point was calculated by setting the flow rate at a predetermined point using the valve at the water inlet. The apparatus was then allowed to constantly measure the pressure difference, outputting millivolts, while three separate mass flow measurements were taken. These mass flow rates were then converted into a volumetric flow rate using a density at the corresponding recorded water temperature. The average output reading over

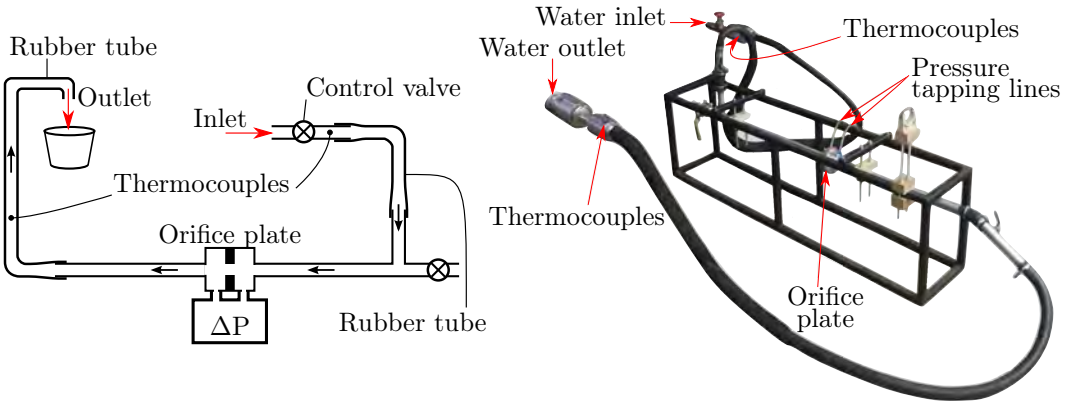

(a) (b)

Figure D.3: (a) line drawing and (b) photo of orifice plate calibration set-up for positive flow direction test

the constant measurement period was then combined with the corresponding average of the three volumetric flow-rates to give one data point. This was repeated for between eight and eleven separate flow rates spanning the range of operation. The lower flow-rates were focused on. This was done in order to provide sufficient data for curve fitting requirements. These calibration points are shown in Figure D.4.

It was found that using separate power function fits of the form $y = C_1 x^{C_2}$ for the forward and reverse flow situations gave the best results. This was because the fitting was done using volumetric flow rate as the independent variable x and the dependent variable being the reading from the pressure transducer y. Thus, when the formula had to be manipulated so that volumetric flow rate was the dependent variable it was simple

$$x = (y/C_1)^{1/C_2} \tag{D.4}$$

unlike a second order polynomial. The results of the volumetric flow rate fitting and recorded calibration results plotted against one another can be seen in Figure D.5, if the fit was absolutely perfect all the data points would lie exactly on the $y = x$ line. The results of the curve fitting can be found in Table D.2.

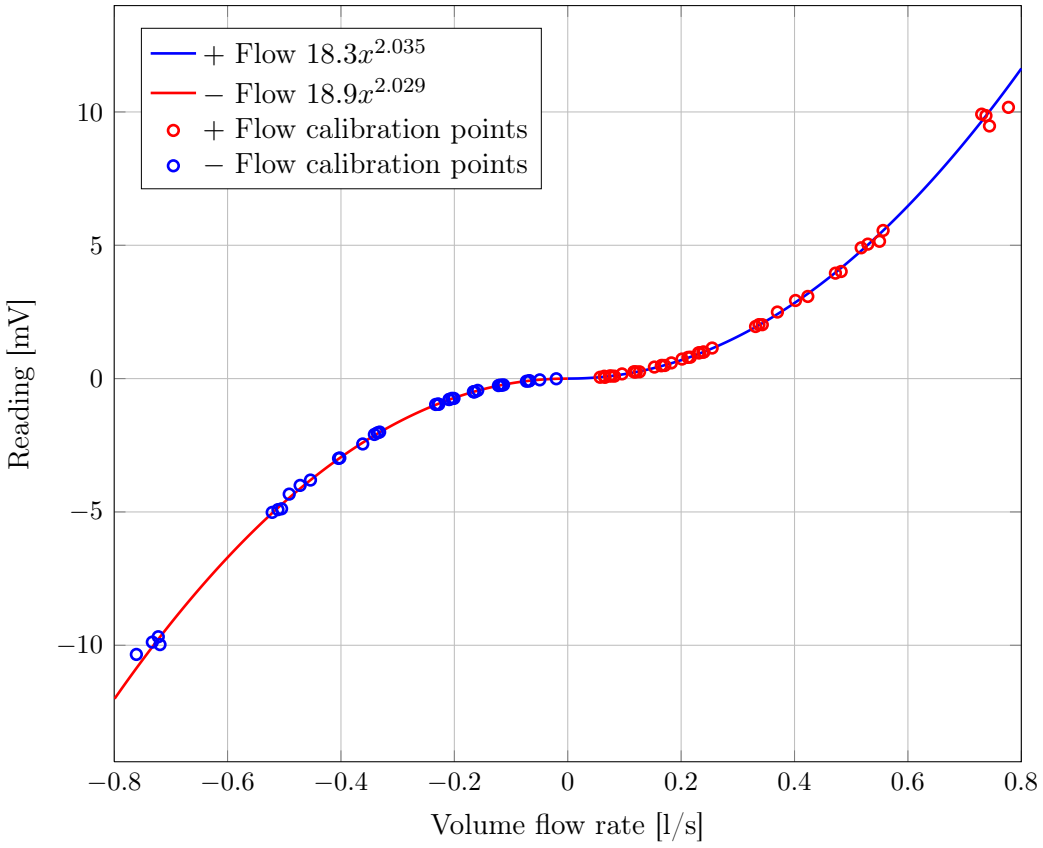

Figure D.4: Orifice plate calibration points and calibration curves

Table D.2: Results of curve fitting

Flow Direction	C_1	C_2
Forward	18.30842	2.035064
Reverse	18.91587	2.029294

For low flow rates, those below ±0.1 l/s, the calibration of the flow meter was found not accurate with a few points having an error larger than 10%, as can be seen in the second graph of Figure D.5. For flow rates below ±0.05 l/s no repeatable calibration points could be captured due to the exceptionally small flow rate, as can be seen in the second graph of Figure D.5, with only one point falling well within the range. The power function, equation D.4, used to predict flow rates is expected to enlarge the error at small flow rates, between ±0.1 l/s as seen in Figure D.5. This is particularly true for small perturbations around zero, due to the near vertical gradient of equation D.4 around zero.

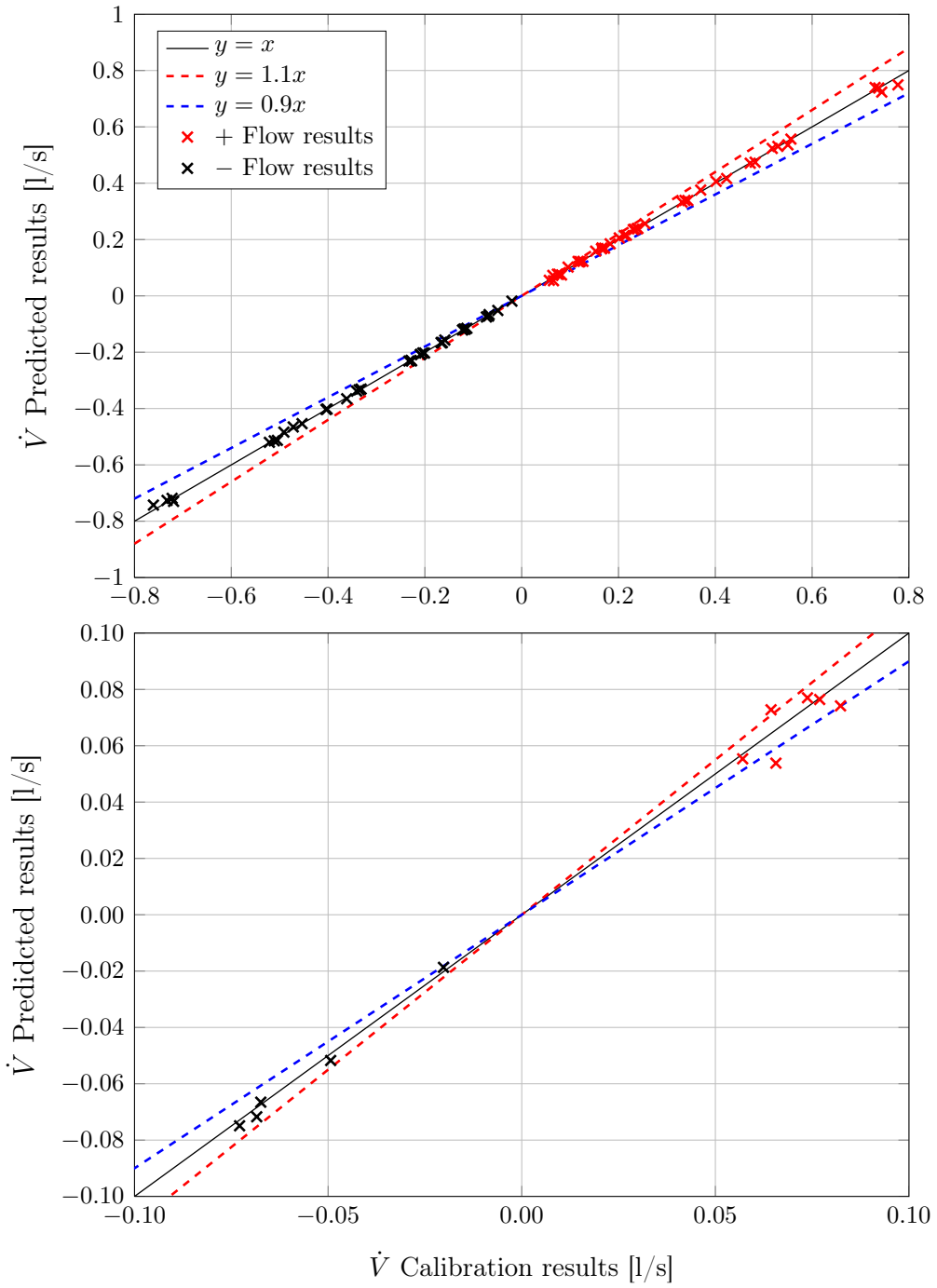

Figure D.5: Recorded volumetric flow rate versus curve fitting volumetric flow rate showing total range and single phase operation range

E. Experimental Procedure and Safety

This Appendix deals with the operation of the experimental set-up and its safety concerns. The general procedure when conducting testing is discussed along with the major outcomes of the safety report and risk mitigation steps taken.

E.1 Experimental Procedure

The experiments conducted on the experimental set-up followed similar procedures. The procedures are broken up according to pre-test events, the beginning of a test, during-test and post-test events.

E.1.1 Pre-test events

The experiment was filled with tap water using the expansion tank as the filling point. To overcome any airlocks in the piping system the expansion valve was closed allowing the expansion tank to fill. Once the tank was sufficiently full the air relief and expansion valves were opened. The air relief valve was closed once the experiment was filled with water. The experiment was checked for leaks.

Before testing could commence on the experimental set-up the water used for the test had to be prepared. This preparation was needed as the tap water contained dissolved non-condensible gases that had to be removed. The dissolved gasses were removed by heating the water until it boiled all the while releasing the air collected in the steam drum. A large steam space was allowed to form ensuring the water in the expansion tank was mixed. The steam space was then collapsed, by stopping the heat input, and the heating process and boiling was started again and was done a number of times until no air was visible in the system.

The prepared water was then used for a number of tests. By performing this preparation it allowed the operator to be confident that everything was working. Experimental data was logged for the tests. The preparatory tests were also often performed before the experiment was insulated allowing for easy identification of leaks. Once the preparatory test was completed the set-up was allowed to cool after which the actual tests could begin.

E.1.2 Beginning of test

At the beginning of a test a visual inspection of the set-up was completed. During the inspection the experiment was firstly checked for leaks. Secondly, the valves were all checked ensuring the correct positions, in particular that the expansion line valve was open. The steam drum was checked for the presence of air and the air was removed. The water levels in the constant head tank and expansion tank were also checked with the expansion tank's level recorded in the log book. The pressure lines of the pressure transducer were purged of any air bubbles. The heating elements were checked to be off then the three

phase cable was connected and turned on.

Once the above preliminary checks had been completed the data loggers connected to the laptop were checked along with the configuration settings for the readings. The voltage supply for the amplifier checked, 25.6 V resulting in 24 V, as required, supplied to the op-amp which controlled the safety relay for the heating elements. The pressure transducer readings were then zeroed taking the mean value from a 10 s period. Once the operator was confident everything was working and the desired voltage supplied by the Variac to the element was correct, logging could begin.

The QuantumX was first allowed to begin logging after which the Agilent was started as soon as possible. The Agilent was allowed a number of scans before the heating elements were turned on. The heating elements' individual switches were closed with no 24 V supply voltage to the amplifier. Then to turn the heating elements on, all that was required was the 24 V supply voltage to be supplied. Once the power was supplied to the heating elements the experiment was deemed to be running.

E.1.3 During test events

The first event to typically take place was the turning on of the secondary loop heat exchanger to remove heat from the primary loop. The time to turn the heat exchanger on was determined before the test started. The heat exchanger was turned on by allowing the cooling water to flow through it. As soon as the cooling water's flow rate was set, the mass flow rate of the water was recorded and entered into the log book. In initial tests before the secondary heat exchanger was connected and the number of cooling pipes open was also recorded. When the secondary loop was tested the heat pipe in operation was also recorded and if both were operating the mode of operation was noted in the log books. The mass flow rate was set initially through a tap, however, once the change in flow rates was discovered the rate was changed by changing the discharge points' height. The mass flow rate was measured every time it was changed and thereafter every 5-7 minutes.

By varying the flow rate of the cooling water and the heated area exposed to the cooling water, the heat removed from the set-up could be varied. The electrical power supplied to the reactor could also be varied.

The valve situated between the orifice and the reactor could also be closed with the effect of throttling the flow in the primary loop. The valve to the expansion could also be closed to allow the primary loop to run in heat pipe mode. Heat pipe mode was only entered if there was a steam space for safety reasons. The size of the steam space, when in heat pipe mode, was also recorded in the log. If air was present during a test the air relief valve was opened and the air expelled.

The pressure lines to the pressure transducer were also regularly checked for air bubbles. If one was found it was noted at which time it was first sighted. Then at the end of the test the valve between the reactor and the orifice plate

was closed allowing a zero flow reading to be taken. The zero reading could then be used as an offset in post-processing.

E.1.4 Post-test events

Once the required data was collected for the test, the heating elements were turned off and disconnected from the power supply. The mass flow rate of the cooling water was then set at a maximum to aid the cooling of the primary loop with the time noted in the log. The data collection from the Agilent and QuantumX was stopped and the respective output files along with the log were saved.

The water in the primary loop was force-cooled as time allowed, thereafter the cooling water was stopped. The experiment was then left to stand and cool by itself. If no tests in the immediate future were planned the experiment was drained of all water to prevent algae from growing in the experiment.

E.2 Safety and Risk Mitigation

The use of polycarbonate observation windows allowed the experiment to be run safely to a maximum temperature of 120°C. Due to the dangers of running the experiment a safety report was written explaining the different hazards of the set-up. The safety report's core outcome was that the experimental set-up could not be left by the operator while it was running. In addition to just the procedural side of managing the risks, the experiment was fitted with some safety features. The experiment was located in a specifically designed drip tray which could hold the entire volume of water in the system. A large Perspex shield was set up between the operator's station and the experiment.

A safety control system for the power to the elements was also designed and implemented. The system worked by using the Agilent to send a 5 V alarm signal when the temperature read by the thermocouple probe at the reactor exit was below 120°C. If the temperature exceeded 120°C the 5V signal was stopped by the Agilent. The 5 V signal was then amplified through a custom built amplifier to 24 V (Wahl, 2012). The resulting 24 V signal was then sent to a three phase relay preceding the heating elements which closed the circuit allowing the heating elements to receive power. The unit that contained the whole control system also had three lights to indicate if power was being supplied to a heating element or not. The control unit had the added benefit that the power supply, which supplied the 24 V to the amplifier, could be used as a switch for all three phases. If the 24 V were not supplied the relay would switch and the power supply to the elements would stop.

F. Condenser Section Overall Heat Transfer Coefficient for Use in Initial Guess

The effectiveness-NTU method requires the heat transfer coefficient, $(UA)_c$, to be predefined in order to work. The formula for $(UA)_c$ found in this appendix is used to calculate initial values for the iterations within the solution algorithm in Figure 4.3 as explained in section 4.3.

The experimental $(UA)_c$ was found using equation 4.21 and the experimental results. The experimental values of $(UA)_c$ were then used to find functions to predict $(UA)_c$. As the predicted values would only be used to provide initial values for the thermal resistance model, a simple straight-line function, dependent on one variable only, was chosen (T_i for condensing and two-phase regimes and T_{eo} for the liquid regime).

For the two-phase and condensing regimes it was decided to base $(UA)_c$ on the internal temperature, T_i, resulting in

$$(UA)_c = f(T_i) = 2T_i - 40 \tag{F.1}$$

with both the data and the fit shown in Figure F.1 and T_i in °C and $(UA)_c$ in W/K. For the liquid regime a piecewise linear function based on T_{eo} was used giving

$$(UA)_c = f(T_{eo}) = \begin{cases} 1.376T_{eo} - 85.26 & \text{if } 62.5 \leq T_{eo} < 83 \\ 6.484T_{eo} - 509.2 & \text{if } 83 \leq T_{eo} < 89 \\ 2.393T_{eo} - 145 & \text{if } 89 \leq T_{eo} \\ 1 & \text{if } T_{eo} < 62.5 \end{cases} \tag{F.2}$$

with both the data and the fit shown in Figure F.1 and T_{eo} in °C and $(UA)_c$ in W/K. Equation F.2 was able to capture the heat pipe start up delay characteristic for the initial values.

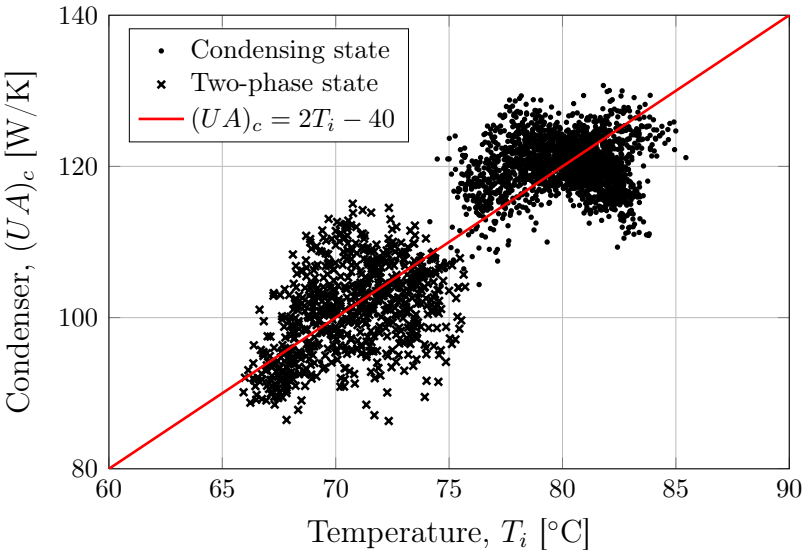

(a) Condensing & two-phase states

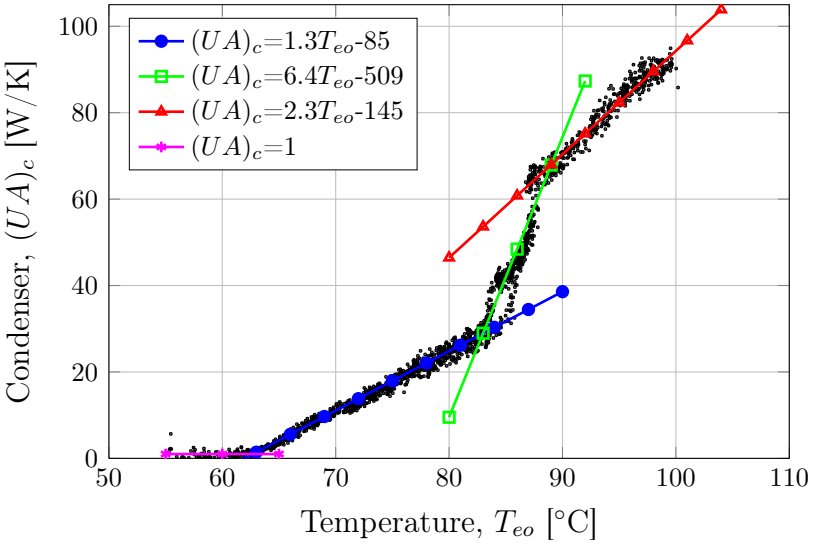

(b) Liquid state

Figure F.1: Approximations of $(UA)_c$ for use in NTU method overlaid on experimental results

G. Secondary Loop Theoretical Model Sensitivity Analysis

A sensitivity analysis was performed on the secondary loop's theoretical model. The model can be seen in Figure 4.1. Test 9 ($t = 200$ min), when the evaporator was operating in condensation mode in the steam drum, was chosen as the basis on which to compare the results of sensitivity analysis.

Table G.1 gives the base values of the variables that were varied in the analysis. The variables were varied independently of one another and are: $\dot{m}_{cw}$, mass flow rate of the cooling water supplied to the condenser; $T_{cw,in}$, temperature of the cooling water entering the condenser; T_{eo}, the temperature outside the evaporator (the steam space); D_c, the diameter of the copper pipe used in the evaporator; A_e and A_c, the surface area of evaporator and condenser respectively; l_{ew} and l_{cw}, the copper wall thickness of the evaporator and condenser respectively; k_{cu}, the thermal conductivity of copper (for the wall resistance). These values were varied by ±5, 15, 20, 30 and 50 percent.

Table G.1: Basis input variables and results for sensitivity analysis base case.

Basis	Value	unit	Basis	Value	unit
$\dot{m}_{cw}$	0.13489	kg/s	l_{ew}	0.7	mm
$T_{cw,in}$	14.93	°C	l_{cw}	0.7	mm
T_{eo}	103.9	°C	k_{cu}	401	W/mK
D_c	15	mm	$\dot{Q}_{HP}$	5.673	kW
A_e	0.11045	m^2	T_i	83.41	°C
A_c	0.1319	m^2			

The outputs of the base case $\dot{Q}_{HP}$ (heat transfer by the secondary loop) and T_i (internal temperature of the secondary loop), see Table G.1, were used to compare the variations of the sensitivity analysis as a percentage (i.e. $\% = 100 \times \dot{Q}_{HP,variation}/\dot{Q}_{HP,Basis}$), yielding the results given in Table G.2. The experimental results for the base case outputs were $\dot{Q}_{HP} = 7.229$ kW, which includes a maximum possible error of ±282 W due to thermocouple reading error, and $T_i = 80.4$ °C.

As can be seen in Table G.2 the model is more sensitive to a change in the area of the condenser, A_c, compared to a change in the area of the evaporator, A_e, which is relatively insensitive. This implies that for the specific operating condition the evaporator section of the secondary loop's heat pipe was over-designed while the condenser is undersized.

The model is highly sensitive to a change in the external temperature of the evaporator, T_{eo}. This is expected as the model uses semi-empirically calculated values for the formulas, calculated using the results from the experiment which

had similar T_{eo} values. Therefore this model is limited in its application to the operational conditions from which the data was obtained for the semi-empirical characterisation. Thus broader operational conditions should be investigated in order to understand the true effects of a change in T_{eo}.

Table G.2: Results of sensitivity analysis (as a percentage change in the outputs $\dot{Q}_{HP}$ and T_i from the base case) for different input variables (left most column) of the theoretical model of secondary loop varied from the base case by $\pm$(5;15;20;30;50)%.

%	50	70	80	90	95	105	115	120	130	150
Variable	**Percentage change of output $\dot{Q}_{HP}$ [%]**									
$\dot{m}_{cw}$	##	97.66	98.63	99.39	99.71	100.27	100.51	100.94	101.30	101.89
$T_{cw,in}$	108.28	104.98	103.33	101.67	100.84	99.17	98.33	96.66	115.40	111.42
T_{eo}	##	##	55.57	79.96	89.76	109.11	135.45	190.06	236.61	310.55
D_c	123.23	122.09	101.65	100.78	100.39	99.64	99.29	98.62	98.01	96.89
A_e	84.47	92.41	95.56	98.02	99.07	100.85	101.63	103.01	104.17	106.06
A_c	74.48	75.15	83.86	92.14	96.12	136.32	156.61	172.94	139.96	150.22
l_{ew}	100.08	100.05	100.03	100.02	100.01	99.99	99.98	99.96	99.95	99.91
l_{cw}	100.04	100.02	100.01	100.01	100.00	99.99	99.99	99.98	99.97	99.96
k_{cu}	99.75	99.89	99.94	99.97	99.99	100.01	100.02	100.04	100.06	100.08
	Percentage change of output T_i [%]									
$\dot{m}_{cw}$	##	100.44	100.27	100.12	100.04	99.95	99.90	99.82	99.75	99.64
$T_{cw,in}$	98.41	99.05	99.37	99.68	99.84	100.16	100.32	100.63	96.98	97.78
T_{eo}	##	##	60.88	81.32	91.12	108.50	114.27	125.97	138.34	163.03
D_c	96.88	96.42	100.06	100.03	100.01	99.99	99.97	99.95	99.93	99.89
A_e	83.08	93.41	96.15	98.28	99.18	100.74	101.42	102.61	103.63	105.29
A_c	104.63	104.51	102.97	101.46	100.73	92.42	87.11	81.57	91.53	88.91
l_{ew}	100.07	100.04	100.03	100.01	100.01	99.99	99.99	99.96	99.96	99.93
l_{cw}	99.99	100.00	100.00	100.00	100.00	100.00	100.00	100.00	100.01	100.01
k_{cu}	99.87	99.94	99.97	99.99	100.01	100.01	100.01	100.02	100.03	100.05

implies the model gave an error as it could not converge or values were unrealistic